HUN REN

Institute of Earth Physics and Space Science

GEOPHYSICAL OBSERVATORY REPORTS

YEAR 2023–2024

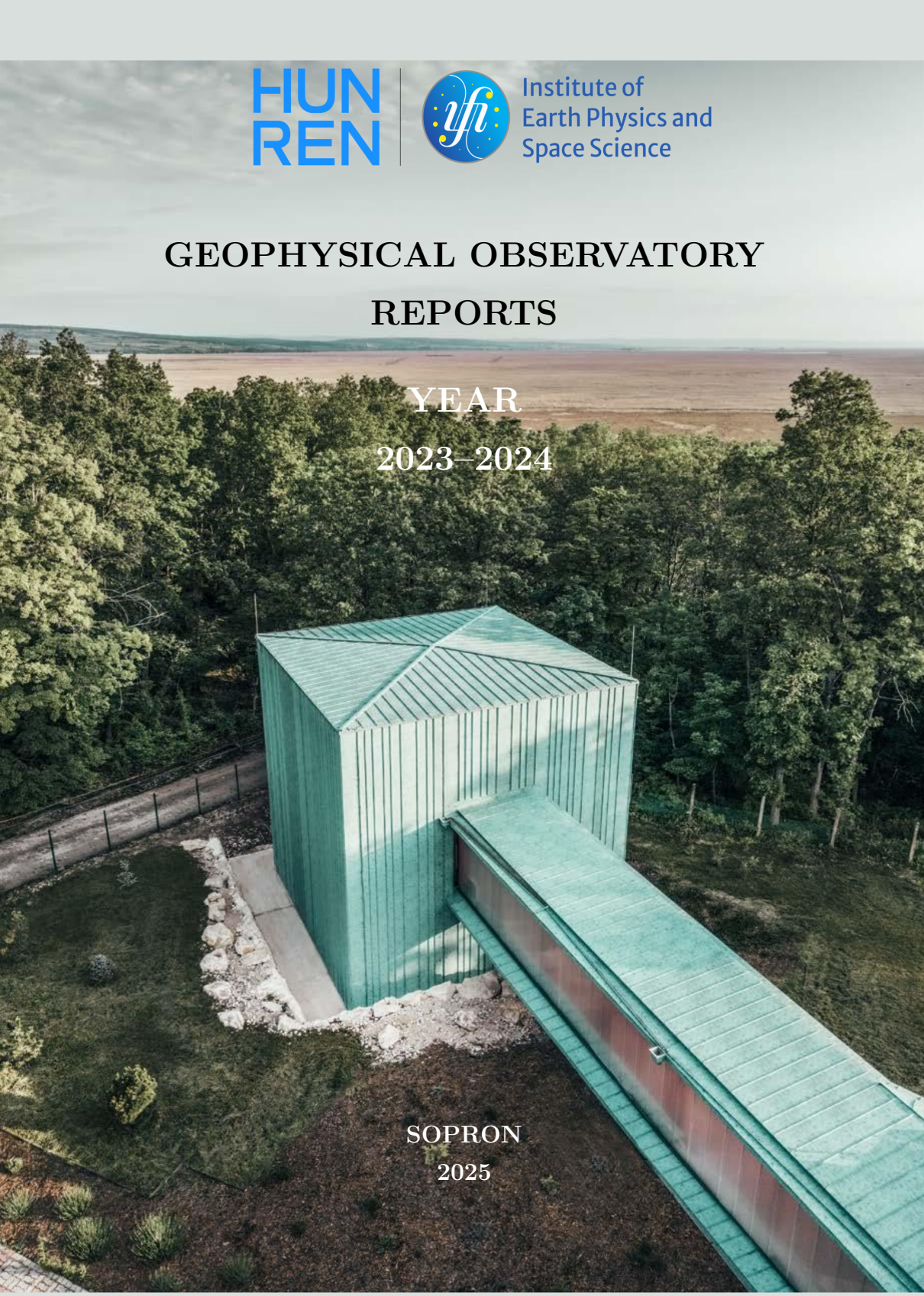

SOPRON

2025

GEOPHYSICAL OBSERVATORY REPORTS

OF THE HUN-REN INSTITUTE OF EARTH PHYSICS AND SPACE SCIENCE

YEAR
2023–2024

Editors

T. Bozóki, A. Buzás, K. Szabóné André

Authors

E. Barbély	V. Barta	J. Benedek
T. Bozóki	I. Bozsó	J. Bór
D. I. Csáki	A. Csontos	B. Heilig
N. Horn	Á. Kis	Á. Kővágó
I. Lemperger	R. Leonhardt	J. Lichtenberger
B. Meurers	Cs. Molnár	T. Molnár
A. Novák	G. Papp	L. Patkó
D. Piri	T. Rubóczki	G. Sátori
Cs. Szabó	K. Szabóné André	J. Szendrői
J. Vozár	V. Wesztergom	E. R. Williams

SOPRON
2025

ISSN 2939-5062

Responsible publisher: **Dr. István János Kovács**

Director

9400 Sopron, Csatkai E. utca 6–8

Tel.: +36-99-508-350

Contents

Preface – ***I. J. Kovács and B. Heilig*** **5**

Observatory Report for 2023–2024
V. Barta, I. Bozsó, J. Bór, A. Csontos, B. Heilig, Á. Kis, I. Lemperger and J. Lichtenberger **6**

Upgrading and Relocation of the Campbell Meteorological Station in the Széchenyi István Geophysical Observatory
K. Szabóné André, Cs. Molnár, T. Molnár, D. Piri, Cs. Szabó, J. Szendrői, V. Wesztergom and J. Bór **22**

Determining the Amplitude Transfer Function of the Permanent Magnetic ELF Measurements of the Széchenyi István Geophysical Observatory
T. Bozóki, J. Bór, K. Szabóné-André, D. Piri, A. Novák, Cs. Molnár and G. Sátori **41**

Testing the Suitability of an Unenergized Power Line Near Szakony, Hungary for Measuring the Air–Earth Electric Current
J. Bór, E. R. Williams and D. Piri **50**

Magnetotelluric Field Campaign in the Nógrád–Gömör Volcanic Field (Northern Pannonian Basin)
T. Rubóczki, Á. Kővágó, Cs. Molnár, J. Vozár and L. Patkó **69**

A Geodynamic Network for the Monitoring of Seismo–Tectonic Activity Along the Mur–Mürz Fault Line (Austria)
E. Barbély, J. Benedek, R. Leonhardt, N. Horn, Cs. Szabó, T. Molnár, D. I. Csáki, B. Meuers and G. Papp **82**

Assessing Time Synchronization in Global ELF Station Networks Based on ELF Transients
K. Németh and T. Bozóki **106**

Preface

The HUN-REN Institute of Earth Physics and Space Science (EPSS) operates a wide range of geophysical and geological observation networks in Hungary (and at some sites abroad) that provide essential information about our natural environment, including the solid Earth, the upper atmosphere and the near-Earth space. These measurements are not only essential for geophysical and geological research, but in many cases they also represent a public service monitoring activity (e.g., the Hungarian National Seismological Network) of general interest to the society, and enables EPSS to be part of major international networks like the Integrated Carbon Observation System (ICOS), the International Real-time Magnetic Observatory Network (INTERMAGNET) or the Global Ionospheric Radio Observatory (GIRO). The importance of this unique and unparalleled monitoring infrastructure is also underlined by the fact that the Hungarian National Research, Development and Innovation Office (NKFIH) recently recognized the Hungarian National Seismological Network and the Széchenyi István Geophysical Observatory as excellent research infrastructures, while the Zero Magnetic Field Laboratory (at Nagycenk) was recognized as a promising research infrastructure.

The original aim of the Geophysical Observatory Reports (GOR) series was to report on the current state of the permanent measurements at the Nagycenk Geophysical Observatory (NCK), also known as the Széchenyi István Geophysical Observatory (SZIGO), and to publish the recorded data. As these data have become available in digital format, the focus of the GOR has shifted to reporting on developments related to the measurements and the publication of short studies based on the measurement data. The fact that the Tihany Geophysical Observatory (TGO) is now also operated by EPSS has made it necessary to further extend the scope of the GOR series, which now covers all the continuous and campaign measurements carried out by EPSS (except seismological measurements).

The present issue contains a report on the current state of the permanent observations (Obervatory Reports 2023–2024), as well as 6 further studies, for example on the meteorological measurements at the NCK, the background of an MT measurement campaign carried out in the Nógrád–Gömör volcanic region and the description of the geodynamic network along the Mur–Mürz fault line.

Sopron, March 2025

Dr. István János Kovács
Director

Dr. Balázs Heilig
Deputy Director

Observatory Report for 2023–2024

Veronika Barta[1], István Bozsó[1], József Bór[1], András Csontos[1], Balázs Heilig[1,2*], Árpád Kis[1], István Lemperger[1] and János Lichtenberger[2,3]

[1]HUN-REN Institute of Earth Physics and Space Science, Sopron, Hungary
[2]Department of Geophysics and Space Sciences, ELTE Eötvös Loránd University, Budapest, Hungary
[3]HUN-REN–ELTE Space Research Group, Budapest, Hungary

Széchenyi István Geophysical Observatory

Geomagnetic Observations

The geomagnetic observations in the Széchenyi István Geophysical Observatory (IAGA code: NCK) have been perturbed in the years 2023–2024 as the construction works of the Zero Magnetic Field Lab (ZBL) were going on at that time. These works included the installation of a 2-layer, 3-meter side length μ-metal chamber, which weighs more than 6 tons and the construction of a 10 m characteristic size triaxial Merritt coil system which serves the purpose of compensating the geomagnetic field. The central point of ZBL is located not more than 60 meters from the absolute measurement pillar. This year the interaction of the compensation magnetic field and the chamber's shielding transients are analysed and tuned to be as stable as possible. This tuning process goes along with a systematic setting of the compensation magnetic field in a wide range of 0–110%.

The effect of the varying compensation field and the presence of the μ-metal chamber on the absolute measurements are significant at the distance of the pillar of the absolute measurements. For this reason, a new absolute measurement pillar location is proposed to be set. The new location is much farther from the ZBL, and the perturbation effect of the preliminary location is being investigated.

We intend to continue providing definitive data to INTERMAGNET utilising the baseline determined from the absolute measurements taken at the new location to be installed.

*Corresponding author: Balázs Heilig (heilig.balazs@epss.hun-ren.hu)
Citation: V. Barta, I. Bozsó, J. Bór, A. Csontos, B. Heilig, Á. Kis, I. Lemperger and J. Lichtenberger (2025): Observatory Report for 2023–2024. *Geophysical Observatory Reports, 2023–2024*, 6–21. https://doi.org/10.55855/gor2024.1

Geoelectric Observations

The basis of the geoelectric observation in the Széchenyi István Geophysical Observatory is a high-resolution and very sensitive digital voltmeter equipped with a 32 bit analogue/digital converter, programmed for automatic switching between measurement ranges to prevent saturation and preserve the high-resolution measurement ability. It operates two independent measurement channels corresponding to the North–South and the East–West oriented electrode pairs. The raw sampling of the hardware is 40 Hz and the data is low-pass filtered to have a 10 Hz effective sampling rate of the geoelectric field. Each of the four electrodes has been replaced with a new 1 m^2 lead-plate electrode of 1 cm width. The distance between the corresponding electrodes has been reduced to 250 m as the sensitivity of the modern instruments no longer necessitates a large span. The test phase of the instrument is in progress.

Digisonde Observations

The Digisonde (DPS 4D ionosonde) at the Széchenyi István Geophysical Observatory has operated in normal mode for most of the time of 2024.

The normal 15-minute schedule contains the following programs:

- Vertical Ionograms [1–13/14 MHz].
- Vertical and oblique sounding synchronised with Athens (AT138) [1–18 MHz].
- Skymaps for the F layer [the appropriate frequency is determined from the last recorded ionogram] and for the E layer [∼2.1 MHz] during the daytime.
- D2D (Digisonde-to-Digisonde) measurements synchronised with Pruhonice (PQ052) and Dourbes (DB049). Sopron is the receiver station.
- Maintenance programs (Built-in Test BIT, Auto gain control AG, Channel equalising CCEQ).

A quiet radio mode (TAV) also has been set on 2024-02-21, in this mode the Digisonde is able to listen to the radio universe above foF2 (it starts from 10 MHz according to the settings) up to the maximum 30 MHz limit.

The 15-minute schedule in the normal operational mode is the following:

Number	**Program**	**Start**
1	Vertical ionogram [1–13 MHz]	0:00
2	D2D PQ 052, Passive	2:35
3	Skymap [F region]	3:55
4	D2D DB049, Passive	4:36

5	Vertical, oblique sounding with AT138	5:00
6	Radio listening mode (TAV)	7:00
7	D2D PQ 052, Passive	7:35
8	BIT	8:20
9	CCEQ	8:22
10	AG	8:34
11	D2D DB049, Passive	9:36
12	Vertical ionogram [1–14 MHz]	10:00
13	Skymap [E region]	11:45
14	D2D PQ 052, Passive	12:35
15	Radio listening mode (TAV)	14:30
16	D2D DB049, Passive	14:36

High-cadence campaigns (1 ionogram/min) have been performed during the year to study the Medium Scale Travelling Ionospheric Disturbances generated by the terminator and/or by intense tropospheric events (Cyclone Boris). The dates of the 1-min campaigns are the following: 2024-03-20; 2024-06-20; 2024-09-08-2024-09-10; 2024-09-12; 2024-09-13.

It is important to note that the strength of the received signal was lower especially in the lower frequency band (< 5 MHz) in the first part of the year because of a hardware issue that was solved on 18 July 2024. Therefore, the Digisonde provided the standard good-quality ionograms after 19 July 2024.

Sopron Digisonde data is available at: http://iono.nck.ggki.hu/. Furthermore Sopron station provides data to GIRO (Global Ionosphere Radio Observatory, https://giro.uml.edu/), to the European Mirror site of GIRO (Prague), to DIAS (DIgital upper Atmosphere Server) and TechTIDE (https://techtide.eu/) servers at Athens and the eSWua portal of INGV (electronic space weather upper atmosphere, Istituto Nazionale di Geofisica e Vulcanologia, Rome).

Atmospheric Electricity

Atmospheric electricity measurements were continuous in the years 2023–2024.

VLF Observations

The VLF measurements were operated continuously at Nagycenk in 2023–2024 and supplied data for AWDANet (inferring plasmaspheric electron density from whistler data) and AARDDVARK (for monitoring ionospheric D-region perturbations) networks.

Meteorological Observations

Meteorological measurements were continuous in the years 2023–2024, meteorological records have been regularly submitted to the central database of HungaroMet, the National Meteorological Service in Hungary.

Tihany Geophysical Observatory

Tihany Geomagnetic Observatory (IAGA code: THY) was established in 1954. For almost 70 years, THY belonged to the Eötvös Loránd Geophysical Institute and its legal successors. In 1991, THY was one of the founding members of INTERMAGNET. In 2023, THY was taken over by the Institute of Earth Physics and Space Science (EPSS).

In addition to its original task, the observatory has always hosted other geophysical measurements, such as observation of paleomagnetic, geothermic, seismologic, and different space phenomena.

Geomagnetic Observations

In 2023, data were recorded by three parallelly run vector magnetometers (two fluxgate and one DIDD). Following the INTERMAGNET standard, we calculate and record minute mean values by applying a standardised Gaussian filter to the instruments 1-second samples (5 seconds for the DIDD), using our data collection system. Since 2019, a new LEMI-035 magnetometer with suspended sensors, which has a high tolerance against external electromagnetic noise, has been operated as the primary system. It was installed in the pavilion (#4 in Fig. 2). To meet the anticipated new INTERMAGNET standards, we implemented an OBSDAQ system with an A/D converter of 24-bit resolution and 128 Hz sampling rate in the primary system.

For recording the total field, alongside the continuously operating GSM-19 Overhauser magnetometer (which operates in the attic of the absolute house), we operated at least one additional scalar magnetometer running in parallel. The DIDD systems data can serve as a backup for three-component recording, as this instrument performs measurements every 5 seconds needed for determining inclination and declination. Each measurement sequence also includes the total field value, which can thus be used to generate the observatorys XYZ minute averages. The instrument measures the geomagnetic components in the eastern room of the variation house (#3 in Fig. 2). The data collection task is handled by a version of MAGLIN software adapted for DIDD systems. Naturally, we record and archive all measurements, including 1- and 5-second samples.

Since 2020 the DTU FGE device has been operated in the western room of the variation house (#3 in Fig. 2). The data-collecting system of this device is a MAGOR DAQ system. The DAQ fulfils the new INTERMAGNET standards as well.

The absolute measurements were performed in the absolute house (#2 in Fig. 2) on the absolute pillar (pillar 1). In 1991, pillar 1 was rebuilt. In this year the azimuth value of the reference mark was determined. For absolute measurements, our instrument set consists of Zeiss 010A (primary) and Zeiss 20A (DIM) theodolites transformed into non-magnetic by MinGeo Ltd., and equipped with DMI (Danish) magnetometers. Using the Zeiss instruments, we conducted measurements at least weekly, following the null-point method. The difference between the total field values measured on the absolute pillar and the site of the GSM-19 instrument was regularly observed. The pillar difference (total field measurement site absolute pillar) was −1.6 nT in 2023. Annual mean values are for the year 2023: Decl.: 5°10.3; Incl.: 63°42.5; H: 21584 nT; X: 21496 nT; Y: 1946 nT; Z: 43688 nT; F: 48729 nT.

The absolute measurements were performed, and the definitive yearly dataset was processed by András Attila Csontos.

Most of our data collection systems are based on the MAGLIN software, and remote access is provided when needed. In addition to INTERMAGNET minute averages, we also perform continuous one-second sampling with the LEMI magnetometer.

The observatory provided a quasi absolute quasi-real-time minute mean record of geomagnetic components for the INTERMAGNET GIN server in Edinburgh. Since 2023 the quasi absolute quasi-real-time one-second sampled record has also been transmitted. The preliminary geomagnetic records for 2023, as well as definitive data for years 1991–2022, are available at the INTERMAGNET website (https://intermagnet.org/).

EMMA Observations

The European quasi-Meridional Magnetometer Array (EMMA) was established in 2012 in the frame of the EU FP7 PLASMON project. The network was taken over in 2023 by EPSS and is now coordinated by this institute. EMMA consists of 27 variometer stations equipped with fluxgate vector magnetometers from northern Finland to the middle of Italy, covering low middle and high geomagnetic latitudes (L = 1.56). Currently, EPSS operates three of these stations. Besides the Tihany station, one magnetometer is operated in Vyhne (Slovakia) in cooperation with the Hurbanovo Geophysical Observatory of the Slovak Academy of Sciences, and one in Lonjsko Polje Geomagnetic Observatory (IAGA code: LON) in collaboration with the University of Zagreb. EMMA stations were operational in 2023 and 2024. The availability of the observations varied station by station. Detailed information on the availability, as well as quick look line plots and dynamic power spectra are available at the EMMA website: http://geofizika.canet.hu/plasmon/.

VLF Observations

The VLF measurements had been operated continuously at Tihany in 2023–2024 and supplied data for AWDANet (inferring plasmaspheric electron density from whistler data), AARDDVARK (for monitoring ionospheric D-region perturbations) and WWLLN (for global lightning locations) networks.

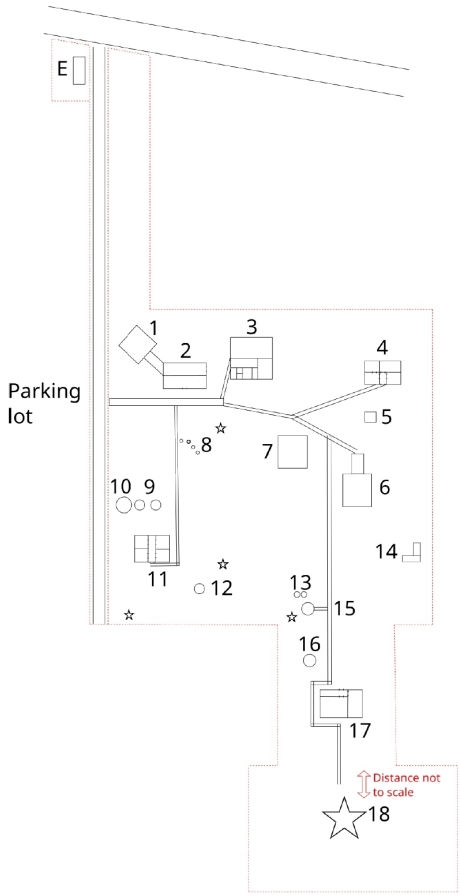

Fig. 1. Schematic of the buildings, measurements operate at the SZIGO. E Entrance; 1 Zero Magnetic Field Laboratory with corridor; 2 Telluric measurements; 3 Main building with staff hostel and electronic laboratory; 4 Computer centre (data loggers, server of local network, satellite transmitter); 5 Proton magnetometer (DI/DD); 6 Building of geomagnetic variometer station; 7 Building for geomagnetic absolute measurements with 4 pillars installed; 8 Meteorological measurement instruments (Campbell meteorological station central stand, Visibility meter, LIDAR for measuring cloud base); 9 Twin Atmospheric electric potential gradient sensors (radioactive); 10 Atmospheric electric potential gradient sensors (field mill); 11 Atmospheric electricity house (data logging of the Schumann resonance data (ELF-band electric and magnetic field records), atmospheric electric potential gradient, LINET lightning detection network station, atmospheric UV detection); 12 Electric ball antenna of the Schumann resonance recording system; 13 InSAR corner reflectors; 14 Magnetic induction coils of the Schumann resonance recording system; 15 Place of the old meteorological station; 16 VLF antenna; 17 Digisonde station; 18 Digisonde transmitter antenna. The smaller star symbols represent the receiver antennas of the Digisonde.

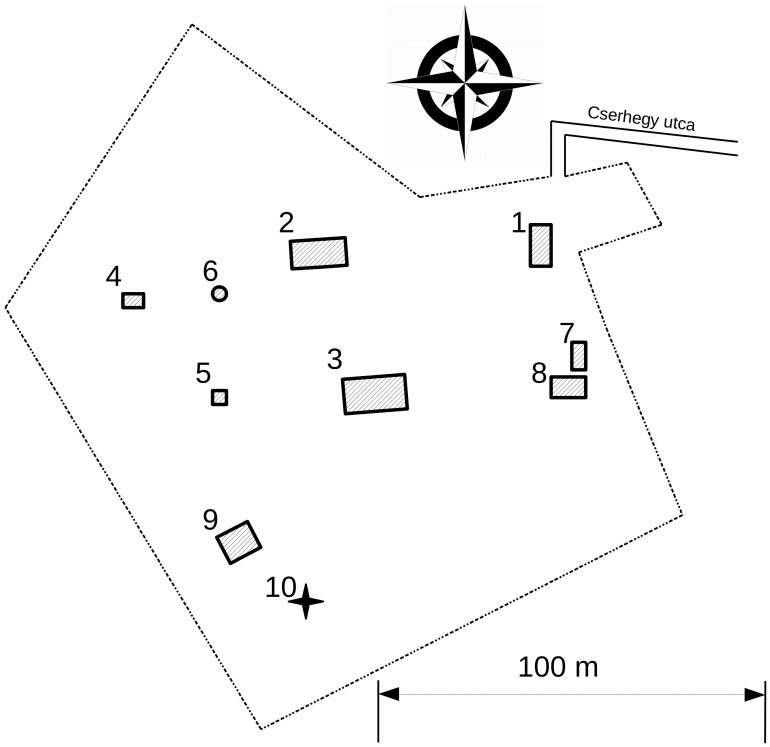

Fig. 2. Schematic of the buildings, measurements operate at the THY. 1 Clock house; 2 Absolute house (absolute pillars [1 and 2] and total field measurement); 3 Variation house (pillars are in the eastern and in the western room); 4 Pavilion (two pillars); 5 New measurement hut; 6 Temperature hut; 7 Test building; 8 Laboratory; 9 Green house; 10 VLF antenna.

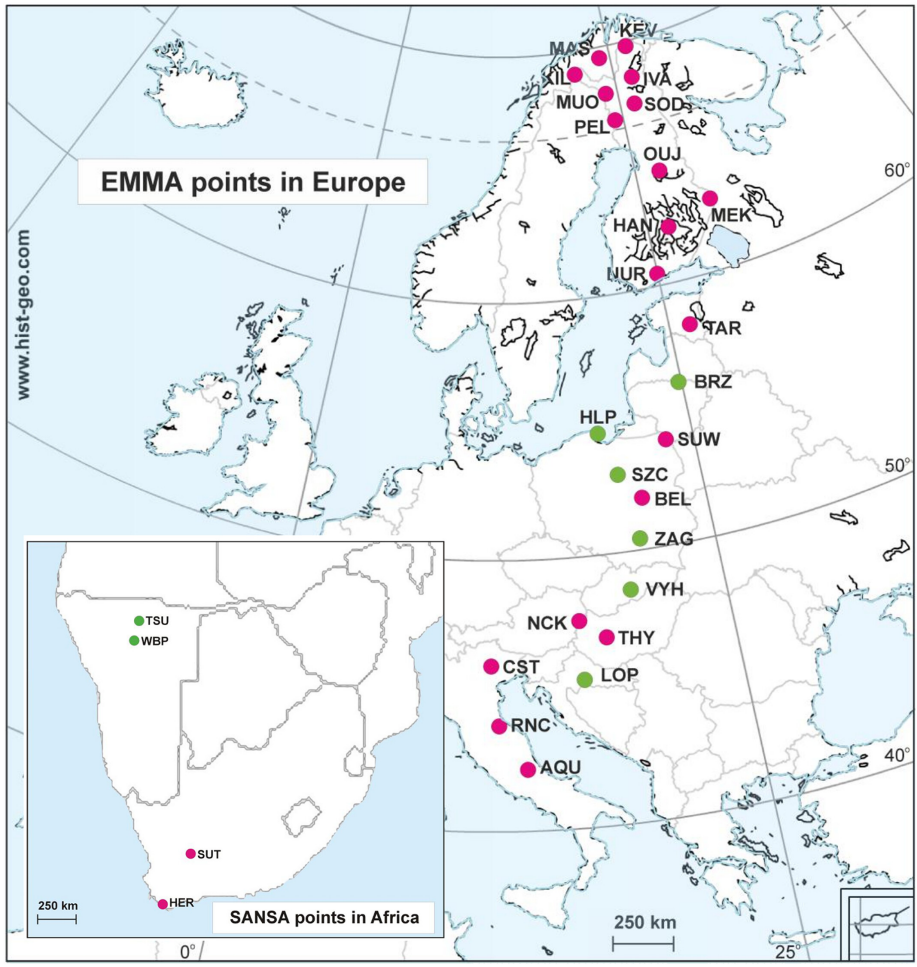

Fig. 3. EMMA stations (Jorgensen et al, 2017).

Table I. Observations at Széchenyi István Geophysical Observatory.
∗: Referenced to the geometrical center of the two electrode pairs positioned in N–S and E–W directions buried in a depth of 2 m nearby the observatory.

Geomagnetic Observations	**type**	**manufacturer**	**year of production**	**year of installation**	**frequency band**	**sampling rate**	**data rate**	**observation site**	**owner of data**	**other**
variation recording / primary	DTU FGE	DTU, Lyngby, Denmark	2020	2020	DC–0.2 Hz	20 Hz	1 s	variation house, pier 1	EPSS	Orientation: XYZ
back-up	LEMI-025	LEMI LLC., Lviv, Ukraine	2010	2010	DC–5 Hz	10 Hz	1 s	variation house, pier 1	EPSS	Orientation: XYZ
absolute measurement	Zeiss-10A + DTU DIM	Zeiss-DTU-MinGeo Ltd.	2018	2019		twice a week (Mon and Thu)	twice a week (Mon and Thu)	absolute variation house, pier 2	EPSS	
absolute measurement	GSM-19	Gem Systems, Markham, Canada	2016	2016		1 s	1 s	absolute variation house, pier 2	EPSS	
MIRA	in-house	in-house	2000	2000	n/a	once every two years	once every two years	absolute variation house, pier 2	EPSS	Azimuth: 298°33.92’
Geoelectric Observations	**type**	**manufacturer**	**year of production**	**year of installation**	**frequency band**	**sampling rate**	**data rate**	**observation site**	**owner of data**	**other**
variation recording			2022	2022	DC–10 Hz	40 Hz	10 Hz	∗	EPSS	Orientation: x – North, y – East

Ionosonde Observations	**type**	**manufacturer**	**year of production**	**year of installation**	**frequency band**	**sampling rate**	**data rate**	**observation site**	**owner of data**	**other**
Ionosonde	DPS-4D	Lowell Digital International		2018	1–30 MHz	5 min	5 min	SZIGO, ionosonde house + antenna system	EPSS	
Atmospheric Electricity Observations	**type**	**manufacturer**	**year of production**	**year of installation**	**frequency band**	**sampling rate**	**data rate**	**observation site**	**owner of data**	**other**
Schumann resonance (SR) electric	SR electric monitoring system	in-house		1993	5–35 Hz	500 Hz	0.002 s	SZIGO	EPSS	
SR magnetic	SR magnetic measuring system	in-house		1996	3–40 Hz	500 hz	0.002 s	SZIGO	EPSS	
Atmospheric electricity, potential gradient (PG)	Radioactive collector-tpye PG measuring instrument #1	in-house		1961	DC	11 Hz	11 Hz	SZIGO	EPSS	

PG	Radioactive collector-tpye PG measuring instrument #2	in-house		1998				SZIGO	EPSS	
PG	EFM-100	Boltek, Port Colborne, Canada		2013	DC	2 Hz	2 Hz	SZIGO	EPSS	
VLF Wave Observations	**type**	**manufacturer**	**year of production**	**year of installation**	**frequency band**	**sampling rate**	**data rate**	**observation site**	**owner of data**	**other**
AWDANet										
VLF receiver	VLF receiver	ELTE, BL Electronics Ltd.	2003	2002	100 Hz–20 kHz	40 kHz	variable	Nagycenk	ELTE	
AARDDVARK										
VLF receiver	VLF receiver	ELTE, BL Electronics Ltd.	2007	2007	100 Hz–40 kHz	96 kHz	0.05 s	Nagycenk	ELTE	
Meteorological Observations	**type**	**manufacturer**	**year of production**	**year of installation**	**frequency band**	**sampling rate**	**data rate**	**observation site**	**owner of data**	**other**
Temperature	Campbell HMP35D, BME280	Campbell Scientific		1997, 2020		5 s	variable, 1.5, 10 min, lately 1 min	SZIGO	EPSS	

Relative humidity (RH)	Campbell HMP35D	Campbell Scientific		2020		6 s	variable, 1.5, 10 min, lately 1 min	SZIGO	EPSS
Wind (direction and speed)	Campbell 05103-LC	Campbell Scientific		1997		5 s	variable, 1.5, 10 min, lately 1 min	SZIGO	EPSS
Air pressure	Campbell CS106	Campbell Scientific		2022		5 s	variable, 1.5, 10 min, lately 1 min	SZIGO	EPSS
Air pressure	BME280	Bosch Sensortec		2020		6 s	variable, 1.5, 10 min, lately 1 min	SZIGO	EPSS
Precipitation	Campbell ARG100	Campbell Scientific		1997		5 s	variable, 1.5, 10 min, lately 1 min	SZIGO	EPSS

Table II. Observations at the Tihany Geophysical Observatory.

Geomagnetic Observations	**type**	**manufacturer**	**year of production**	**year of installation**	**frequency band**	**sampling rate**	**data rate**	**observation site**	**owner of data**	**other**
variation recording / primary	LEMI-035	LEMI LLC., Lviv, Ukraine	2017	2018	DC–5 Hz	128 Hz	1 s	new variation pavilion, pier 1	EPSS	Orientation: XYZ
back-up	DTU FGE (upgraded)	DTU, Lyngby, Denmark	1999 (sensor)	2019	DC–5 Hz	128 Hz	1 s	variation house, eastern room	EPSS	Orientation: XYZ
back-up	DIDD (upgraded)	Gem Systems, AMrkham, Canada; MinGEO LTd., Budapest, Hungary	1999 (sensor)	2019	DC–0.2 Hz	1 Hz	0.2 Hz	variation house, western room	EPSS	Orientation: IDF
absolute measurements	Zeiss-10A + DTU DIM	Zeiss–DTU–MinGeo Ltd.	2004	2005		weekly	weekly	absolute house, pier 1	EPSS	
absolute measurements	Zeiss 020A + DTU DIM	Zeiss–DTU–MinGEo Ltd.	2006	2006		occasionally		absolute house, pier 1	EPSS	
absolute measurement	GSM-19	Gem Systems, Markham, Canada	1991	1991		5 s	5 s	absolute house, attic	EPSS	

MIRA	the southern tower of the Tihany Benedictine Abbey					occasionally		absolute house, pier 1	EPSS	Azimuth: 3°59'10"
Geomagnetic Observations	**type**	**manufacturer**	**year of production**	**year of installation**	**frequency band**	**sampling rate**	**data rate**	**observation site**	**owner of data**	**other**
EMMA										
variometer	LEMI-035 fluxgate	LEMI LLC., Lviv, Ukraine	2010	2011	DC–5 Hz	128 Hz	1 s	Lonjsko Polije (HR)	EPSS	Orientation: DHZ
variometer	LEMI-035 fluxgate	LEMI LLC., Lviv, Ukraine	2010	2011	DC–5 Hz	128 Hz	1 s	Tihany	EPSS	Orientation: DHZ
variometer	Narod STE fluxgate	Narod Geophysics Ltd., Vancouver, Canada	2006	2012	DC–5 Hz	128 Hz	1 s	Vyhne (SK)	EPSS	Orientation: DHZ
VLF Wave Observations	**type**	**manufacturer**	**year of production**	**year of installation**	**frequency band**	**sampling rate**	**data rate**	**observation site**	**owner of data**	**other**
AWDANet										
VLF receiver	VLF receiver	ELTE, BL Electronics Ltd.	2002	2002	100 Hz–20 kHz	40 kHz	variable	Tihany	ELTE	
WWLLN										
VLF receiver	VLF receiver	ELTE, BL Electronics Ltd.	2005	2005	100 Hz–48 kHz	96 kHz	variable	Tihany	ELTE/ wwlln.net	

AARD-DVARK										
VLF receiver	VLF receiver	ELTE, BL Electronics Ltd.	2007		2007	100 Hz–48 kHz	96 kHz	0.05 s	Tihany	ELTE

Upgrading and Relocation of the Campbell Meteorological Station in the Széchenyi István Geophysical Observatory

Karolina Szabóné André[1]*, Csaba Molnár[1], Tibor Molnár[1], Dániel Piri[1], Csongor Szabó[1], Judit Szendrői[1], Viktor Wesztergom and József Bór[1]

[1]HUN-REN Institute of Earth Physics and Space Science, Sopron, Hungary

Abstract

The main meteorological station at the Széchenyi István Geophysical Observatory equipped mostly with Campbell Scientific meteorological instruments has undergone a major change in recent years. Data download from the data logger has been automated by a mini-PC, new instruments have been added (ceilometer, visibility and present weather sensor, barometer) and the station has been moved to a new location. Now it better complements the atmospheric measurements in the observatory, for example by facilitating the determination of the so-called fair-weather conditions for the evaluation of atmospheric potential gradient measurements. Additionally, a cooperation with the Hungarian Meteorological Service (HMS) has been established, in the framework of which meteorological data are transmitted from the observatory to the HMS. Plots of the station data, updated every 10 minutes, are available on the observatory's website.

Keywords: meteorological measurements, weather, ceilometer, visibility sensor.

Brief History of the Station Before 2021

A meteorological station was installed in the Széchenyi István Geophysical Observatory (NCK) near Nagycenk, Hungary, at the end of 1997 to support other measurements such as the atmospheric electric potential gradient (PG) measurements. Temperature, relative humidity, wind speed, wind direction, global solar radiation, and precipitation data was logged in 10-minute temporal resolution using a Campbell CR10X datalogger (Figs. 1 and 2, Table I). The station

*Corresponding author: Karolina Szabóné André (szabone.a.karolina@epss.hu)

Citation: K. Szabóné André, Cs. Molnár, T. Molnár, D. Piri, Cs. Szabó, J. Szendrői, V. Wesztergom and J. Bór (2025): Upgrading and relocation of the Campbell meteorological station in the Széchenyi István Geophysical Observatory. *Geophysical Observatory Reports, 2023–2024*, 22–40. https://doi.org/10.55855/gor2024.2

was located near the so-called ionosonde house in a sheltered place surrounded by trees (Fig. 3a).

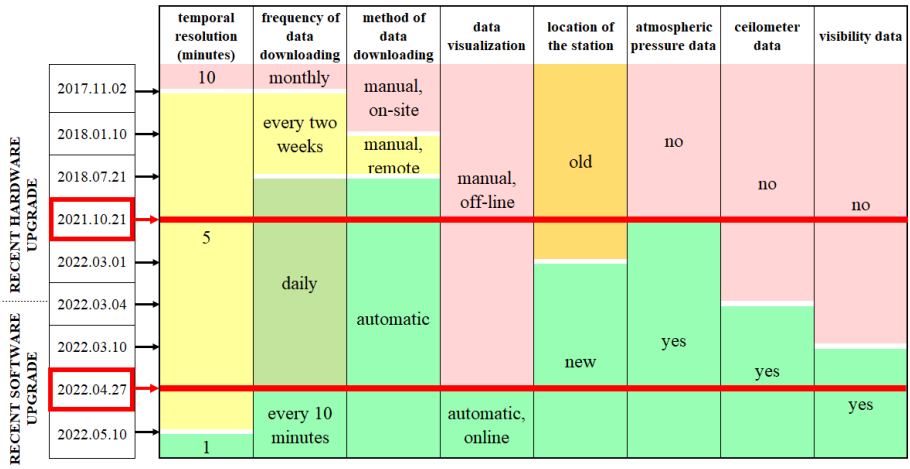

Fig. 1. Evolution of the Campbell meteorological station between 2017 and 2022. The upper red line indicates the recent hardware upgrade which started on 21th October 2021 when the newly purchased barometer was installed. The second red line indicates the recent software upgrade (27th April 2022), the implementation of programs to process data from the new instruments and display all data every 10 minutes.

The first data series of the station was published in the Geophysical Observatory Reports: 1999–2001 (2003). The measurements were suspended in 2012 and were resumed only at the end of August 2017. Data was manually backed up from the data logger quasi monthly using a laptop. A mini-PC was installed in 2018. This enabled automatic daily backup of data from the data logger.

When PG data is evaluated, it is essential to know whether there were fair weather conditions at the measurement site (Harrison and Nicoll, 2018). It is important to have data about the cloud cover, hydrometeors, and wind speed measured at 10 m above ground level. The first two parameters can be determined using a ceilometer and a visibility and present weather sensor. Besides, a meteorological station is incomplete without a barometer measuring the atmospheric pressure. The need to purchase these instruments has therefore arisen and has been fulfilled in the framework of the INFRA tender of the Eötvös Loránd Research Network (ELKH) in 2021.

Fig. 2. The Campbell meteorological station, surrounded by trees in its original location.

Relocation of the Station and Installation of the New Instruments

The station was moved from its original location to a more open place near the PG measurements (Figs. 3 and 4) on 1st March 2022. The newly purchased barometer was placed into the box of the datalogger on the main tower, and it is operating since 21st October 2021. The ceilometer as well as the visibility and present weather sensor were installed during the relocation of the station. Some details about the instruments can be found in Table I.

LIDAR Ceilometer

A SkyVUE PRO light detecting and ranging (LIDAR) ceilometer was purchased from the Campbell Scientific Ltd. The instrument uses short pulses of near infra-red light ($\lambda = 915 \pm 5$ nm with 10 kHz pulse frequency) to detect cloud layers. The emitted short pulses are scattered back from aerosol particles of the atmospheric column above the instrument. The measured (raw) back-scattered data is calibrated and range corrected by the instrument to obtain the so-called two-way attenuated backscatter profile (hereinafter referred to as attenuated

Table I. Some details about the instruments in operation at NCK.
*elevation of the barometer is above mean sea level.

Instrument	Location	Elevation above ground level	Link
Väisälä humidity and temperature probe	main tower (loc. 1 on Fig. 3)	2.0 m	HMP35D manual
Väisälä barometer	main tower (loc. 1 on Fig. 3)	154.66 m*	PTB110 manual
Young wind monitor	main tower (loc. 1 on Fig. 3)	2.4 m	05103-LC
Skye Instruments Pyranometer	main tower (loc. 1 on Fig. 3)	2.0 m	SP1110
Tipping bucket rain gauge	loc. 4 on Fig. 3	1.3 m	ARG100 brochure manual
Visibility and present weather sensor	loc. 2 on Fig. 3	1.5 m	CS125
HygroVUE5 humidity and temperature probe	loc. 2 on Fig. 3	1.5 m	HygroVUE5 manual
LIDAR ceilometer	loc. 3 on Fig. 3		SkyVUE PRO manual

backscatter profile; SkyVUE PRO manual, 2022, Appendix A). This variable is reported by the instrument besides other cloud-related data. The height of the scattering aerosols can be obtained from the time difference between the emitted and back-scattered signal. The strength of the back-scattered light varies with height and this data allows identification of cloud bases. If there is significant scattering but the cloud base cannot be defined, then the vertical visibility can be calculated. The maximum reporting range of the SkyVUE PRO LIDAR is 10 km, and the reporting resolution is 5 m.

Visibility and Present Weather Sensor

A CS125 Visibility and Present Weather sensor (hereinafter referred to as CS125) was also purchased from Campbell Scientific Ltd. This instrument uses infra-red light ($\lambda = 850 \pm 35$ nm with 1 kHz light pulse rate) to determine visibility and to identify hydrometeors (e.g., mist, fog, rain, etc.). The state of

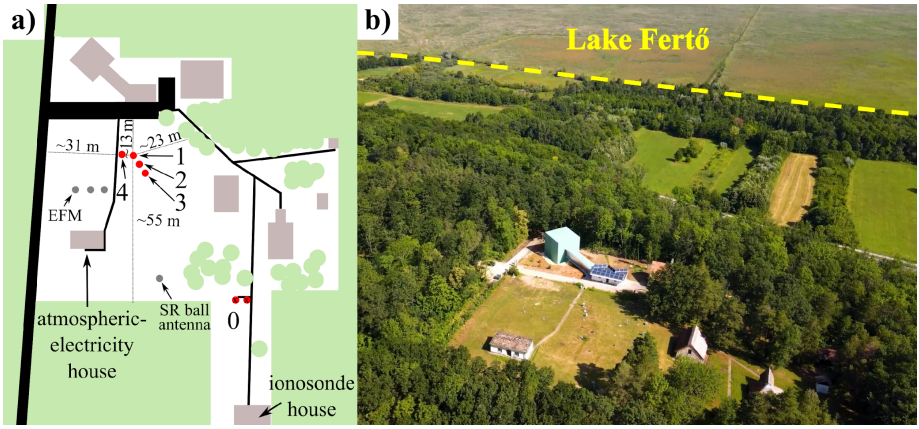

Fig. 3. **a)** Location of the Campbell meteorological station in the observatory: location before (0) and after 1st March 2022 (1: main tower, 2: visibility and present weather sensor (CS125), 3: ceilometer (LIDAR), and 4: tipping bucket rain gauge). Green area and circles indicate forest and individual trees, respectively. The Boltek Electric Field Monitor (EFM) and the two radioactive instruments measuring the atmospheric electric potential gradient are marked by three grey dots. **b)** A photo of the surroundings of the NCK observatory at the end of June 2022. The shore of Lake Fertő is marked by a yellow dashed line. Source of original photo: website of the EPSS (EPSS news, 2022).

present weather can be reported in the form of e.g., SYNOP and METAR code (WMO, 2019; Milrad, 2017; Wikipedia, 2022). Besides, the CS125 can report precipitation intensity (mm/h). A HygroVUE5 temperature and relative humidity sensor is connected to the CS125 to make more precise discrimination between liquid and frozen precipitation. The measuring range of the CS125 is from 5 m to 75 km (visibility).

Collaboration with the Hungarian Meteorological Service

For better utilization of the new instruments, a cooperation has been established between the HUN-REN Institute of Earth Physics and Space Science (EPSS) and the Hungarian Meteorological Service (HMS). Ceilometers as well as visibility and present weather sensors provide very useful information to support e.g., aviation services. In Hungary, nine ceilometers are in operation in the Tiszántúl Region, one in Budapest and other two in the Transdanubia (Siófok and Pécs) (Fig. 5), and data from theses sensors are collected in the E-profile database (E-profile, 2022). In Little Hungarian Plain (northern part of Transdanubia), there has been no such measurement so far, therefore our new instrument at Fertőboz, near Sopron can fill this gap. Registration to the E-profile database and preparation of data transmission to the E-profile database was in progress at the time of writing this paper. The transmission of ceilometer data as well

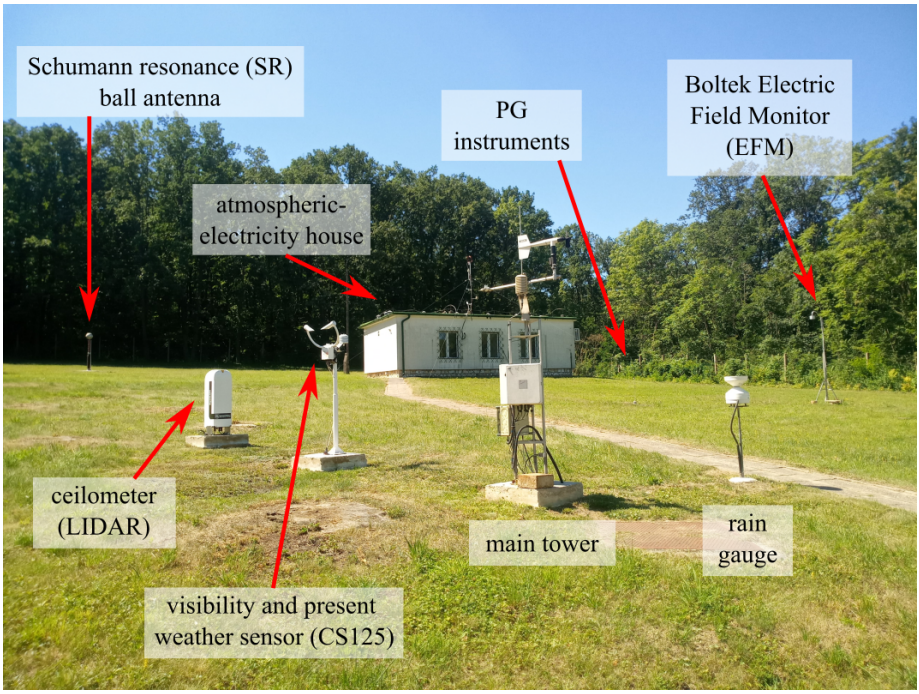

Fig. 4. The Campbell meteorological station with the new instruments at its new location since 1st March 2022.

as visibility and present weather sensor data to the HMS is already operational. Additionally, all data collected with the CR10X data logger enriches the HMS meteorological database.

Data Processing System

A MeLE StarCloud PCG02 Plus stick PC (mini-PC) is placed in the box of the CR10X datalogger in the main tower of the meteorological station. This mini-PC runs a Windows 10 Home operating system and it performs the data obtaining, processing, forwarding, archiving, and plotting tasks. The CR10X datalogger, the LIDAR and the CS125 are connected to the mini-PC via RS232-USB cables. The LIDARs adapter is connected directly through one of the two USB ports of the mini-PC. The other two devices are connected through a USB-hub. Note: an experimental atmospheric pressure measurement based on a simple sensor (BOSCH BME280) is also installed on the main tower. This instrument is also connected to the mini-PC through the USB-hub.

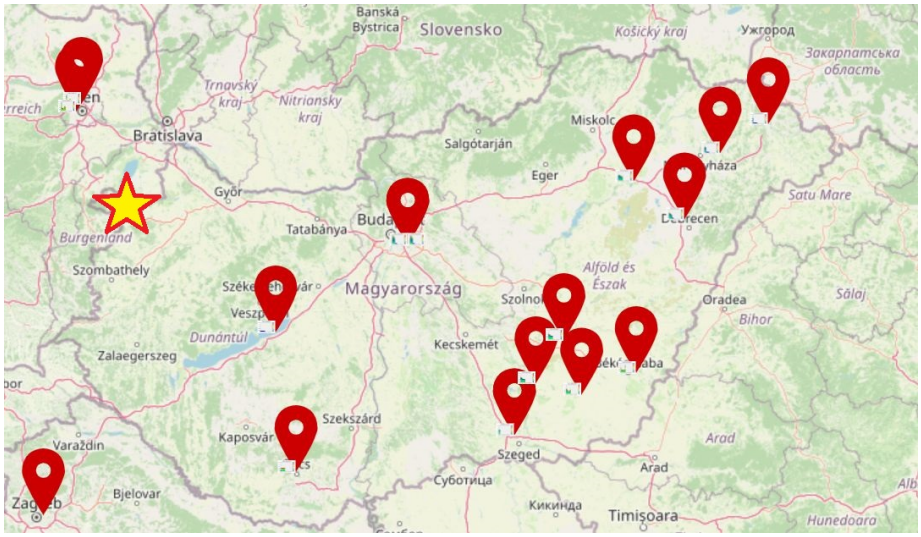

Fig. 5. Location of the LIDAR stations of the E-profile network in Hungary and its surroundings. The location of the new LIDAR (Fertőboz) is marked with a star. Source of the map: E-profile (2022), edited by the Authors.

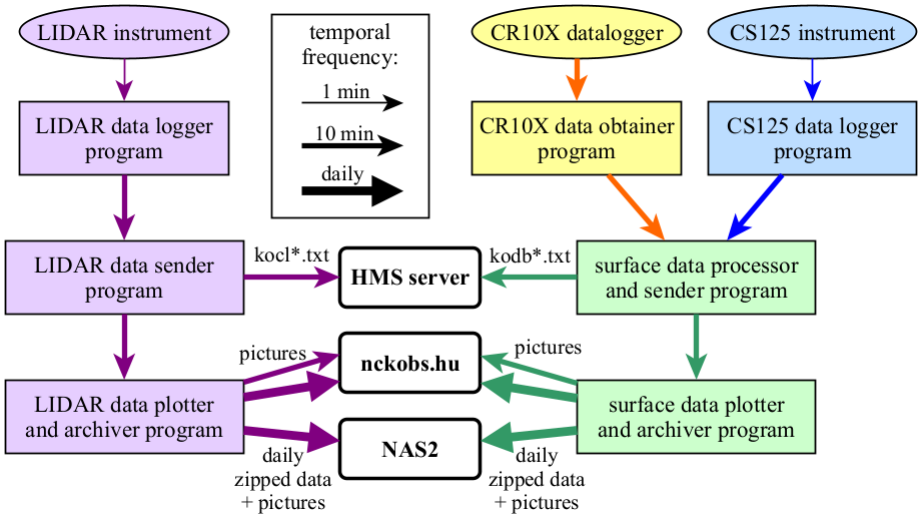

Fig. 6. Data flow of the Campbell measuring system. HMS server is the data-receiving gateway of the Hungarian Meteorological Service (HMS), NAS2 is the network-attached storage service of the HUN-REN Institute of Earth Physics and Space Science.

The data processing system is designed to produce data files which can be transmitted to the HMS. Data are divided into two groups. LIDAR telegrams are stored in plain text files (with kocl prefix in the file names), while the data from CR10X and CS125 are merged into a common txt file. These files are called surface data files (with kodb prefix in the file names). Both types of data files contain 10 minutes of data. The name of the data file contains the time point of the last measured data (rounded to the nearest 10 minutes of the hour). The 10-minute data file is transmitted to the HMS FTP server every 10 minutes.

There are seven Python programs which run continuously on the mini-PC (Fig. 6). Three correspond to the LIDAR measurements (purple rectangles in Fig. 6) and the other four programs handle the CR10X, CS125, and surface data (yellow, blue, and green rectangles in Fig. 6). Three programs collect data from the three different instruments. The LIDAR and the CS125 instruments are queried to send data to the mini-PC in every minute (polling mode). Data sent by the instruments are appended to 10-minute data files. Downloading data from the CR10X data logger is only necessary every 10 minutes. Two programs main task is to send data to the HMS server every 10 minutes. LIDAR data files are forwarded as they are received from the instrument but the CR10X and the CS125 data files need to be processed before transferring. The so-called surface data processor and sender program decodes the data, performs the above-mentioned merging, and sends the surface data files to the HMS. Two other programs are used to plot data and transfer pictures to the web server of the observatory (nckobs.hu) every 10 minutes. At the end of the day, these programs archive data files by zipping and sending them to a NAS2 located at the EPSS in Sopron. Daily image files showing the visualized measured data are also transferred to the NAS2 and the nckobs.hu server.

Visualization of Data

The plots produced by the programs described above are published on the Observatory's website in the Data, Meteorological measurements page (Meteorological data at nckobs.hu, 2022). This section is about the information displayed in the figures. The title on all figures contains the first and last time points of the displayed data. It helps following the measurements realtime: the graphs are updated every 10 minutes, and the latest time will also change. If the last time does not change, it indicates that there is a problem with the system (e.g., a measurement stops, or the internet goes down, etc.).

LIDAR Plots

Two figures are produced using LIDAR data. The first one shows the actual data and the second one shows two auxiliary variables for monitoring the state of the instrument.

The first figure consists of three subplots (Fig. 7) showing data which are essential for determining the so-called fair-weather conditions for interpreting PG measurements (Harrison and Nicoll, 2018). One of the fair-weather criteria is no stratus or stratocumulus clouds below 1500 m. Therefore, the 1500 m height above ground level is marked on the first two panels of this figure.

Cloud Base Data The top panel of Fig. 7 shows the instantaneous cloud base data calculated from the individual backscatter profiles. Three cloud layers can be distinguished this way. The latest cloud height values are shown in the legend.

Sky Condition Data The second panel of Fig. 7 shows sky condition data: cloud base and cloud cover. The cloud cover is given in octas, which shows how many eighths of the full spherical angle of the sky are covered by clouds. These values are calculated from backscatter data of the latest half an hour with cloud data in the previous 10 minutes given an extra weighting. The sky condition algorithm is described in the manual of the instrument (SkyVUE PRO manual, 2022). Five cloud layers can be distinguished by this method with the SkyVUE PRO LIDAR. If there was detected cloud cover at the time of the last measurement, its data are also shown in the "Latest cloud data" text box in the figure.

Attenuated Backscatter Profile The bottom panel of Fig. 7 shows the attenuated backscatter profile data. The beginning of 31st August 2022 was calm and clear. The green area near the surface is the planetary boundary layer (PBL, Hayden and Pielke, 2016). The PBL is usually thinner during the day than at night. It was about 2000 m during the night and less than 1000 m during the day on 31st August.

Another difference between nighttime and daytime is the strength of the backscattered signal at the upper levels of the observed air column which is greater during daytime. It can be caused by the Sun because its radiation also includes near-infrared light which is used by the LIDAR, and this can increase the overall power of the signal that is detected by the sensor of the LIDAR.

The mostly sunny weather changed during the day. The clouds can be identified on the attenuated backscatter profile as red spots/areas. The persistent precipitation appears as yellowish–reddish formations over large areas after 17 UTC. For technical reasons, the backscattered signal strength is very low above the rain clouds (white area).

Auxiliary Variables The second plot shows two auxiliary variables (Fig. 8). The temperature of the laser (top panel) is usually 40 °C. The LIDAR has a heater so if the weather conditions make necessary it heats the laser up to 80 °C to avoid condensation and freezing of atmospheric moisture on the window.

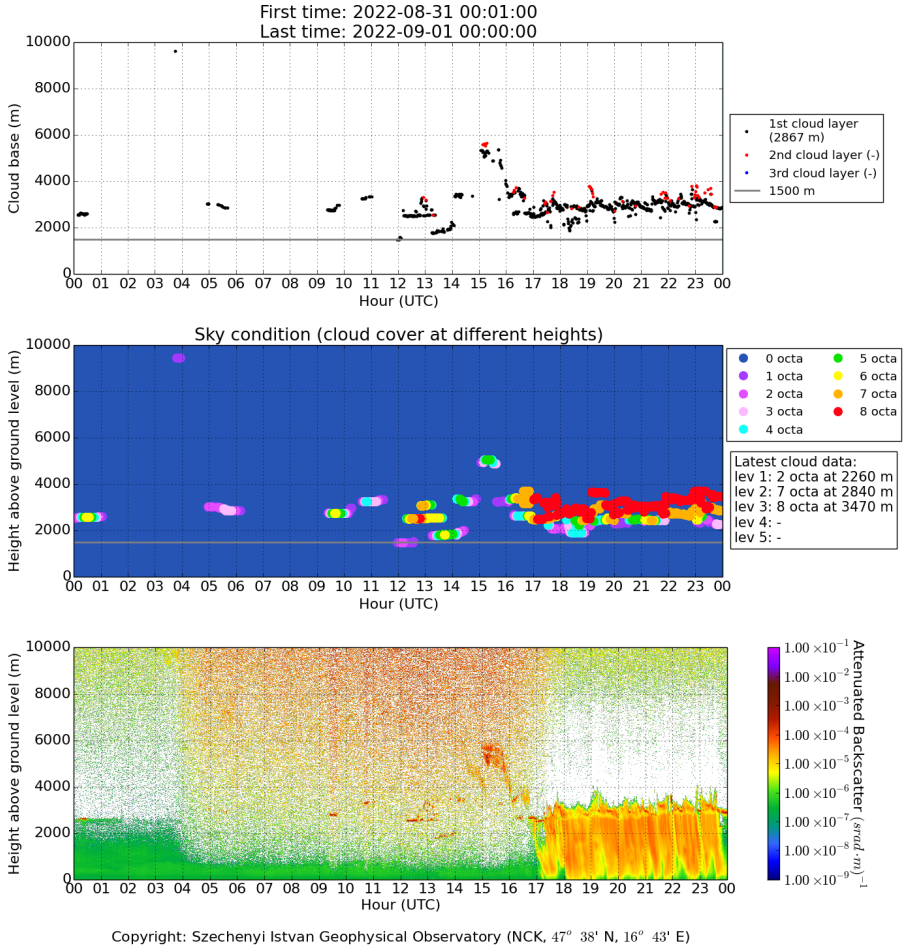

Fig. 7. LIDAR data measured at NCK on 31st August 2022: instantaneous cloud bases (top), sky condition (center) and attenuated backscatter profile (bottom).

The second variable is the LIDAR window transmission (bottom panel). The window of the instrument must be cleaned when the transmission drops below 80%.

Present Weather, Visibility, and Precipitation

The CS125 can count the number and measure the speed and size of particles falling in its detecting volume. The HygroVUE5 temperature and relative humidity probe which is connected to the CS125 provides data which is used to improve the discrimination between frozen and liquid precipitation. Based

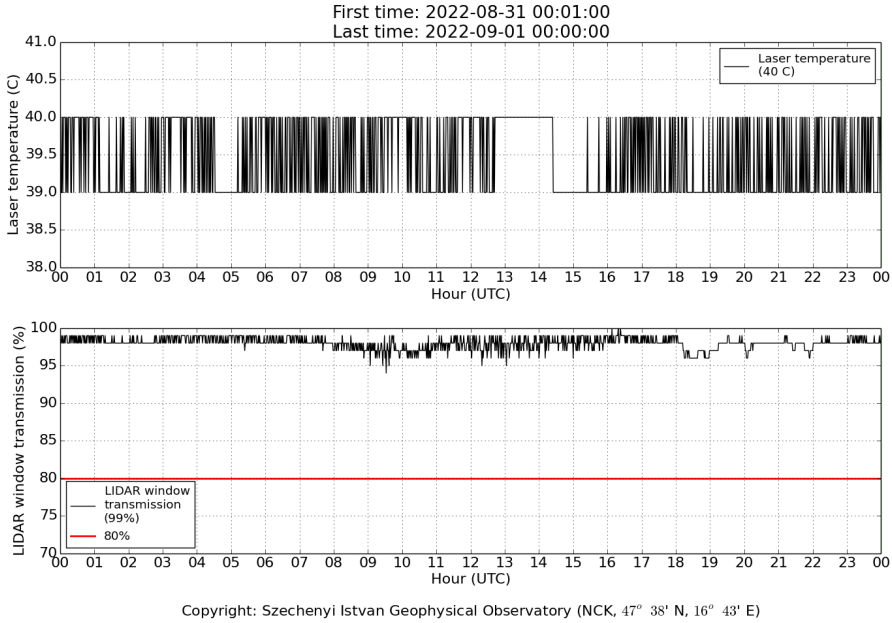

Fig. 8. Auxiliary variables obtained from LIDAR telegram at NCK on 31st August 2022: laser temperature (top) and LIDAR window transmission (bottom).

on these data the sensor can determine the following quantities: *a)* so-called present weather which is a description of the weather phenomena present at the time of observation, *b)* visibility, and *c)* intensity of precipitation.

Present weather data obtained from the CS125 is shown in the upper panel of Fig. 9. The background of the plot is colorful. The different colors correspond to different phenomena which are described in the legend above the plot. Rain is marked in green, snow in blue. Categories that may include solid or liquid precipitation (drizzle, precipitation, shower) are indicated in pink or purple. The thunderstorm category is yellow because of the lightning occurring in thunderstorms. The red line is the present weather reported as SYNOP code (WMO, 2019). Zero value means no significant weather. The precipitation which can be seen in the LIDAR backscatter plot (Fig. 7, bottom panel) is also detected by the CS125. The latest values are shown in the legend in parenthesis: the first value is the SYNOP code (in category /SYNOP code/ format) and the second value, after the comma, is the METAR code. The -DZ means light intensity drizzle. Further description about METAR codes can be found in Milrad (2017) and in the Wikipedia METAR page (Wikipedia, 2022).

The timeseries of visibility is shown in Fig. 9 (second panel). During the rain at the end of 31st August 2022 the visibility was lower than before.

The bottom panel of Fig. 10 shows different quantities related to precipitation: *1)* precipitation intensity determined by the CS125 (orange), *2)* cumulated precipitation calculated from CS125 precipitation intensity with 15% uncertainty also marked (red) and *3)* cumulated precipitation measured by the ARG100 tipping bucket rain gauge and recorded by the CR10X data logger (black). One tilt of the ARG100 means 0.2 mm of precipitation, therefore 0.2 mm is included in the figure as a reference (grey). The precipitation for the day is summed from 00:01 UTC up to 00:00 UTC on the next day to obtain cumulated precipitation. Thus, from the legend of the end-of-day graph, it is possible to see how much precipitation fell that day: 2.6 mm or 3.32 mm fell on 31st August according to the ARG100 and the CS125, respectively. Between 17 and 18 UTC zero tilt was registered by the ARG100 but it was raining according to the CS125. The amount of rain was below 0.2 mm according to the CS125 and it did not saturate the tipping bucket, so the ARG100 did not detect it. This shows that the ARG100 is not strong in measuring small amounts of rain. If the amount of rain is less than 0.2 mm and it does not tip the tipping bucket and the water later evaporates, the precipitation is not recorded. The ARG100 has no built-in heating and is therefore not suitable for real-time measurement of snowfall if the snow can not melt when it falls down (e.g., if the surface temperature of the instrument is under 0 °C). Snow accumulates on the insect net at the top of the funnel and only flows down to the tipping bucket after melting, even days or weeks after the snowfall. It is also possible that the wind blows it off before it melts, or someone removes some or all of the snow from the top of the tipping bucket. This also leads to measurement errors. The ARG100 can produce false measurements even if it is pushed or clogged. However, there could be false precipitation indicated by the CS125 also, if spiders are weaving webs and moving around the sensor, or if light is reflected into the sensor from somewhere, or during cleaning the instrument. In suspicious cases, when the precipitation lasted only a few minutes according to CS125, it is recommended to check the LIDAR backscatter plot, because falling precipitation should be seen on that too. If there is nothing, maybe not even clouds, the precipitation is not real, it should be ignored and the person responsible must look at the instrument. These instruments need to be maintained regularly (e.g., every week). So it can be seen that both instruments have their drawbacks, but together they give a more reliable picture of current rainfall patterns than separately.

Other Surface Plots

Other variables from the so-called surface data files are global solar radiation, temperature, relative humidity (Fig. 10), and atmospheric pressure, wind speed as well as wind direction (Fig. 11). Data from the CS125 data files (HygroVUE5 data) are plotted with red lines in these figures. Other data from the CR10X data logger are plotted with black and blue.

Global solar radiation shows how much sunlight reaches the instrument. Its diurnal cycle is affected by different factors. The effect of trees shadowing the instrument can be seen between 04 and 06 UTC (Fig. 10, upper panel). The global solar radiation increases slowly from 04 to 06 UTC when the Sun rises but the trees shadow the instrument. After 06 UTC global solar radiation starts to increase rapidly when the Sun can shine directly at the instrument above the trees. Due to clouds passing between the Sun and the instrument around 09:30 UTC (see Fig. 7), global solar radiation is reduced. The sky was covered by clouds in the afternoon (lower global solar radiation), but there was a less cloudy period around 15 UTC (see Fig. 7) when the global solar radiation had a local peak on this day.

Both temperature and relative humidity showed a fairly characteristic diurnal cycle on 31st August (Fig. 10, second and bottom panel). The temperature values of the different instruments differ only slightly, while the difference between the two relative humidity data series is larger. The higher the relative humidity, the larger the difference between them. It is because the old Väisälä instrument (black lines) was last calibrated in 2017, but the HygroVUE5 is a factory calibrated, new instrument. This emphasizes the importance of regular calibration at least every few years.

The mean sea level pressure is shown in the top panel of Fig. 11. Wind speed and resultant wind speed is shown in the second panel of Fig. 11. The shading of the marks depends on the wind speed: the stronger the wind, the darker the marker. This is not an absolute scale. The meaning of the darkest color varies according to the values currently displayed. The data logger samples the instruments every 5 seconds (sampling rate = 5 s), including the anemometer. So, every 5 seconds we get a wind vector (with direction and magnitude). The data acquisition interval is 1 minute. This means that the CR10X collects wind vectors every 5 s for 1 minute. From these the data logger calculates the resulting vector. The so-called resultant wind direction and resultant wind speed is the direction and length of this vector, respectively. An illustration and more detailed description can be found in the CR10X data logger manual on page 11-2 (CR10X manual, 2022). The wind speed (blue dots on the second panel of Fig. 11) is the scalar sum of the length of the small wind vectors. If the wind directions variation is small or the wind speed is low, then the two wind speeds are close to each other. If the wind directions variation is high and/or the wind speed is also high, then the two wind speeds differ more.

Wind direction is shown at the bottom panel of Fig. 11. The shading of the marks depends on the wind speed in the same way as on the wind speed graphs. At the beginning of 31st August 2022, southerly winds blow. After sunrise, the wind started to be northerly. It is the effect of the Lake Fertő and it is called lake–land breeze circulation (Woodhams et al, 2022). This phenomenon is common at the observatory when the weather is not affected by fronts. After sunset, the water in Lake Fertő cools down more slowly than the coastal areas resulting in a temperature difference between the lake and the observatory. The

warmer air rises above the lake and the air mass is replenished from the coastal areas. This means light southerly winds during nighttime. After sunrise, the coastal area warms up more rapidly than the lake, the air rises above the coastal area and northerly winds start to blow. On the examined day, the nighttime southerly winds did not return after sunset because of a cyclonic wave which had brought the precipitation in the afternoon.

Summary

This study describes the development of the main meteorological station at the NCK observatory between 2017 and 2022: from manual data acquisition to producing online plots which are updated quasi-real time every 10 minutes. In addition to describing the new data acquisition and processing system, the relocation of the meteorological measurements, for it to be closer to the atmospheric electricity measurements they support, was also discussed. Moving to a more open location also meant that measurements became less disturbed by the surrounding trees. We briefly described the two main instruments which were recently purchased: the LIDAR ceilometer and the visibility and present weather sensor. This was followed by a description of the plots on the observatory's website. A day with calm weather during the first half of the day was presented. On this day, the so-called lake–land breeze was observed, too. During the second half of the day, a precipitation system reached the station, so the LIDAR plots showed how cloud cover and precipitation appear in the data.

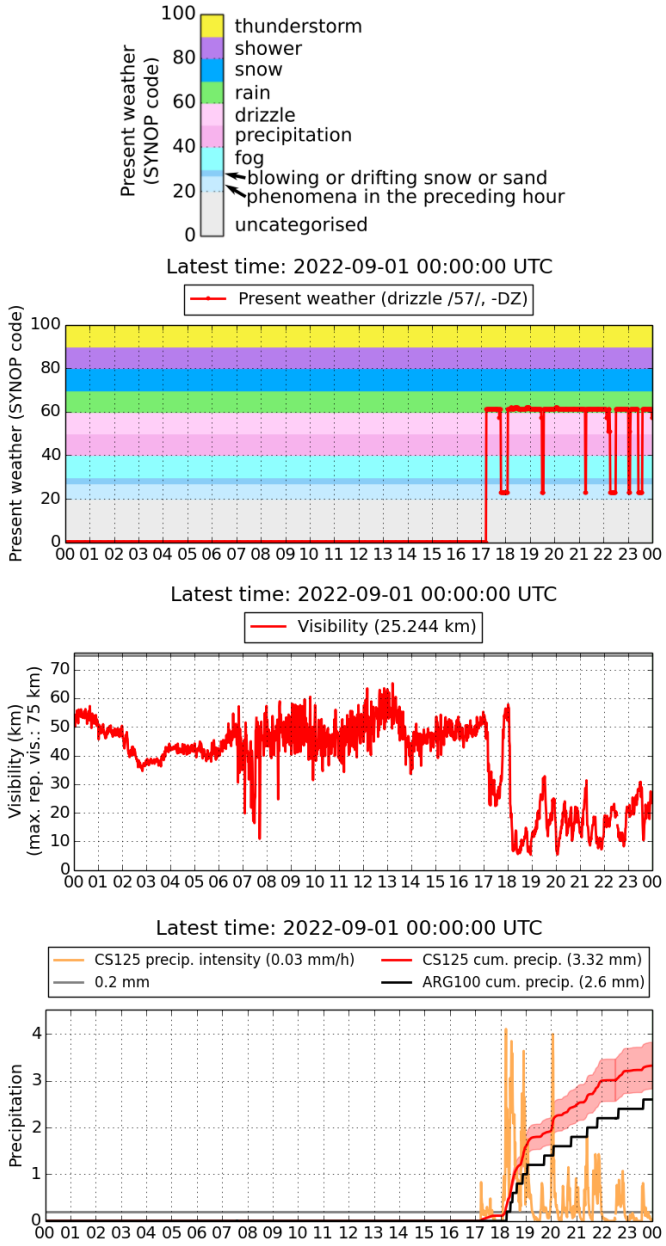

Fig. 9. Present weather (top), visibility (center), precipitation intensity (bottom, orange) and cumulated precipitation (bottom, red) obtained from the CS125 visibility and present weather sensor, and cumulated precipitation from the ARG100 tipping bucket rain gauge (bottom panel, black) at NCK on 31st August 2022.

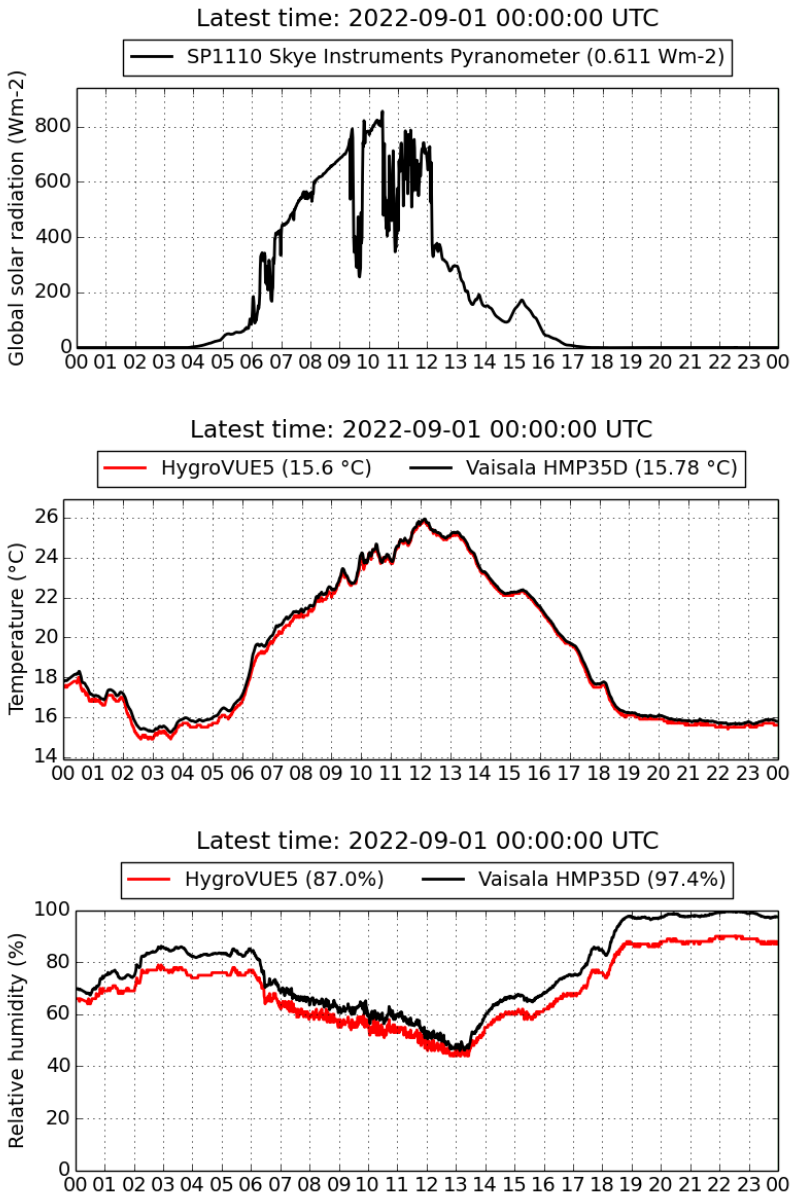

Fig. 10. Global solar radiation (top), temperature (center) and relative humidity (bottom) data at NCK on 31st August 2022.

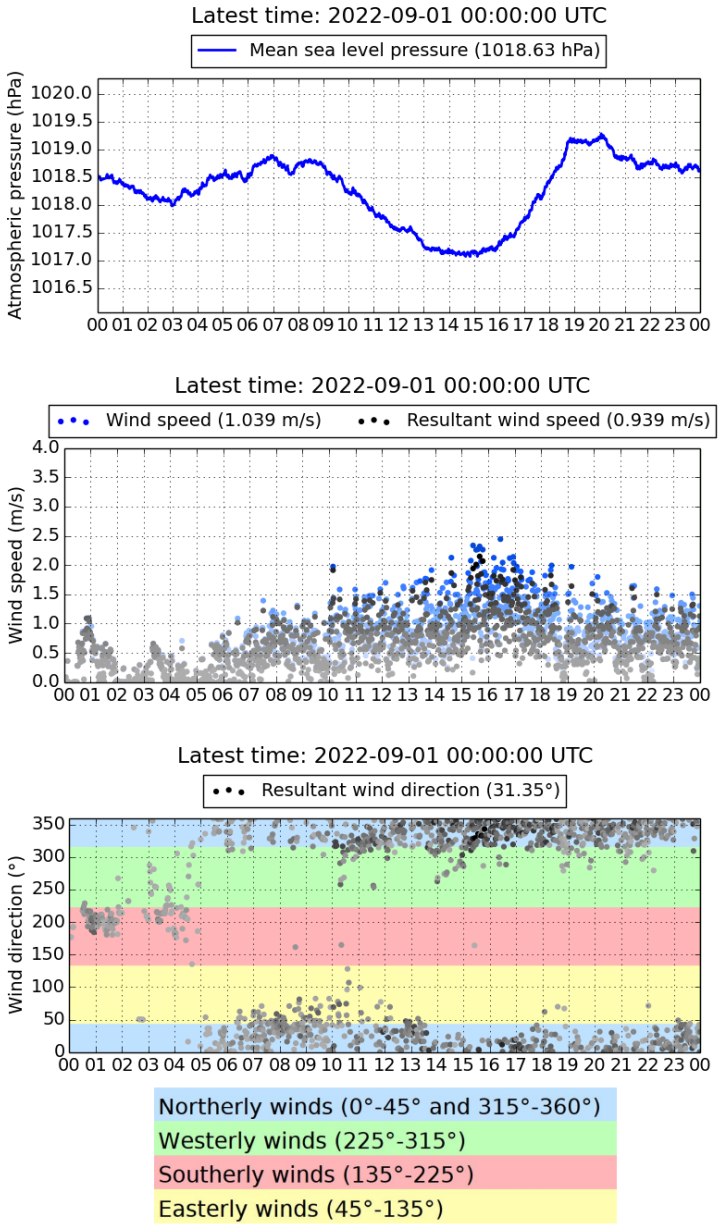

Fig. 11. Mean sea level pressure (top), wind speed (center) and wind direction (bottom) data at NCK on 31st August 2022.

Acknowledgements

This research has been supported by the National Research, Development and Innovation Office, Hungary (NKFIH; grant No. K138824) and the INFRA tender of the Eötvös Loránd Research Network (ELKH) in 2021. The authors would like to thank the collaboration opportunity and the assistance of the Hungarian Meteorological Services colleagues: Kornélia Radics, Gyula Horváth, István Sebők, Rita Hodossyné Rétfalvi and Hajnalka Baksáné Szini.

References

05103-LC (2022). Homepage of the Young Wind monitor (05103-LC). Available at: https://www.campbellsci.com/05103-lc. (Accessed: 21 October 2022).

ARG100 brochure (2022). Brochure of tipping bucket rain gauges. Available at: https://s.campbellsci.com/documents/ca/product-brochures/arg100-sbs500_br.pdf. (Accessed: 21 October 2022).

CR10X manual (2022). Manual of the CR10X data logger. Available at: https://s.campbellsci.com/documents/us/manuals/cr10x.pdf. (Accessed: 18 October 2022).

CS125 (2022). Homepage of the CS125 visibility and present weather sensor. Available at: https://www.campbellsci.com/cs125. (Accessed: 21 October 2022).

E-profile (2022). Available at: https://e-profile.eu/#/cm_profile. (Accessed: 18 October 2022).

EPSS news (2022). The technical handover of the Zero Magnetic Field Laboratory took place on 30 June 2022. https://epss.hu/en/magneses-nullter-laboratorium-muszaki-atadasa/ (Accessed: 21 October 2022).

Geophysical Observatory Reports, 1999–2001 (2003). Available at: https://gor.epss.hu/issues/GOR1999-2001/.

Harrison, R. G. and Nicoll, K. A. (2018). Fair weather criteria for atmospheric electricity measurements. *Journal of Atmospheric and Solar–Terrestrial Physics*, 179, 239–250. Available at: https://doi.org/10.1016/j.jastp.2018.07.008.

Hayden, B.P. and Pielke, R.A. (2022). Planetary boundary layer. *Encyclopedia Britannica*. Available at: https://www.britannica.com/science/planetary-boundary-layer. (Accessed: 21 November 2022).

HMP35D manual (2022). Manual of the Väisälä HMP35D humidity and temperature probe. Available at: https://s.campbellsci.com/documents/us/manuals/vaisala_hmp35a_manual.pdf. (Accessed: 21 October 2022).

HygroVUE5 manual (2022). Manual of the HygroVUE5 temperature and relative humidity sensor. Available at: https://s.campbellsci.com/documents/eu/manuals/hygrovue5%20-%201306.pdf. (Accessed: 21 October 2022).

Meteorological data at nckobs.hu (2022). Meteorological measurements at the Széchenyi István Geophysical Observatory website. Available at: https://nckobs.hu/data/met/. (Accessed: 18 October 2022).

Milrad, S. (2017). Synoptic Analysis and Forecasting: An Introductory Toolkit. *Elsevier*. Available at: https://doi.org/10.1016/C2015-0-05604-0.

PTB110 manual (2022). Manual of the CS106 Barometric Pressure Sensor (Väisälä PTB110). Available at: https://s.campbellsci.com/documents/us/manuals/cs106.pdf. (Accessed: 21 October 2022).

SkyVUE PRO manual (2022). Manual of the SkyVUE PRO ceilometer. Available at: https://s.campbellsci.com/documents/us/manuals/skyvuepro.pdf. (Accessed: 18 October 2022).

SP1110 (2022). Homepage of the Skye Instruments Pyranometer (SP1110). Available at: https://www.campbellsci.eu/sp1110. (Accessed: 21 October 2022).

Wikipedia (2022). METAR weather codes. Available at: https://en.wikipedia.org/wiki/METAR#METAR_weather_codes. (Accessed: 18 October 2022).

WMO (2019). WMO code table 4680: Present weather reported from an automatic weather station. In *Manual on codes: International Codes*, WMO Report No. 306, Geneva, Switzerland, A-360–A362. Available at: https://library.wmo.int/doc_num.php?explnum_id=10235#page=384.

Woodhams, B. J., Barrett, P. A., Marsham, J. H., Birch, C .E., Bain, C. L., Fletcher, J. K., Hartley, A. J., Webster, S. and Mangeni, S. (2022). Aircraft observations and sub-km modelling of the lakeland breeze circulation over Lake Victoria. *Quarterly Journal of the Royal Meteorological Society*, *148*(743), 557–580. Available at: https://doi.org/10.1002/qj.4155.

Determining the Amplitude Transfer Function of the Permanent Magnetic ELF Measurements of the Széchenyi István Geophysical Observatory

Tamás Bozóki[1*], József Bór[1], Karolina Szabóné André[1], Dániel Piri[1], Attila Novák[1], Csaba Molnár[1] and Gabriella Sátori[1]

[1]HUN-REN Institute of Earth Physics and Space Science, Sopron, Hungary

Abstract

In July 2020, a detailed ELF/VLF noise test was carried out in the Széchenyi István Geophysical Observatory. This test included the temporary installation of a pair of LEMI-type induction coil magnetometers that run from a battery during the test period (9 July 2020) when the power supply of the observatory was gradually shut down. As the temporary coils were installed two days before the test day (7 July) and continued to operate until the 13rd of July, there were several days when both the permanent and temporary systems were in operation. In this study, we use this overlapping period to further investigate electromagnetic noises present in the observatory and to determine the amplitude transfer function of the permanent ELF-band recording system based on the calibrated temporary measurements.

Keywords: extremely low frequency, Schumann resonance, induction coil.

Introduction

Recording of the atmospheric magnetic field in the extremely low frequency (ELF) band (3 Hz–3 kHz) began in November 1996 in the Széchenyi István Geophysical Observatory (NCK) near Nagycenk, Hungary (Sátori et al., 2013; Bór et al., 2020). A pair of locally built induction coil magnetometers were buried about 1 m below the ground in a non-magnetic chamber. These coils record the two horizontal components of the magnetic field in the geographic north–south (NS) and east–west (EW) directions. In November 2016 the original EW coil had to be replaced by a LEMI-120 type magnetic antenna (Bór et al., 2020).

*Corresponding author: Tamás Bozóki (bozoki.tamas@epss.hun-ren.hu)

Citation: T. Bozóki, J. Bór, K. Szabóné André, D. Piri, A. Novák, Cs. Molnár and G. Sátori (2025): Determining the Amplitude Transfer Function of the Permanent Magnetic ELF Measurements of the Széchenyi István Geophysical Observatory. *Geophysical Observatory Reports, 2023–2024*, 41–49. https://doi.org/10.55855/gor2024.3

On the 9$^{\text{th}}$ of July, 2020 a detailed noise test was carried out at the NCK, which is described in detail in the paper by Bozóki et al. (2021). The measurements of the observatory, the power supply of buildings and solar panels as well as charging of the batteries were gradually shut down and finally the main power supply of the observatory was interrupted. In order to survey changes in the electromagnetic (EM) noise environment during the test period, a pair of LEMI-type induction coil magnetometers, running on batteries, were installed near the permanent magnetic measurements on the 7$^{\text{th}}$ of July and continued to operate until the 13$^{\text{rd}}$ of July. This means that there were 7 days when both the permanent and temporary systems were in operation (except the ∼3 hour long period when the noise test took place). This overlapping period is used in this study to further investigate EM noises present in the observatory and to determine the amplitude transfer function of the permanent magnetic measurements based on the calibrated LEMI-type antennas used in the temporary measurement.

Description of the Measurements

At the time of the noise test, permanent ELF-band measurements of the two horizontal magnetic field components were made by two different induction coils. The NS field component has been measured by a locally manufactured induction coil that, before its current utilization, used to serve audio-magnetotelluric measurements. The signal at the output of the antenna is conditioned by a pre-amplifier placed near the coil, and led to the main amplifier which is located in a wooden house about 60 m away from it. The EW component was measured by a LEMI-120 induction coil that substitutes the other locally fabricated magnetic antenna which is broken. The LEMI-120 coil is also buried in the soil about 10 m from the wooden house. It has a built-in pre-amplifier with a balanced signal output. This signal of the antenna is connected to the other (unbalanced) input channel of the main amplifier using a balanced-unbalanced adapter. The main amplifier contains a hardware low pass filter with a cut-off frequency of about 38 Hz and a notch filter centered at 50/3 Hz to suppress the corresponding narrow-band noise from the railway lines running in Austria, relatively close to the observatory. The measured signal at the output of the main amplifier is then sampled at 500 Hz and archived for further processing.

Note that the last time the original recording system was calibrated was in 2008. During the calibration, the induction coil was put in the center line of two calibrating Helmholz coils. Magnetic fields of different amplitudes and frequencies were created by switching different electrical currents onto the calibrating coils. The signal (voltage) at the output of the main amplifier was recorded, so the transfer characteristics of the whole system were determined. Individual parts of the system have not been examined separately. Aging of the electronics in the original pre-amplifier and main amplifier could somewhat modify the transmission characteristics of the system in the time that has passed since the

last calibration. Additionally, the response function of the system, as a whole, has become practically unknown in the EW data channel when the original induction coil was replaced by the LEMI-120 antenna. The transfer function of the LEMI-120 antenna is known, so attempts were made to determine the transfer function of the system by measuring the response of the main amplifier alone. However, contradictory results were found when the full transfer function of the system, obtained this way, was applied. The noise test in the observatory with the parallel ELF-band magnetic measurements installed provides a good opportunity to determine the amplitude transfer function of the hybrid-state permanent recording system.

The temporary magnetic measurements were carried out with LEMI-120 type magnetic antennas that were run from a battery and were placed at a distance of about 50 m from the permanent measurements. The sampling frequency of the system was set to 500 Hz. These coils were oriented towards the geomagnetic NS and EW directions. Transforming the recorded data to components corresponding to the geographic NS and EW directions was done by applying digital rotation with the actual declination value (4.6°) in July 2020 determined by the absolute magnetic field measurements of the observatory (Lemperger et al., 2021). The temporary measurements were corrected for the transfer function of the coils (provided by the LEMI company) and are regarded as the absolutely calibrated reference data in this study.

Results

Figures 1-6 show dynamic spectra corresponding to the permanent and temporary magnetic measurements in the 7–13 July period (except the test day). Both measurements show that the magnetic field is highly contaminated by different noises at NCK and that this noise contamination is stronger in the H_{NS} field component. The first three modes of Schumann resonances at around 8, 14 and 20 Hz can only be identified in certain calm periods (like the afternoon hours on 12 July) primarily in the EW field component. It can be clearly seen in these figures that the permanent measurements include a notch filter at ∼16.6 (= 50/3) Hz which aims to suppress the characteristic narrowband noise from Austrian railway lines (Bór et al., 2020) and that there is a low pass filter above ∼38 Hz in the permanent measurements which is not present in the temporary measurements. A number of narrowband noises can be identified in the figures, some of which are continuous, some of which are transient but appear regularly, and some of which are of changing frequency. Low frequency (< 5 Hz) wideband noises appear as well which sometimes reach the lowest Schumann resonance mode at ∼8 Hz. It is to be noted that narrowband noises with changing frequencies were detected in the H_{EW} component by the permanent system which are usually not observed by the corresponding coil of the test measurements. The reason for this observation needs to be clarified in the future.

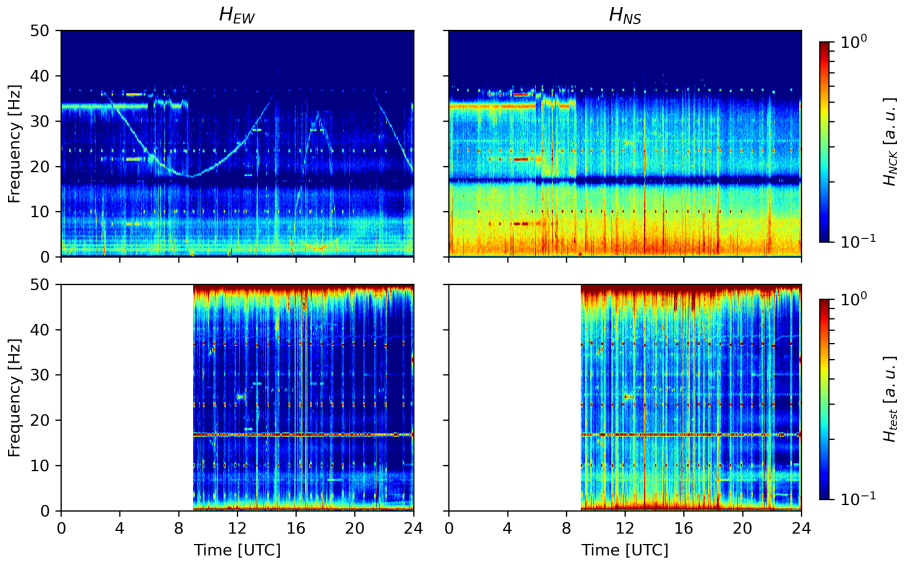

Fig. 1. Dynamic spectra corresponding to the H_{EW} (left column) and H_{NS} (right column) field components from the 7th of July, 2020 measured by the permanent (upper row) and the temporary (bottom row) magnetic measurements.

From the 4 days with complete records in both measurements (8, 10, 11, 12 July) 1-min average amplitude spectra were determined (window type: Hann, window length: 2048, window overlap: 1024) and the ratio of amplitude spectra corresponding to the two systems were calculated for the two field components separately. The most probable values of the ratio spectra were estimated based on the `gaussian_kde` function of the `scipy.stats` python package. These curves were resampled for the 2 Hz–40 Hz frequency range with 0.2 Hz frequency resolution and smoothed by applying a Savitzky–Golay filter (window length: 21, polynomial order: 3). The following frequency bands containing strong, narrowband noise (probably of local origin) were excluded before smoothing: 2.9–4.4 Hz, 6.5–8.8 Hz, 9.5–10.3 Hz, 10.7–11.3 Hz, 22.7–23.7 Hz, 24.4–25.7 Hz, 28.5–29.3 Hz, 29.7–34.7 Hz, 36.1–37.9 Hz. Finally, the ratio values at 8 Hz were selected as the calibration coefficients and all the curves were normalized with these coefficients in order to arrive at the dimensionless amplitude transfer functions. The calibration coefficients are $3.439{\cdot}10^{-5}$ and $3.766{\cdot}10^{-5}$ pT/digital unit for the H_{NS} and H_{EW} field components, respectively.

Figure 7 shows the whole collection of normalized ratio spectra as well their most probable values and the smoothed and resampled curves. If we consider the temporary measurements to be properly calibrated, these curves represent the amplitude transfer functions of the permanent measurements. The ampli-

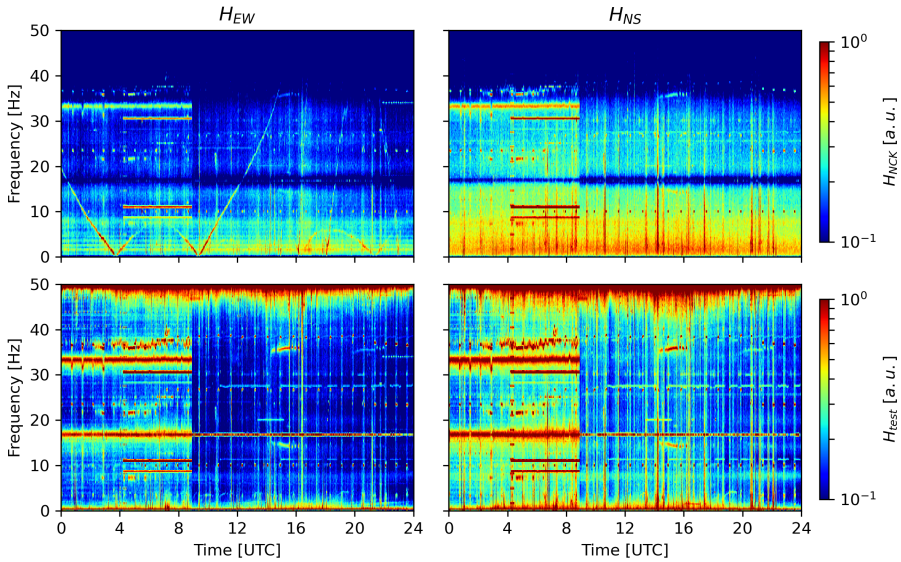

Fig. 2. The same as Fig. 1 but for the 8$^{\text{th}}$ of July, 2020.

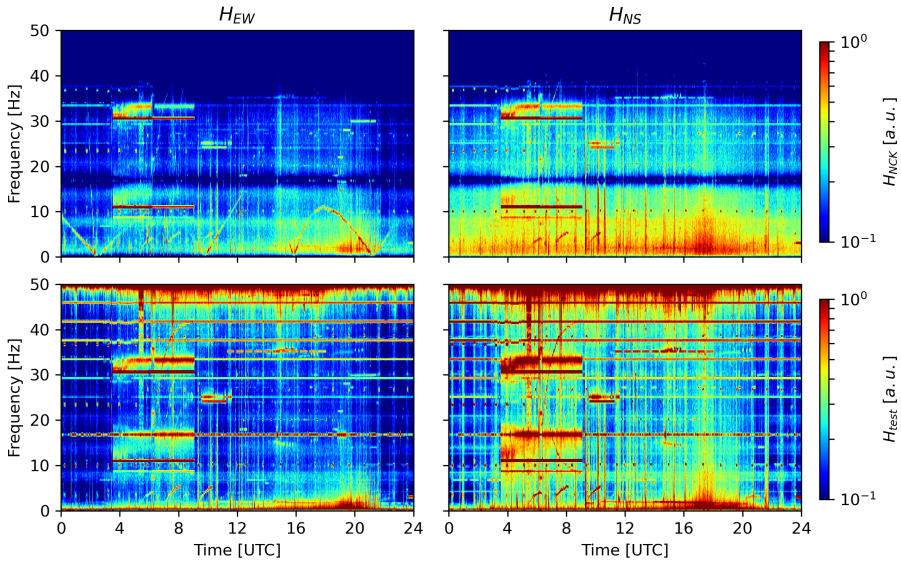

Fig. 3. The same as Fig. 1 but for the 10$^{\text{th}}$ of July, 2020.

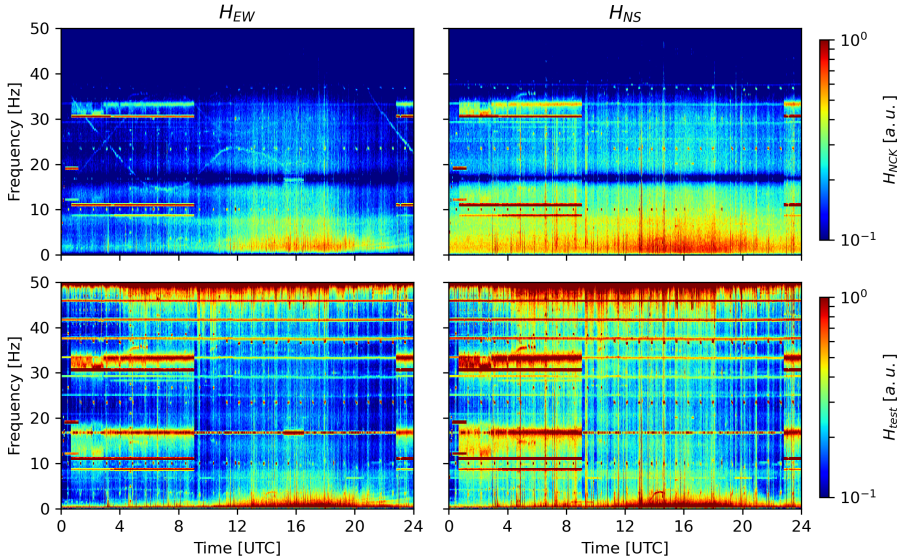

Fig. 4. The same as Fig. 1 but for the 11$^{\text{th}}$ of July, 2020.

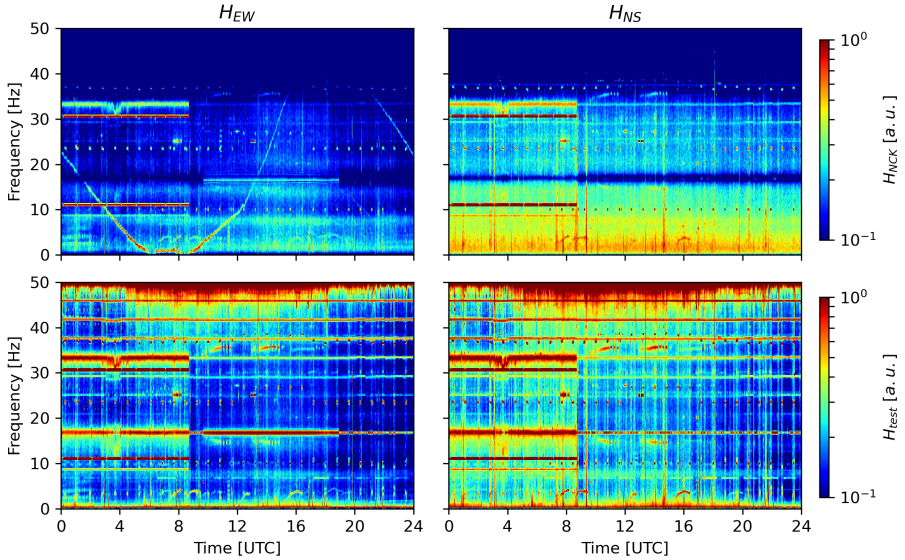

Fig. 5. The same as Fig. 1 but for the 12$^{\text{th}}$ of July, 2020.

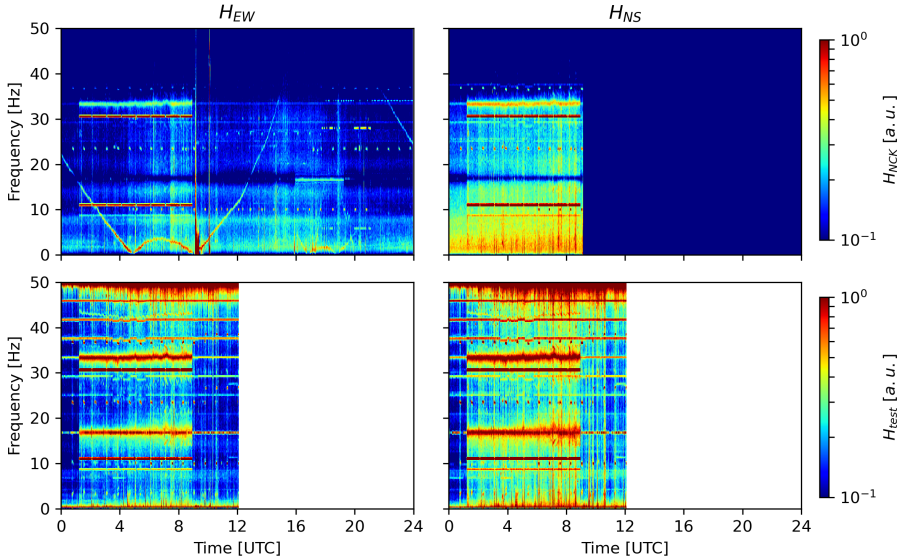

Fig. 6. The same as Fig. 1 but for the 13$^{\text{th}}$ of July, 2020.

tude transfer functions show a large notch at around 16.6 Hz and a strongly decreasing trend above 30 Hz, consistent with the differences between the systems (as discussed earlier). It is also noticeable that while the amplitude transfer function corresponding to the H_{EW} field component is practically flat in the 5–30 Hz frequency range, this is not true for the H_{NS} field component. This difference can be explained by the fact that the H_{EW} component is measured by a LEMI-type induction coil in the permanent system while the H_{NS} component by the original, locally manufactured coil.

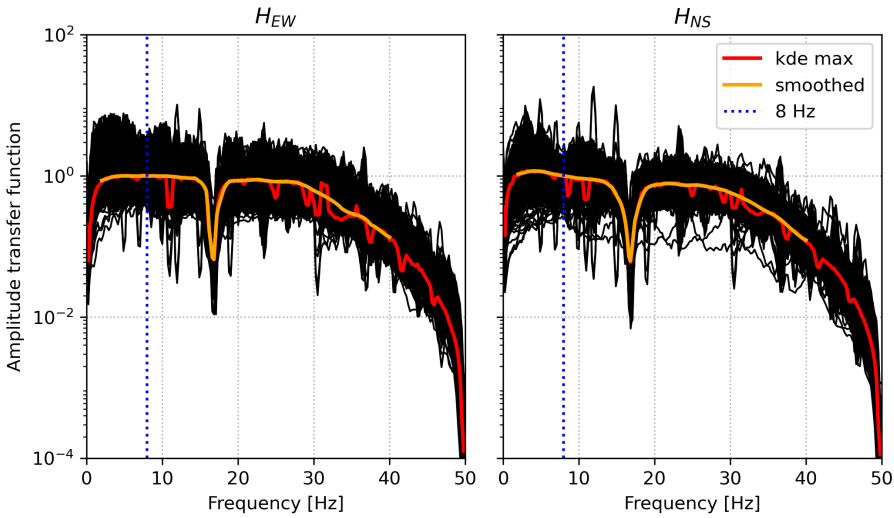

Fig. 7. The normalized ratio of 1-min average amplitude spectra corresponding to the temporary and the permanent measurements (black) and the most probable values of these ratios as provided by kernel density estimation (red). The orange curves represent the smoothed and resampled versions of the red curves and are regarded as the actual amplitude transfer functions. Certain frequency bands containing strong, narrowband noise were excluded before calculating the smoothed amplitude transfer function.

Acknowledgements

This work was supported by the National Research, Development, and Innovation Office, HungaryNKFIH, project numbers K138824 and PD146019. The contribution of T.B. was also supported by the János Bolyai Research Scholarship of the Hungarian Academy of Sciences (BO/00352/24).

References

Bór, J., Sátori, G., Barta, V., Szabóné-André, K., Szendrői, J., Wesztergom, V., Bozóki, T., Buzás, A., & Koronczay, D. (2020). Measurements of atmospheric electricity in the Széchenyi István Geophysical Observatory, Hungary. *Hist. Geo Space Sci.*, **11**(1), 53–70. https://doi.org/10.5194/hgss-11-53-2020

Bozóki, T., Bór, J., Piri, D., Novák, A., & Molnár, Cs. (2021). ELF Noise Test in the Széchenyi István Geophysical Observatory. *Geophysical Observatory Reports, 2020*, 14–17. https://doi.org/10.55855/gor2020.2

Lemperger, I., Szendri, J., Szabó, Cs., Kuslits, L., Kis, Á., Szalai, S.M., Molnár, Cs., & Wesztergom, V. (2021). Geomagnetic observation system in the

Széchenyi István Geophysical Observatory. *Geophysical Observatory Reports, 2020*, 26–34. https://doi.org/10.55855/gor2020.4

Sátori, G., Rycroft, M., Bencze, P., Märcz, F., Bór, J., Barta, V., Nagy, T., & Kovács, K. (2013). An Overview of Thunderstorm-Related Research on the Atmospheric Electric Field, Schumann Resonances, Sprites, and the Ionosphere at Sopron, Hungary. *Surv. Geophys.*, **34**, 255–292, https://doi.org/10.1007/s10712-013-9222-6

Testing the Suitability of an Unenergized Power Line Near Szakony, Hungary for Measuring the Air-Earth Electric Current

József Bór[1]*, Earle R. Williams[2] and Dániel Piri[1]
[1]HUN-REN Institute of Earth Physics and Space Science, Sopron, Hungary
[2]Parsons Laboratory of the Department of Civil and Environmental Engineering, Massachusetts Institute of Technology, Cambridge, MA, USA

Abstract

The global activity of tropospheric sources of atmospheric electricity can be monitored by near-surface measurements of the parameters of the atmospheric global electric circuit. Measuring the air-Earth vertical electric current on long power transmission lines in fair weather conditions promises an applicable solution for that purpose. The implementation of such a measurement is considered and an unenergized power distribution line of 14.5 km length near western border of Hungary was examined to determine whether it is suitable for further investigations. It was found that a 2.2 km-long segment of the line might be used for that after further testing. This report summarizes the experiences of the first testing of the line, including theoretical considerations on the expected magnitude of the electrical quantities that can be measured on the line and performance of the applied tools and measuring devices. Practical guidelines for selecting the line and the measuring point on the line are derived and recommendations for further tests are given.

Keywords: global electric circuit, air-Earth electric current, power lines.

Introduction

Climate change is one of the global challenges that are critically relevant for humanity as it affects the fundamental areas of prospering of mankind: energy, land, agriculture, as well as basic conditions of living, most notably the temperature (Hardy, 2003). Several elements of the climate are cross-linked via the temperature, e.g. thunderstorm and lightning activity (Williams, 1992), global rainfall (Salzmann, 2016), etc. As thunderstorms and electrified shower clouds are the key drivers of the atmospheric global electric circuit (GEC) (Mach et al., 2011), monitoring of the GEC is a plausible tool for studying the interlinked

*Corresponding author: József Bór (Bor.Jozsef@epss.hun-ren.hu)
Citation: J. Bór, E. R. Williams and D. Piri (2025): Testing the Suitability of an Unenergized Power Line Near Szakony, Hungary for Measuring the Air–Earth Electric Current. *Geophysical Observatory Reports, 2023–2024*, 50–68. https://doi.org/10.55855/gor2024.4

elements of the climate. The DC and AC parts of the GEC (Rycroft et al., 2008), however, have not been effectively utilized so far in this aspect.

Distinction between sources of the DC and AC global circuits is fundamentally important. Beginning with the new theory for the DC global circuit by C.T.R Wilson (1920), electrified shower clouds (precipitating clouds without lightning) are considered as important contributors to the air-earth current. This has been supported by satellite measurements (Liu et al., 2010) and it is also sustained by evidence from measurements of substantial cloud-top current to the DC global circuit by, e.g., Wilson (1920), Mach et al. (2009, 2010, 2011). More than 90% of worldwide precipitating convection (electrified shower clouds and thunderstorms combined) is recognized to contribute to the DC global circuit (Liu and Zipser, 2009). In contrast, only thunderstorms drive the AC global circuit and Schumann resonances (Price et al., 2007).

In attempting to characterize the global climate change via monitoring the GEC, we now focus on the DC part, because quantitative access to the DC global circuit in a globally representative measurement of air-Earth current on a continuous basis would enable access to the continuous variations of rainfall and latent heat release on a continental scale. This achievement would provide unprecedented access to global energetics on both weather and climate time scales. The currently available model-based estimates of the sensitivity of global rainfall to temperature (e.g., Salzmann, 2016) vary by nearly an order of magnitude, largely due to the uncertainty in the role of global aerosol in modulating the rainfall. These model predictions could be checked by this global electrical measurement. The measurements would likely provide a new impetus to global weather forecasting, too.

Reliable continuous access to the DC global circuit, involving all electrified weather worldwide, though pursued for more than a century, is still unsolved. Although some spot attempts have been carried out in special locations, e.g., Vostok, Antarctica (Burns et al., 2017), they are always subject to dominance by local effects and so are generally unsuccessful for continuous monitoring. This is especially true for measurements of the atmospheric electric potential gradient (Nicoll, 2012). Joint analysis of PG measurements recorded in fair weather conditions at well separated monitoring sites can be one workaround for this problem (Bór et al., 2023). The numerous unsuccessful attempts push forward an alternative new approach, which is based on the use of unenergized long transmission lines from an infrastructure already in place. Global representativeness is supposed to be achieved due to the mutual cancellation of local effects that vary along the long line. These lines can be fundamental from a technical point of view, too, because they increase the collection area of the air-Earth current by orders of magnitude over other earlier efforts (Ruhnke, 1969; Ruhnke et al., 1983; Tammet et al., 1996), and so they yield a sufficiently larger electric current which is relatively easier to measure.

This report serves to document the experiences gained during checking the suitability of a segment of an unenergized power line near Szakony, Hungary for making air-Earth current measurement on it.

The tested power line and its environment

We were informed that an unenergized power line runs between two settlements, Szakony and Sopronkövesd near the western border of Hungary (Fig. 1). It used to be a distribution power line of 22 kV. One end of the line (47.432872° N, 16.712734° E) is in Szakony. From there, it runs north-west for about 2.2 km before it takes a sharp turn to head to north-east. Along the first section, it runs quasi-parallel to another active distribution line of 22 kV that lays south-west from it. The distance between the two lines is only 20–100 m. Just before it turns to north-east at the point (47.448574° N, 16.693866° E) (Fig. 2), the unenergized line crosses a high voltage power distribution line of 132 kV (i.e. runs below it) which is running perpendicular to its section back towards Szakony. After turning to the northeast, the unenergized line runs quasi-parallel to the 132 kV active transmission line, partly on its right side, partly on its left side, and literally under it, too, along a short section (Fig. 3b). Close to Sopronkövesd, the tested line crosses an electrified railway line and takes another sharp turn to north-west again right after this (Fig. 1). It runs further in this direction for about 2 km before it terminates. Several active distribution power lines of 22–25 kV crosses the tested line or run parallel to it within a 20–100 m range along some sections.

The total length of the unenergized line is ∼14.5 km. The line consists of 3 wires for the 3 phases of the transmitted electric power. The wires are at about 10 m height above the ground level (pole heights are supposed to be within the 10–15 m range). At most supporting poles, which are placed spaced by 100 m each from one another, the central wire is elevated by 0.8 m from the two, lower running wires. The horizontal distance between the two lower wires is 1.4 m. A diameter of 12 mm can be assumed for each wire (the diameter of the wires applied in such distributing lines is between 9 mm and 14 mm).

It was discovered only in the middle of the testing process that the unenergized line was damaged between two poles, ∼1.3 km after it turns toward north-east. The two lower wires were torn off from the supporting pole at (47.457427° N, 16.704972° E) (Fig. 3a), while the upper wire remained intact. At the next pole towards the northeast at (47.459506° N, 16.707542° E), the two released wires were connected to the top wire and all of them were wound around the metal structure of the pole, i.e., they were more or less grounded (Fig. 3b). This means that all three wires of the rest of the line towards its end at Sopronkövesd were interconnected and were more or less grounded at this pole. On the other hand, from the previous pole all the way back to the

end at Szakony, the two lower wires were separated from the rest of the line, while the top wire was connected to the same, including all three wires, and the grounding point.

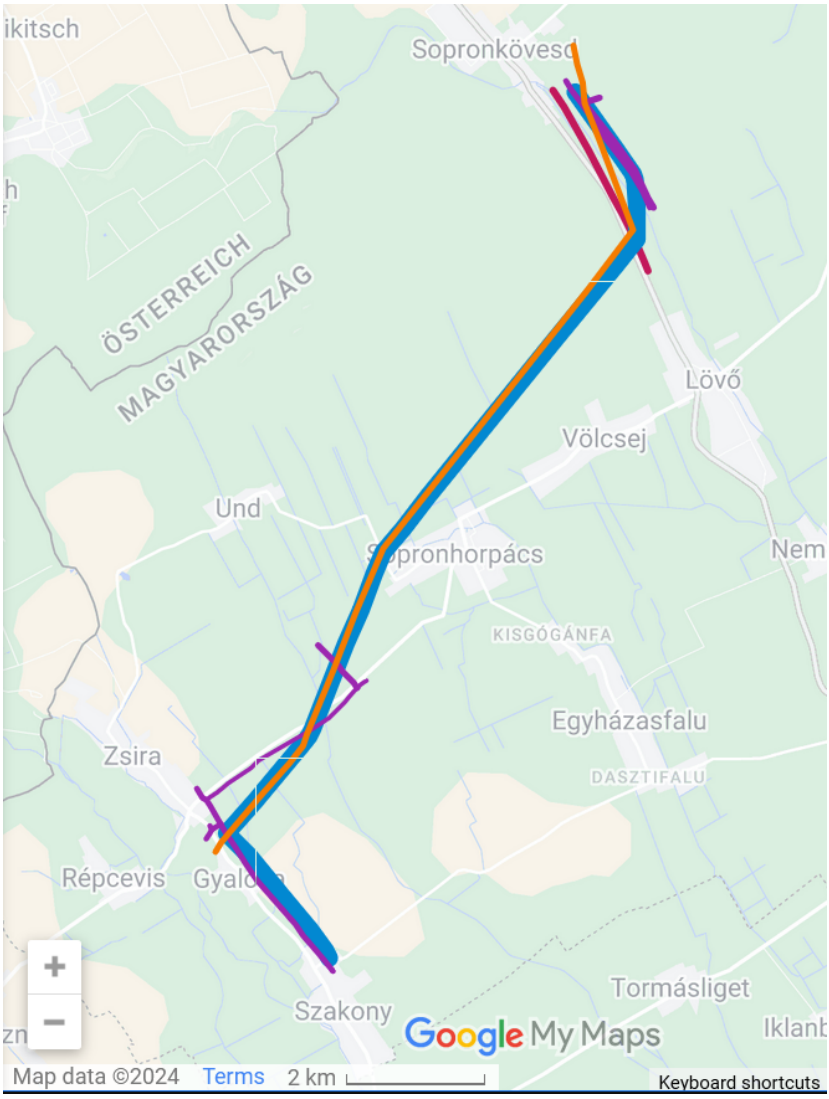

Fig. 1. Map of the tested unenergized power line (thick and blue) and the interfering sections of the power line network. 22 kV distribution lines (purple), 132 kV transmission line (orange), electrified railway line (red). The map is northward oriented. Google maps, 2024.

Fig. 2. Turning point of the tested power line, 2.2 km from its end in Szakony. The pole in the middle is equipped with a mechanical switch that allows breaking the continuity of the line.

Preparations for the testing, methodology

Voltage or current measurement?

The final goal of making measurements on a long transmission line is to infer the global state of the DC GEC. In principle, this can be achieved in two ways. As the power line runs in the air on insulating supporting poles, it acquires the potential of the background field at its elevation level, which, in fair weather conditions, is driven by the potential of the upper equalizing layer in the lower ionosphere (Rycroft et al., 2008). The voltage the line acquires represents the state of the DC GEC. Implementing this approach is both difficult and dangerous. A very long conducting line can collect a significant amount of charge and may come to a very large voltage of several kilovolts compared to the ground. Although the supporting poles are generally good insulators, even a small leakage current through them to the ground can bias the measurement. Given the unavoidable coupling of AC sources, both natural (e.g., lightning) and

Fig. 3. Discontinuity **(a)** and loose grounding **(b)** of the tested unenergized power line. The other line is a high voltage transmission power line of 132 kV.

man-made (e.g., nearby-running active power lines), to the measured line, it can be challenging to extract the DC part of a possibly highly varying voltage. This approach also requires a very sophisticated measuring device exhibiting very low leakage current and so a very high internal resistance that is comparable to the total resistance of the support of the line.

The other concept is to measure electric current that runs between the line and earth through a low-resistance ammeter, i.e., the air-Earth current. Since the line cannot gather a large potential in this approach, this solution is unquestionably safer to test. It also seems easier to realize because one needs to provide only a very good grounding for practically all of the current to flow in the measuring channel towards the ground. Nevertheless, implementing this variant is still challenging. Partly because the DC current to be measured is very small and weak, i.e. it comes from a source that has a very high internal resistance so it cannot drive conventional ammeters. And partly because the direction of the current may change due to the AC coupling to the line, and commercial ammeters in the micro-nanoampere regime normally can handle only monodirectional electric currents. Additionally, large current transients can easily damage electronics designed to be sensitive to very small DC currents. Considering the resources and measuring instruments that were available to us, we opted for checking the suitability of the unenergized line for making air-Earth current measurements on it.

Estimation of the electric parameters of the measured line

Initial calculations were made to estimate what we can expect at the measured line. At the estimation of the air-Earth current, ideal fair weather conditions and no AC coupling to the tested line were assumed. According to Tammet et al. (1996), the effective current collection area A (square meters) of a long horizontal wire of length L (meters), height H (meters) and wire radius R (meters), is given by the following equation

$$A_w = \frac{2\pi LH}{\ln(2H/R)}. \tag{1}$$

For one wire of the tested line, the parameters $L = 14500$ m, $H = 10$ m, and $R = 0.006$ m yield $A_w = 1.1 \cdot 10^5$ m^2. Taking the vertical current density to be $J = 2$ pA $= 2{\cdot}10^{-12}$ A/m^2 (Haldoupis et al., 2017), the air-Earth current on one grounded wire is $I_w = J{\cdot}A_w = 22.5{\cdot}10^{-6}$ A $= 22.5$ μA. The total current on the interconnected 3 wires will be less than triple of this value, because the wires are close to one another. The reduction due to the geometry of wire arrangement was not estimated, still the magnitude of the expected total current could be inferred. It should be a few tens of microamperes somewhere between 22.5 μA and 67.5 μA.

The voltage of the floating line U is simply the product of the vertical electric field E (the negative of the potential gradient) and the height of the line. In fair weather conditions, E is usually taken to be -130 V/m (Haldoupis et al., 2017). This yields -1300 V for a line at 10 m height. Note that under charged clouds, especially during thunderstorms, E can be more than two orders of magnitude larger which is dangerous both for humans and for the measuring electronics. Therefore, the testing should be carried out in fair weather conditions.

The total charge the line collects (Q) is the product of its voltage U and its capacitance C. Following the formula given by Tammet et al. (1996), the capacitance of a wire can be calculated using the formula

$$C_w = \frac{2\pi\epsilon L}{\ln(2H/R)}, \tag{2}$$

where ϵ is the permittivity of the air. Assuming this to be equal to the permittivity for free space $\epsilon_0 = 8.85 \cdot 10^{-12}$ F/m, the capacity of a wire of the line becomes $C_w = 9.34 \cdot 10^{-8}$ F $= 93.4$ nF. With this value, the largest charge on one wire of the line can acquire is $Q_w = 129$ μC, and so $Q = 388$ μC for the 3 wires combined.

The energy W_w stored on one wire can be calculated as $W_w = \frac{1}{2}C_w \cdot U^2$. For one wire this is $\sim$84 mJ. For the 3 wires combined, the value is $W = 252$ mJ, which is not necessarily lethal in fair weather conditions. However, in stormy weather the voltage can be 1–2 magnitudes larger and the energy can easily be within (or even over) the range applied in defibrillators, namely 120–360 J (Goyal et al., 2023), and so it can be dangerous to human life. This further

emphasizes that the test should be made in fair weather conditions and with precaution to avoid any electric shock to people.

On using a spark gap in the measurement

One easy solution for limiting the voltage of the wires is using a spark gap. The spark gap separation d (in mm) can be calculated as the ratio of the maximum allowed voltage U_{max} to the breakdown strength of air $U_{B,air}$. Note that $U_{B,air}$ is usually taken to be 3000 V/mm but it may vary depending on the geometry of the spark gap and environmental conditions, e.g., temperature, pressure, and humidity (Sankar, 2011). For example, if the voltage on the line is to be limited to $U_{max} = 1000$ V, a gap $d = U_{max}/U_{B,air} = 0.33$ mm should be set.

Note that a good spark gap is perhaps the simplest tool to verify whether the floating transmission line functions as expected. Sparks should occur regularly when the separation d is set below the distance that corresponds to the maximum reachable voltage of the line. The time τ (seconds) needed to fully charge the line capacitance from an initially discharged condition can be calculated as

$$\tau = \frac{Q}{I} = \frac{Q}{J \cdot A} = \frac{\frac{2\pi\epsilon LEH}{\ln(2H/R)}}{J\frac{2\pi LH}{\ln(2H/R)}} = \frac{\epsilon E}{J} = \frac{\epsilon}{\sigma}, \tag{3}$$

where $\sigma = J/E$ is the conductivity of air, which can be taken to be $\sigma = 2 \cdot 10^{-12}$ A/m^2 / 130 V/m = $\sim 1.54 \cdot 10^{-14}$ S/m. With this value, $\tau = 8.85 \cdot 10^{-12}$ F/m / $1.54 \cdot 10^{-14}$ S/m = $\sim$575 s or roughly 9.5 minutes. Note that τ does not depend on the parameters of the line. It is simply the local ambient relaxation time of the atmosphere. Because of the varying conductivity, the actual value of the relaxation time may differ from this estimation, but, depending on the applied spark gap separation, discharges in the spark gap should be observed regularly in every few minutes. Note that good insulation of the spark gap is very important in this application. Since the charging current of the line is very weak, surface current leakage of the spark gap can cause significant deviations from the theoretically expected operation.

Capacitive coupling to the measured line

Capacitive coupling between the tested line and nearby-running active transmission and distribution lines can be expected. The following considerations were made to quantify the conditions for the coupling to remain at a manageable level. Note that such calculations are relevant also from the point of view of safety when work is to be done close to high voltage lines (Luo et al., 2023). An active power line, a single wire of infinite length is assumed to run horizontally at the height H_A above the ground surface. It can be shown that the vertical component of the electric field of this active line and its mirror image under the

surface together (E_A) at a horizontal distance D from the line can be given by the formula

$$E_A = \frac{\lambda}{2\pi\varepsilon_0}\left(\frac{H_A - H}{D^2 + (H_A - H)^2} - \frac{H_A + H}{D^2 + (H_A + H)^2}\right) \tag{4}$$

(Reitz et al., 2008), where λ (C/m) is the momentary (but uniform) line charge density of the wire. The line charge density determines the radial electric field E_r at the surface of the wire (cable) through the relation

$$E_r = \frac{\lambda}{2\pi\epsilon R_A}. \tag{5}$$

Here R_A is the radius of the active wire. To obtain an upper limit for the line charge density, we take the radial electric field at the surface of the wire (cable) to be the breakdown strength of air $U_{B,air} = 3$ MV/m. Assuming that R_A is the same as that for the tested line, i.e. 6 mm, solving the relation for the line density yields $\lambda = 1.0 \cdot 10^{-6}$ C/m. We can use this value of λ in the expression for E_A. For the air-Earth current to be monopolar, E_A should not exceed the electric field near the Earths surface, i.e., 130 V/m. This expression can be solved either analytically or numerically for the minimal D which fulfills this condition. Table I contains the E_A values obtained for D varying between 40 m and 50 m, assuming that the active line runs at the same height as the tested line, i.e. at 10 m.

Table I. The vertical component of the electric field (E_A) of an infinite line of charge of 10^{-6} C/m line density at 10 m height at a horizontal distance D from it.

D (m)	40	41	42	43	44	45	46	47	48	49	50
E_A (V/m)	-180	-173	-166	-160	-154	-148	-143	-138	-133	-128	-124

It can be seen that the amplitude of the coupled AC voltage on the line in absolute value is less than the external fair weather field (130 V/m) only further than 49 m from the measurement on the tested line. This means that an active wire, as parameterized above, must be at least ∼49 m away from the measured line, but the further the better. If the line consists of 3 wires, with the distance between the phases (wires) taken as negligible compared to the distance between the lines, the minimum required distance is triple this value, i.e. 147 m. Note that this value is an upper limit for the minimum distance, and can be lower if the radial electric field at the surface of the active wire is less than the breakdown field of the air, which is usually so.

If the unenergized line is running parallel to the live line, the AC field estimates apply everywhere along the line. In the much more favorable circumstance that the unenergized line runs perpendicular to the live line, the calculated fields are present only at the end closest to the live line, and diminish substantially further along the line.

Note that an AC signal on the measured line can also be induced by transient electromagnetic wave packets travelling in the air. Such wave packets can originate from both natural (e.g., lightning) and man-made sources (e.g., electric motors or motors with a spark plug). These noise sources may occasionally produce very energetic electromagnetic transients, too. Moving away from areas of human activity can be a solution for eliminating man-made noise sources. Transients of natural origin, however, can always occur, so the measurement must be set up and interpreted accordingly.

Instrumentation used for testing the line

- A spark gap with an adjustable separation distance was manufactured locally. The two ends of the spark gap are separated by a rod of 40 mm diameter made of polyamide for insulation. Note that the surface current leakage of the spark gap could not be measured reliably with the equipment that was available for us.

- The Nanoranger ammeter by Altonovus was intended to be used for measuring small monodirectional currents (https://www.altonovus.com/nanoranger).

- A Voltcraft ET-02 device was used to measure the grounding resistance at the measuring point.

- A Voltcraft M-3860M digital multimeter and an analog oscilloscope (Tektronix 2213) was used to check the level of AC coupling on the measured line.

- All these devices were run on-site either on battery or on a battery-powered 220 V AC inverter.

Timeline of the testing and the observations

Initial measurements at the termination of the tested line in Szakony

The testing took place on January 17, 2024. There was some very weak, practically negligible wind. High level clouds fully covered the sky, but there were no low level clouds so the weather could be described as quasi-fair or semi-fair (Harrison et al., 2020).

The investigation was started at the terminating pole of the tested line (47.432872° N, 16.712734° E) in the village Szakony (Fig. 4). At that point, the line to be tested runs at a distance of about 60 meters from a parallel energized line of 3 phases at 22 kV AC (Fig. 1). The resistance of the grounding attached to the terminating pole was measured to be 13-14 Ω.

Fig. 4. Termination of the tested power line in Szakony. The three wires (phases) coming up from the ground and attached to the supporting pole are under power.

Measurements at the first test point

We learned that an active distribution line, in the continuation of the unenergized line, ends at the terminating pole (Fig. 4). Although it is well separated from the tested line, we were advised that it is not safe to work in the vicinity of the end of this active line. So we moved two pole distances (∼200 m) up the test line and made further investigation there at the pole (47.433954° N, 16.711779° E). The ground resistance was found to be 19 Ω at that pole. Using a cherry-picker truck, kindly provided by the energy networks and energy infrastructure company E.ON, high voltage on the wires was checked for safety precautions (Fig. 5a). No significant voltage was found. Then the three phases (wires) of the line were combined using special clamps and all were linked to one down-going cable (Fig. 5b). The wires were combined to increase the total current the line can provide.

The down-going cable from the line was attached to the grounding of the pole at its base through the closed spark gap (Fig. 5c), so the line was separated from the ground by the polyamide insulator of the spark gap. Then the gap was very slightly opened (the exact separation distance was difficult to measure) to

Fig. 5. Preparations at the first test location. **(a)** Testing for high voltage. **(b)** Combining the 3 wires (phases). **(c)** Dániel Piri (to the right) and professor Earle Williams are assembling the oscilloscope, inverter, and car battery. The spark gap (to the left) is fixed to the grounding of the pole and the reel of the down-coming cable from the combined line is already attached to its right side.

see whether any spark occurs. No spark could be observed.

The DC voltage between the two ends of the opened spark gap was measured by the digital multimeter. The value wasnt growing and it was not very stable either, it varied in the range of 13–16 V. This value is much smaller than what was expected (∼1300 V) from the height of the line (10 m) given the fair weather potential gradient is 100–200 V/m.

A car battery of 12 V was connected to the line at the corresponding end of the opened spark gap through the Nanoranger ammeter, serving as a voltage source, to check the leakage current (i.e., the insulation resistance) of the line. The device displayed 150 μA and 110 μA in the two wiring (polarity) configurations. Calculating the leakage resistance by Ohms law $R = U/I =$ 12 V $/110 \cdot 10^{-6}$ A $=$ ∼109.1 $k\Omega$ which is a rather low value indicating a poorly insulated system.

To test the AC signal variations on the line, an analog oscilloscope was connected to the two ends of the closed spark gap with a 10-fold voltage attenuator inserted between the oscilloscope and the tested line. The oscilloscope was powered by an inverter supplied by a 12 V car battery. A strongly and not uniformly varying AC signal was seen in the oscilloscope in the 4–5 V range peak-to-peak (pp). This corresponds to the range 40–50 Vpp on the line taking into account the voltage attenuator.

After this, the oscilloscope was disconnected from the spark gap and the spark gap was bridged by the Nanoranger ammeter. The device displayed 130 nA. Note that this result is most probably biased because the AC component of the signal was larger than the DC voltage on the line, so the actual current was likely not monodirectional. In case of bidirectional currents, the values displayed by the Naoranger device cannot be trusted, because the Nanoranger is specifically designed for the measurement of monodirectional small currents. However, being aware of the relatively strong coupled AC signal on the line, results of the leakage test became questionable, too, since the AC voltage variation on the line (40–50 Vpp) was larger than the DC voltage of the battery (12 V).

The above-described experiences are not surprising now that we know that the combined wires were more or less short-circuited to the ground via the top wire at a location further down the line, but that was not known at the time of those measurements. Nevertheless, the 40–50 Vpp signal variations at 10 m height correspond to an electric field variation of 4–5 V/m pp. This is much smaller than the ambient fair weather vertical electric field (100–200 V/m) so this environment would have allowed making valid measurements in normal conditions.

Measurements at the second test point

It was speculated that the magnitude of the AC signal component might be lowered further if the long section of the test line that is running parallel with

the 132 kV transmission line is detached. Segmenting the line is possible at poles where there is a mechanical switch to aid maintenance works. The closest switch was on the pole where the test line turns sharply to the north–east (47.448578° N, 16.693864° E) (Fig. 2). Note that several active power lines run perhaps the closest to the test line at this location.

The measurement took place at the pole with the switch. Ground resistance at this pole was found to be 9 Ω. We were informed that poles with a switch are supposed to have a better grounding. Our measurements confirmed this information (9 Ω vs. 13–19 Ω). The three phases (wires) of the tested line were combined, and the down-going cable was connected to the grounding at the base of the pole through the spark gap. The AC signal measurements were repeated both by the digital multimeter, which showed variations in the 115 Vpp range, and by the oscilloscope, which indicated practically the same range (120 Vpp) and confirmed that the signal waveform includes similar irregularities and mixed frequency content as it was observed at the first testing point.

The 4-fold increased AC amplitude at this location confirms the considerations on the AC coupling in cases when the active line runs perpendicularly to the tested line. This was the configuration here considering the 132 kV high voltage transmission line and the segment of the tested line from this measuring location back to its end in Szakony. The measurements confirmed that the coupled AC signal rings off along the unenergized line further away from the point or region of the strongest coupling. Note that even at its increased level, the coupled AC electric field, 120 Vpp / 10 m = 12 V/m pp is still less than the normal fair weather electric field (100–200 V/m), so usable air–Earth current measurement could have been made on the test line under normal circumstances, at least in theory.

It was around this time when the discontinuity of the lower two wires and the loose grounding of the line (via the top wire and due to the combination of the 3 wires) were discovered.

When the switch was opened and the 2.2 km-long segment of the line back to its end in Szakony was disconnected, the amplitude of the AC component of the signal on the tested line dropped by 75%. Additionally, the waveform of the signal lost its noisy character (Fig. 6) and became apparently sinusoidal at 50 Hz which is the common base frequency of the European continental power line network. This confirmed that a significant fraction of the AC signal component was caused by capacitive coupling from the high voltage transmission line that is running parallel with the tested line in most of its northern part. Detaching that northern segment from the tested line significantly increases the signal to noise ratio in a measurement. On the other hand, it was also realized that the high frequency noise and the irregular, non-sinusoidal character of the signal were caused by the longer segment of the line that included the grounding (Fig. 3b).

The last experiment repeated the leakage current test with the switch opened. This time, the values displayed by the Nanoranger device were 190

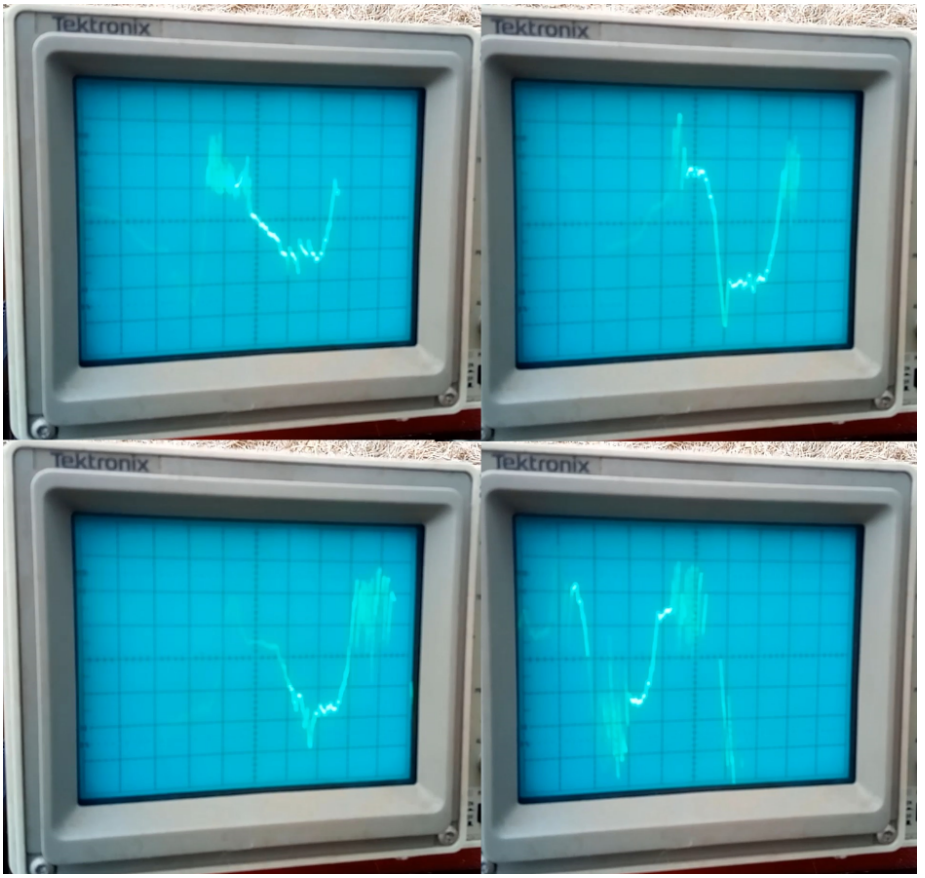

Fig. 6. Screenshots from the oscilloscope when the whole tested line was measured.

μA and 178 μA when it was connected with different polarities and the same 12 V car battery was used as a voltage source. At that point, the testing ended, so these values cannot be evaluated, because the DC voltage was not checked on the 2.2 km-long separated line segment. Note that the insulation resistance of the spark gap wasnt known either. It was observed that the spark gap was practically short-circuited when alcohol was sprayed on the insulator that separates its two ends. This observation emphasizes that the insulation of the spark gap is very much important. It cannot be excluded that dirt and surface moisture caused most of the inferred current leakage during the testing. This would be important especially in the voltage measurement-based research of the DC GEC because leakage currents may significantly bias the measured voltage on the line.

Summary and Conclusions

Supporting our efforts in trying to measure the air–Earth current, E.ON, the energy networks and energy infrastructure company in Hungary kindly made an unenergized power distribution line available for us for testing. The line contained 3 wires for the 3 transmitted power phases, its total length is about 14.5 km and it is located close to the western border of Hungary. Knowing the length and height of the line as well as the approximate diameter of its wires, the potential and the expectable air–Earth current on the line was estimated in section *Estimation of the electric parameters of the measured line*. The benefits of applying an adjustable spark gap in the tests have been discussed, and a method for finding an optimal gap size have been described in section *On using a spark gap in the measurement*. Being aware of the likely AC capacitive coupling of nearby-running active transmission and distribution lines to the tested line, a practical condition for the safe distance from an active line has been worked out in section *Capacitive coupling to the measured line*.

The most important experiences and conclusions of the field test are summarized below.

- Results of the test highlighted the importance of having a good grounding of low resistance at the measuring point. Selection of supporting poles equipped with a maintenance switch at the measuring point is recommended as these poles should have a better grounding.

- Lines of significant current leakage are not suitable for air–Earth current measurements. Checking the leakage resistance of each wire of the tested line separately allows including only the appropriate wires in the measurement. Note that measurement of the current leakage must be made using an appropriate measuring device and voltage source so that the possible capacitive AC coupling from external sources to the tested line is taken into account. Caveats and pitfalls of leakage current measurements are discussed in section *Measurements at the first test point*.

- There were several active, high-voltage power lines in the 20–100 m vicinity of the tested line, so capacitive AC coupling to the tested line could be expected. The AC component is a noise in DC air–Earth current measurements and makes the processing of the recorded data more difficult. Therefore, selection of a line that is away from the known active local power sources is recommended. Lines which are perpendicular to a crossing active power line are favored over lines which are parallel to the nearby active power lines. In case of a perpendicular line, the measurements should be made as far from the cross point with the active line as possible. In addition to keeping a distance from active power lines, low pass filtering the current would provide a solution to cope with unwanted effects of the AC coupling in any measuring environment.

- Although the test line in this report was much exposed to AC capacitive coupling, the performed test did not exclude the possibility that the air–Earth current can be measured on a separated segment of the line. Quantitative survey of the external AC field via the AC signal component on the line and its evaluation of its ratio to the fair weather electric field should be made at each line which is considered for measuring the air–Earth current.

- Having appropriate instrumentation for both checking the line and making measurements on it is of fundamental importance. The spark gap, if applied, should be verified to have a very good insulation to prevent current leakage. The ammeter device intended for measuring the air–Earth current should impose as little load on the line current as possible due to the extremely high internal resistance of the atmospheric current source. If the monodirectionality of the measured current cannot be guaranteed, a non-polarity-specific ammeter should be applied. Additionally, the internal resistance of the ammeter must be at least 2 orders of magnitude less than the total leakage resistance to ground of the line being used.

It has been demonstrated that a rough evaluation of the suitability of an unenergized power line for measuring the air–Earth current can be made with the relatively simple tools applied in this testing. Some of the tools should be improved for the follow-up tests to be more reliable. This includes improving the leakage resistance of the spark gap, and making leakage current measurements with a voltage source of a much higher power. Perhaps the most needed addition would be an universal, polarity-independent solution with which the digital time series of the air–Earth current can be recorded for an in-depth analysis.

Acknowledgements

The Authors express their gratitude to Ferenc Varga, Béla Lágler, József Szántó, and their colleagues for their help in organizing and carrying out the field work. The Authors thank E.ON, the energy networks and energy infrastructure company in Hungary for supporting this work by providing access to the unenergized power line. This work was supported by the National Research, Development, and Innovation Office, Hungary-NKFIH, project number NKFIH-K138824.

References

Bór, J., Bozóki, T., Sátori, G., Williams, E., Behnke, S. A., Rycroft, M. J., et al. (2023). Responses of the AC/DC global electric circuit to volcanic electrical activity in the Hunga Tonga-Hunga Ha'apai eruption on 15 January 2022. *J. Geophys. Res.: Atmos.*, **128**, e2022JD038238. https://doi.org/10.1029/2022JD038238

Burns, G. B., Frank-Kamenetsky, A. V., Tinsley, B. A., French, W. J. R., Grigioni, P., Camporeale, G., & Bering, E. A. (2017). Atmospheric Global Circuit Variations from Vostok and Concordia Electric Field. *J. Atmos. Sci.*, **74**, 783–800. https://doi.org/10.1175/JAS-D-16-0159.1

Goyal, A., Chhabra, L., Sciammarella, J. C., et al. (2023). Defibrillation. [Updated 2023 Jul 24]. In: StatPearls [Internet]. Treasure Island (FL): StatPearls Publishing; 2024 Jan-. Available from: https://www.ncbi.nlm.nih.gov/books/NBK499899/.

Haldoupis, C., Rycroft, M., Williams, E., & Price, C. (2017). Is the Earth-ionosphere capacitor a valid component in the atmospheric global electric circuit? *J. Atmos. Sol. Terr. Phys.*, **164**, 127–131. https://doi.org/10.1016/j.jastp.2017.08.012

Hardy, J. T. (2003). *Climate Change: Causes, Effects, and Solutions*. John Wiley & Sons Inc., Hoboken, NJ 07030, USA. ISBN: 978-0-470-85019-0, 272 pages.

Harrison, R. G., Nicoll, K. A., Mareev, E., Slyunyaev, N., & Rycroft, M. J. (2020). Extensive layer clouds in the global electric circuit: their effects on vertical charge distribution and storage. *Proc. R. Soc. A*, **476**, 20190758. http://dx.doi.org/10.1098/rspa.2019.0758

Liu, C., & Zipser, E.J. (2009). Warm Rain in the Tropics: Seasonal and Regional Distributions Based on 9 yr of TRMM Data. *J. Clim.*, **22**, 767–779. https://doi.org/10.1175/2008JCLI2641.1

Liu, C., Williams, E.R., Zipser, E.J., & Burns, G. (2010). Diurnal variation of global thunderstorms and electrified shower clouds and their contribution to the global electrical circuit. *J. Atmos. Sci.*, **67**, 309–323. https://doi.org/10.1175/2009JAS3248.1

Luo, X., Yin, M., Xu, C., & Tang, G. (2023). Simulation Study on Safe Distance between Crane Boom and High-Voltage Line Based on Electric Field Intensity. *J. Phys. Conf. Ser.*, **2493**, 012020. https://doi.org/10.1088/1742-6596/2493/1/012020

Mach, D.M., Blakeslee, R.J., Bateman, M.G., & Bailey, J.C. (2009). Electric fields, conductivity, and estimated currents from aircraft overflights of electrified clouds. *J. Geophys. Res.: Atmos.*, **114**, D10204. https://doi.org/10.1029/2008JD011495

Mach, D.M., Blakeslee, R.J., Bateman, M.G., & Bailey, J.C. (2010). Comparisons of total currents based on storm location, polarity, and flash rates derived from high-altitude aircraft overflights. *J. Geophys. Res.: Atmos.*, **115**, D03201. https://doi.org/10.1029/2009JD012240

Mach, D.M., Blakeslee, R.J., & Bateman, M.G. (2011). Global electric circuit implications of combined aircraft storm electric current measurements and satellite-based diurnal lightning statistics. *J. Geophys. Res.: Atmos.*, **116**, D05201. https://doi.org/10.1029/2010JD014462

Nicoll, K.A. (2012). Measurements of atmospheric electricity aloft. *Surv. Geophys.*, **33**(5), 991–1057. https://doi.org/10.1007/s10712-012-9188-9

Price, C., Pechony, O., & Greenberg, E. (2007). Schumann resonances in lightning research. *Lightning Research*, **1**, 1–15.

Reitz, J.R., Milford, F.J., & Christy, R.W. (2008). *Foundations of Electromagnetic Theory*. 4th Edition. Addison-Wesley, Reading, MA. ISBN-10: 0321581741, ISBN-13: 978-0321581747, 630 pages.

Ruhnke, L.H. (1969). Area averaging of atmospheric electric currents. *J. Geomagn. Geoelec.*, **21**, 453–462. https://doi.org/10.5636/jgg.21.453

Ruhnke, L.H., Tammet, H.F., & Arold, M. (1983). Atmospheric electric currents at widely spaced stations. In: Ruhnke, L.H., & Latham, J. (Eds.), *Proceedings in Atmospheric Electricity*, A. Deepak Publishing, pp. 76–78.

Rycroft, M.J., Harrison, R.G., Nicoll, K.A., & Mareev, E.A. (2008). An Overview of Earths Global Electric Circuit and Atmospheric Conductivity. In: Leblanc, F., Aplin, K.L., Yair, Y., Harrison, R.G., Lebreton, J.P., & Blanc, M. (Eds.), *Planetary Atmospheric Electricity*, Space Sciences Series of ISSI, **30**, 83–104. Springer, New York, NY. https://doi.org/10.1007/978-0-387-87664-1_6

Salzmann, M. (2016). Global warming without global mean precipitation increase? *Sci. Adv.*, **2**, e1501572. https://doi.org/10.1126/sciadv.1501572

Sankar, P.B. (2011). *Measurement of air breakdown voltage and electric field using standard sphere gap method*. Masters Thesis, Department of Electrical Engineering, National Institute of Technology, Rourkela, India. https://core.ac.uk/reader/53188100.

Tammet, H., Israelsson, S., Knudsen, E., & Tuomi, T.J. (1996). Effective area of a horizontal long-wire antenna collecting the atmospheric electric vertical current. *J. Geophys. Res.*, **101**(D23), 29671–29677. https://doi.org/10.1029/96JD02131

Williams, E.R. (1992). The Schumann Resonance: A global tropical thermometer. *Science*, **256**, 1184–1187. https://doi.org/10.1126/science.256.5060.1184

Wilson, C.T.R. (1920). Investigations on lightning discharges and on the electric field of thunderstorms. *Phil. Trans. R. Soc. A*, **221**, 73–115. https://doi.org/10.1098/rsta.1921.0003

Magnetotelluric Field Campaign in the Nógrád–Gömör Volcanic Field (Northern Pannonian Basin)

Tibor Rubóczki[1,2*], Ákos Kővágó[1,2], Csaba Molnár[1], Ján Vozár[3] and Levente Patkó[1]

[1]HUN-REN Institute of Earth Physics and Space Science, Sopron, Hungary
[2]Doctoral School of Earth Sciences, Eötvös Loránd University, Budapest, Hungary
[3]Earth Science Institute, Slovak Academy of Sciences, Bratislava, Slovakia

Abstract

In planning a magnetotelluric survey, there are several requirements to consider in order to record high-quality electromagnetic time series for geological investigation. In this paper, we present an example of a magnetotelluric field survey recently conducted in the Nógrád–Gömör Volcanic Field (Northern Pannonian Basin) during the summer of 2024, focusing on the recommended conditions for magnetotelluric station deployment. We begin with the geological goals and the motivation behind the magnetotelluric survey, followed by a suitable site selection, and conclude with some direct electromagnetic field observations from the time series obtained. Finally, we summarize the preliminary results of the magnetotelluric field campaign and suggest potential improvements that could enhance the quality of future field measurements.

Keywords: magnetotellurics, electromagnetic deep structure investigation, field campaign planning.

Introduction

The Institute of Earth Physics and Space Science in Sopron has been conducting field magnetotelluric (MT) measurements in the Carpathian–Pannonian region for more than 60 years, for both near-surface and deep structural investigations (e.g., Ádám and Wesztergom, 2001; Ádám et al., 2017). The current MT instrumentation allows for high-precision electromagnetic (EM) field recording, with an accuracy of <0.1 nT for the magnetic field and <0.1 mV/km for the electric field during long-period MT recordings. The magnetometer and electrodes used during the measurement are capable of detecting changes in the magnetic

*Corresponding author: Tibor Rubóczki (ruboczki.tibor@epss.hun-ren.hu)
Citation: T. Rubóczki, Á. Kővágó, Cs. Molnár, J. Vozár and L. Patkó (2025): Magnetotelluric field campaign in the Nógrád–Gömör Volcanic Field (Northern Pannonian Basin). *Geophysical Observatory Reports, 2023–2024*, 69–81. https://doi.org/10.55855/gor2024.5

field generated by the electric current systems of the ionosphere and the magnetosphere, as well as changes in the electric and magnetic fields originating from the subsurface medium, created simultaneously through electromagnetic induction.

During the deployment of MT measurements, it is important to ensure that the station site aligns with the necessary MT field conditions. The most critical requirements are to position the MT station on a flat ground surface and at a sufficient distance from anthropogenic noise sources, such as the electrical infrastructure. The main challenge is typically finding sufficient spatial distance from electrical infrastructure, such as high voltage power transmission lines, railway lines, solar panel farms, and even smaller devices with lower performance like electric pumps, pylons, electric fences etc. These sources, even several hundred meters to a few kilometers away (depending on conductivity of shallow structures), can cause significant EM noise, detectable in the measurements due to the high sensitivity of MT sensors. In many cases, anthropogenic EM noise cannot be effectively completely removed from the time series, which can compromise MT time series processing, leading to inaccurate MT response functions. Therefore, it is crucial to establish MT measurement sites where EM noise is minimized. A good example of selecting near-optimal MT measurement sites can be seen in the long-period MT measurements conducted in the Transylvanian Basin (Novák et al., 2024).

Note that in mountainous and hilly regions, such as the Transdanubian Range, soil may barely cover the hard bedrock at the surface. Therefore, it is not recommended to establish MT sites in such locations, as the MT sensors should be placed approximately 0.5 m below the surface to avoid temperature fluctuations, wind effects and other environmental factors during measurement (Rubóczki et al., 2024). Given the challenges posed by these criteria, this paper presents the main steps of a recent MT field measurement campaign carried out in 2024 in the Nógrád–Gömör Volcanic Field.

The Geological Objective

The Neogene magmatic evolution of the monogenetic Nógrád–Gömör Volcanic Field (NGVF), and its impact on both the surface and the entire lithosphere, has long been a subject of research. The volcanism (e.g., Konečný et al., 1995) and the melt-wall rock interactions within the crust (e.g., Kovács and Szabó, 2005) and lithospheric mantle (e.g., Szabó and Taylor, 1994) has been investigated in details. The occurrence of carbon dioxide–rich springs in this area suggests that fluids are still actively migrating from the rootzones of the volcanic field to the surface. It is also important to note that the Hurbanovo–Diósjen Line, a boundary between the northern Alpine and Central Western Carpathians units on its northern side and the southern Alpine (Transdanubian) and Dinaridic (Bükk) units on its southern side (Kováč et al., 2016), possibly plays a key role

in the volcanism, as it is likely crosses this area and is associated with active seismicity (Wéber, 2016).

To gather more geological information on the deep lithosphere of the NGVF, colleagues from the Earth Physics and Space Science Research Institute conducted a series of MT measurements in 2013–2014. During this fieldwork, 14 stations were established along a northwest–southeast trending section (Fig. 1a), with station spacing of 3–5 km and a total section length of approximately ∼60 km. The electrical resistivity distribution from these MT measurements reflects subsurface geological structures, including the presence of well-conductive body (<1 Ωm) underneath the Moho in the central NGVF (Fig. 1b). This corresponds to the same area where upper mantle xenoliths with wehrlitic modal composition were collected from six quarries (Patkó et al., 2020). The estimated electrical resistivity of the wehrlites (∼132 Ωm) alone could not account for the observed low resistivity values, leading to further modelling to assess the potential role of melt. The models revealed that even ∼2–3 vol.% of interconnected melt could reduce the electrical resistivity to below 1 Ωm in the wehrlites (Patkó et al., 2021). The goal of the new MT measurements in 2024 was to extend the previous 2D MT section into a 3D model, allowing for a more detailed spatial delineation of the electrically well-conducting domain identified in earlier inversion models.

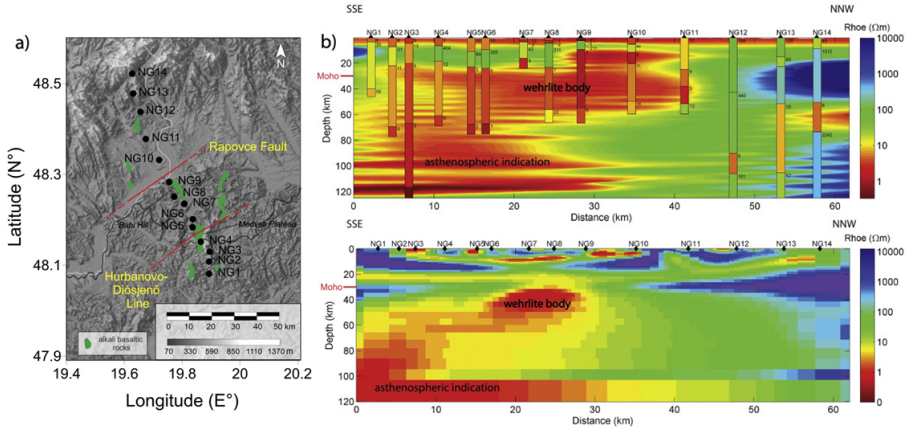

Fig. 1. a) Map of the Nógrád–Gömör MT section, showing measurement locations (black dots), major fault zones (red lines), and surface alkali basaltic outcrops (green fields), **b)** 1D inversion (top), 2D inversion (bottom) of the NG MT section (from Patkó et al. (2021)).

Planning of the MT Sites in the Nógrád–Gömör Volcanic Field in 2024

The location of the planned new MT stations (NGn) was determined based on the subsurface resistivity anomalies identified along the previously measured NG section. Fortunately, the geophysicist colleagues of the Slovak Academy of Sciences informed us, they have MT data from the NGVF region, the so-called 2T section (Vozár et al., 2021). This section traverses Slovakia in a northwest–southeast direction, running parallel to the NG MT section, approximately ∼15 km east of it, and has a comparable MT station spacing to the NG section. The key difference between the MT datasets of the NG and 2T sections is that the NG MT section consists of long-period MT measurements (max. ∼10000 s), whereas the 2T section contains short-period MT data (max. ∼100–500 s). Since our primary objective is to achieve maximum penetration depth in the lithosphere, follow the path of the 2T section. This approach ensures that, after completing the NGn MT measurements, both the NG and 2T MT sections will have long-period MT data, significantly enhancing the depth of investigation. Moreover, the existing 2T MT section data will support the time series processing of the new NGn MT sites. Once the datasets from the NG and 2T sections are combined, they will be suitable for conducting a regional-scale 3D MT inversion, providing a comprehensive view of the lithospheric structures beneath the NGVF.

The planning of the new MT sites required careful consideration of the terrain and the proximity of electrical infrastructure. In the study area, there are primarily small villages located a few kilometres apart with nearby towns such as Lučenec (Losonc) and Fiľakovo (Fülek) more than 10 km away from the closest MT sites (Fig. 2). Most of the suitable land between these villages was under cultivation, making it unsuitable for MT station placement. Additionally, the research area included high-voltage power lines, several stone quarries, and railway lines, all of which needed to be avoided as much as possible. Fortunately, the railway was not electrified, allowing us to place stations nearby without significant concern. Another crucial factor was the planned long-period nature of the MT measurements, which required an operating time of 9 to 14 days. Therefore, it was essential to locate the MT stations in sufficiently safe areas, preferably out of sight. In the unlikely event that someone did discover the MT site, we provided a bilingual Slovakian–Hungarian warning notice on the box, along with the contact details for our colleagues.

The exact site locations were selected using the Google Earth satellite images, taking into account both the geological targets and the field conditions. While other geo-information systems can be utilized, it is crucial to ensure that the maps indicate industrial buildings and agricultural areas that should be avoided. Regularly updated satellite images provide the easiest solution for this purpose. It is highly recommended to conduct a field trip before starting the MT campaign, as field conditions may differ from what is shown on the

maps. This trip also helps assess the accessibility of potential sites. After assigning the MT stations, we undertook a field visit to verify the site conditions. Some planned MT locations appeared accessible on the map, but we found that there was no passable road leading to them. In other instances, we encountered heavier vegetation than anticipated, prompting us to search for alternative site locations.

We would like to note that during the magnetotelluric (MT) measurements, two pairs of electrodes with a length of 50 meters each, measuring two horizontal electric components, are preferably oriented in the north–south and north–west directions to capture the dominant regional geological structures. Therefore, when selecting a site, it is essential to ensure a clear area of 50×50 meters for the installation. Although, in theory, the distance between the electrodes and their orientation can be varied — since these field changes can be accounted for during the MT time series processing — it is usually best to use the default MT instrument setup mentioned above. Once the planned MT locations were selected and the field check was successful, we were ready to launch the field MT campaign.

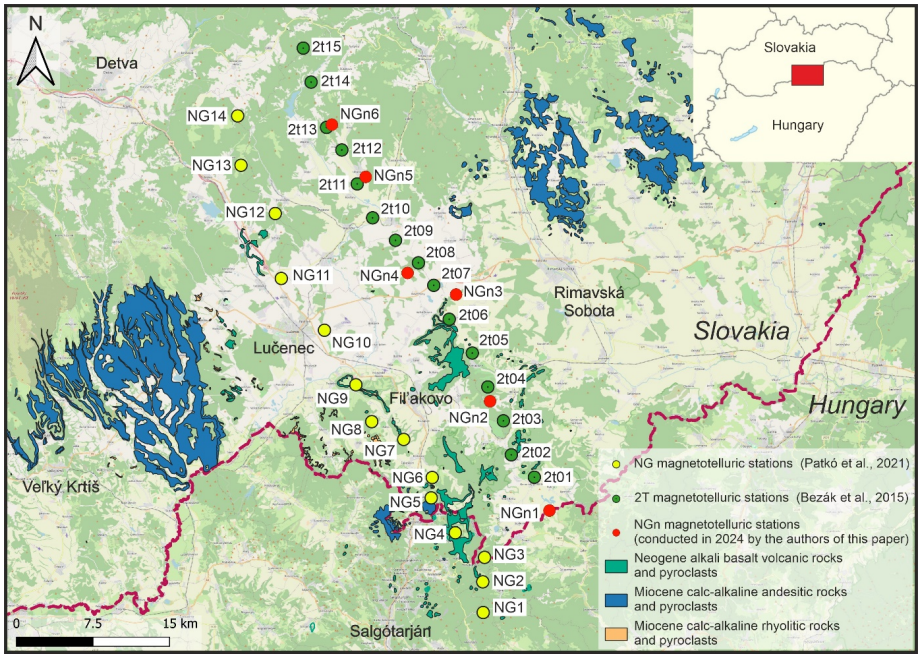

Fig. 2. Simplified map showing MT measurements in the Nógrád–Gömör Volcanic Field and its surroundings, with the distribution of various volcanic products based on the map of Káčer et al. (2005) and Gyalog and Síkhegyi (2005).

MT Field Measurements Experiences

The new NGn MT survey involved 6 long-period MT measurements, as shown in Fig. 2, carried out between July and September 2024. Planning the logistics of the deployment was a challenge, as the round trip between Sopron and NGVF took around 9 hours, and cost efficiency is typically a key factor in any MT campaign. Additionally, concealing the instruments was crucial, particularly given the extended duration of the field measurements, which increased the likelihood of the devices being found, as well as the possibility of errors during data collection, such as animals damaging or chewing on the cables. In the worst-case scenario, this could result in sensor loss. In terms of the location selection, most of the MT stations were situated at least 1 km away from any known electrical infrastructure, to minimize electromagnetic noise. However, the terrain in certain parts of the NGVF was quite hilly, which made it difficult to always find completely flat areas for the installation. Figure 3 provides an example of the local terrain characteristics encountered during the survey.

Some Characteristics of the Nógrád–Gömör MT Time Series

The MT field measurements capture both the horizontal and vertical components of the magnetic induction vector (B_x, B_y, B_z) along with the horizontal electric field components (E_x, E_y). The measurements were performed using a LEMI417 long-period MT instrument, the sampling frequency was 4 Hz in all stations. Figures 4, 5, 6 and 7 illustrate some of the most common patterns in the time series from these field measurements. The time series of the EM field components are sorted. The x component of the magnetic field vector (B_x) aligns with the N–S direction. According to Faraday's law, changes in the magnetic field along this direction induce a corresponding electric (telluric) current in the E–W direction. This is why the second row of the time series (E_y) corresponds to this induced current in the E–W direction. Similarly, the third row (B_y) reflects the E–W component of the magnetic field vector, while its corresponding electric field component (E_x), which lies along the N–S direction, is shown in the fourth row. The near-zero values of B_y ($\approx$0 nT) can be attributed to the orientation of the magnetometer relative to the magnetic E–W direction, which reduces signal amplitude in this component. The 5^{th} row in the time series displays the vertical component of the magnetic field (B_z).

Figure 4 shows the time series of the EM field recorded by the NGn3 MT station on 5 August 2024. By the time the measurements began on 1^{st} of August, the surrounding fields had already been harvested, leading to the assumption that no significant anthropogenic noise from the harvesting would affect the data. However, some moderate electrical noise and occasional overshooting peaks were still observed in the time series of the electrical channels E_x and E_y. This disturbance is likely attributed to activity from a nearby stone mine

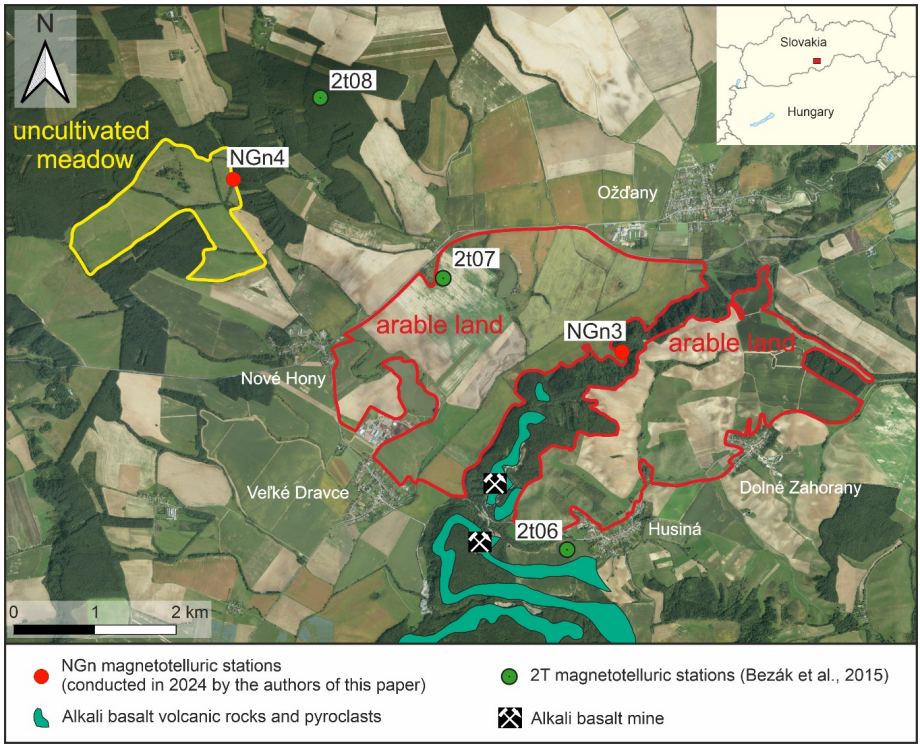

Fig. 3. The area around the NGn3 and NGn4 MT sites (see Fig. 2 to identify these neighbourhoods), where red circles indicate locations unsuitable for deployment, while the areas within the yellow frame are considered suitable for MT installation. The distribution of the alkali basalt volcanics and pyroclasts are based on the map of Káčer et al. (2005).

(∼1 km), particularly since the time series was recorded on a Monday, a typical workday. It is a common observation in the MT fieldwork that anthropogenic noise caused by human activities tends to be present in the electric channels between ∼6 a.m. and ∼6 p.m. on weekdays. While the exact source of the electrical noise is often difficult to identify, the magnetic field components usually exhibit no such noise or at least a much-attenuated version of it. This pattern is evident in the NGn3 time series from 5 August, where the electric channels show noticeable noise between 8 a.m. and 8 p.m., while the magnetic channels remain largely unaffected. Overall, this particular measurement from NGn3 displays a relatively low level of noise compared to other cases, where higher levels of noise were often detected.

The NGn4 MT station was situated in a meadow area, away from cultivated land, leading us to anticipate a lower level of noise intensity during the measurements. However, some of the recorded time series exhibited variations, as

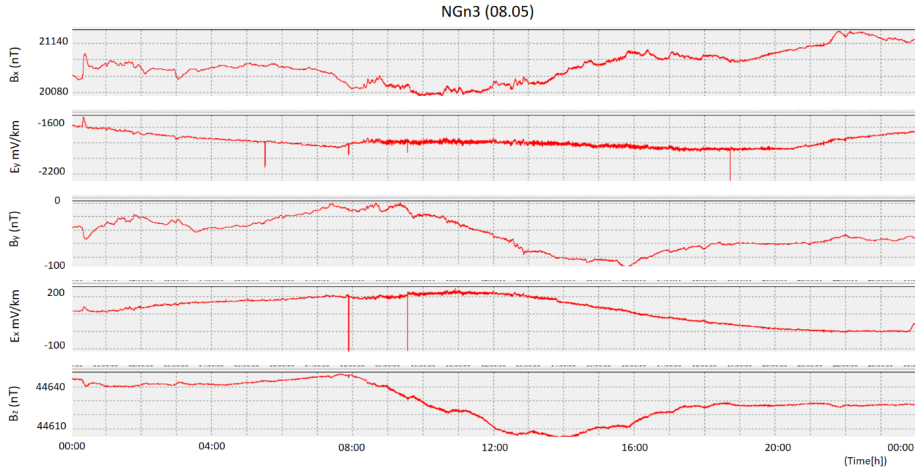

Fig. 4. Time series of NGn3 MT station B_x, B_y, B_z, E_x, E_y, on Monday, 5 August 2024.

illustrated in Fig. 6. Initially, we suspected that a nearby high-power electrical device might be the source of this noise, as such devices can produce both direct electrical noise and magnetic induction components. To investigate further, we compared the time series from the NGn4 MT station with those from the NGn3 MT station, which was operating simultaneously and located about 5 km away (Fig. 3). Notably, both stations recorded very similar field variations throughout most of the day on 11 August. Given the proximity of the two stations, it seemed unlikely that a single anthropogenic electromagnetic source could be responsible for the rapid field changes observed at both locations. As supporting evidence, we also examined the magnetic field components recorded by the nearest magnetic observatory in Slovakia (Fig. 7). The variations in the field at the observatory closely mirrored the signal shapes observed in the time series from both NGn3 and NGn4. This correlation indicates that the rapid changes in magnetic field recorded by the MT measurements on 11 August were likely caused by increased activity from natural electromagnetic sources, rather than by anthropogenic interference.

In the NGn3 MT time series shown in Fig. 5, we observed that the electrical channel in the E–W direction (second row) exhibited signs of malfunction, entering saturation several times. Upon investigation, we discovered that the cable at the site had likely been completely torn, possibly by an animal. This type of issue was not uncommon; the fields that seem ideal for MT stations also attract wildlife. Unfortunately, wild animals tend to roam these areas, and it is not unusual for them to chew or break the cables as they move through the site. During the 2024 MT measurements in the NGVF, we frequently encountered cable damage caused by animals. Given that such damage was a recurring chal-

lenge, especially during long-period MT measurements, it has become evident that a permanent solution is needed to mitigate these failures in the future.

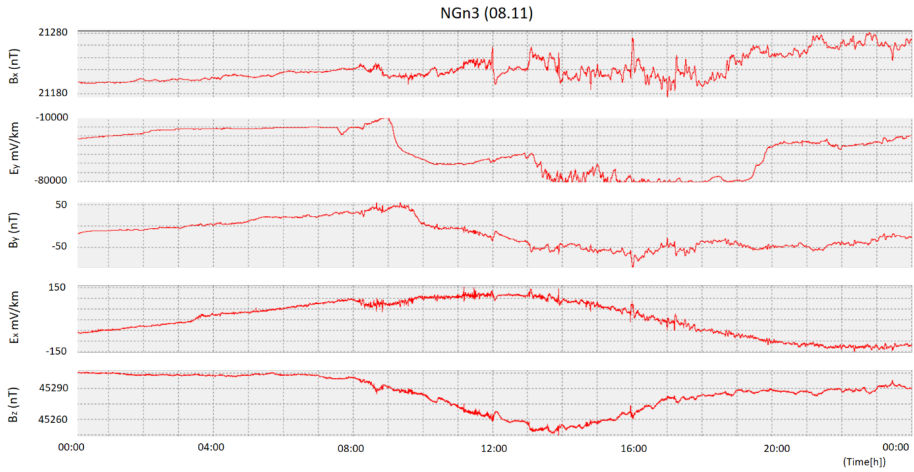

Fig. 5. Time series of NGn3 MT station B_x, B_y, B_z, E_x, E_y, on Sunday, 11 August 2024.

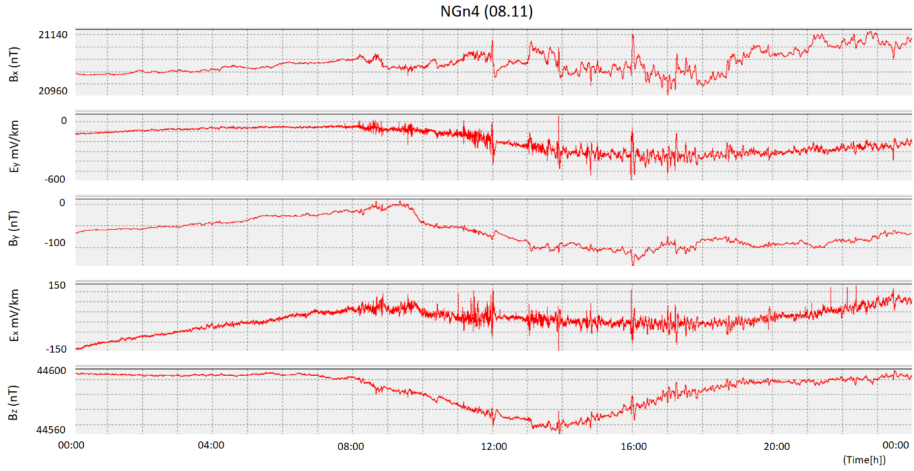

Fig. 6. Time series of NGn4 MT station B_x, B_y, B_z, E_x, E_y, on Sunday, 11 August 2024.

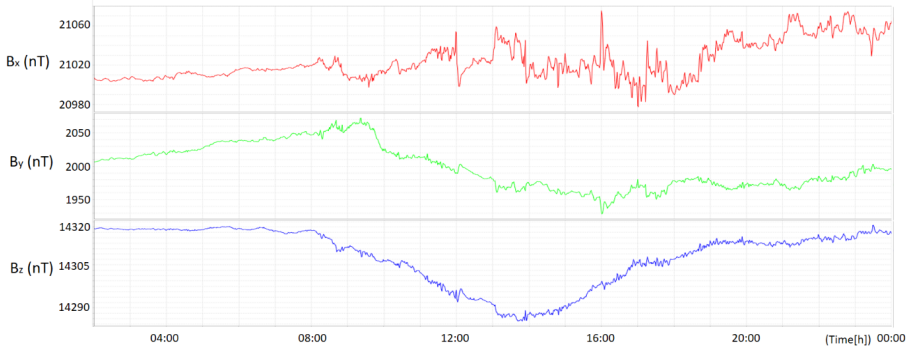

Fig. 7. Time series of Hurbanovo Magnetic Observatory B_x, B_y, B_z fields on Sunday 11 August 2024.

Evaluation of the 2024 MT Fieldwork in the Nógrád–Gömör Volcanic Field

During the new MT survey in the NGVF, we successfully identified new MT site locations that met both the geological and technical requirements for MT deployment. More detailed information on the quality of the 2024 MT measurements will be available after the time series processing. However, it appears that the quality of the recorded time series is comparable to the previous 2013–14 NG MT section measurements. A significant difference is the duration of the 2024 MT measurements, which was 3 to 4 times longer than the prior measurements. The extended recording period offers several advantages: in cases of noisy time series, longer continuous data segments may contain more periods with less noise, such as weekends. Additionally, longer recordings allow for the calculation of impedances with smaller errors over longer periods. The logistics for the long-period MT sites were appropriate, especially given that short-period data had already been collected along the 2T MT section (Bezák et al., 2015). However, we would like to point out that if additional short-period MT measurements had been necessary, it would not have been possible to complete them in a single day. In that case, we would have needed to plan the MT campaign with a different time and cost schedule.

In addition, when selecting the MT stations, it is important to consider both local and seasonal conditions. For example, during the NGn measurements, none of the areas suitable for us had been recently mown. It is crucial to avoid installing an MT station just before mowing, as this could result in equipment damage. Fortunately, during the MT deployment, we were lucky: the 6 new MT measurements were conducted between 9 July and 3 September 2024, and all the selected areas had already been mown before the measurements began. Since there was no significant precipitation during this period, the vegetation grew minimally, and there was no risk of additional mowing.

During the installation of the MT stations, the data logger box was hidden in bushes, which proved to be an effective practice, as the station was not visible even from a few dozen meters away. However, the cables for the electrical channels were frequently disturbed by animals. In the future, the cables should be secured to the ground in some way, as wild boar, deer, roe deer and rabbits tend to chew them. Additionally, it would be helpful to be notified immediately if there is a malfunction at the MT station, rather than only discovering it when collecting the equipment. A good solution would be remote access to the MT station, which is something we are planning to implement in the near future.

Conclusions

In the summer of 2024, between July and September, we successfully carried out MT measurements in the NGVF, establishing 6 new long-period MT stations along a previously measured 2T MT section, which had only short-period (max 100–500 s) data. The aim of the new MT measurements is to extend the dataset to longer-periods (up to 10000 s), allowing for deeper penetration to provide more accurate data at depths of at least 50–100 km. In this short communication, we have reviewed the necessary conditions for planning of the MT measurements, balancing both the geological objectives and the technical suitability of the locations. We have also suggested potential solutions to address challenges such as anthropogenic noise and cable damage caused by animals, both of which can reduce the efficiency of MT measurements. Additionally, we have illustrated the impact of these disturbances on the recorded EM field time series. An interesting observation from the MT measurements was a geomagnetic active period, detected not only in the time series of two parallel operated MT stations but also confirmed by a nearby magnetic observatory.

Acknowledgements

This research was financially supported by the National Research, Development and Innovation Fund (grant number: 145853) to LP. The international collaboration was supported by the KMP-2024/21 HUN-REN mobility project. This work was supported by VEGA project No. 2/0171/24.

References

Ádám, A. and Wesztergom, V. (2001). An attempt to map the depth of the electrical asthenosphere by deep magnetotelluric measurements in the Pannonian Basin (Hungary). *Acta Geologica Hungarica*, 44(2–3):167–192.

Ádám, A., Szarka, L., Novák, A., and Wesztergom, V. (2017). Key results on deep electrical conductivity anomalies in the Pannonian Basin (PB), and their geodynamic aspects. *Acta Geodaetica et Geophysica*, 52:205–228. https://doi.org/10.1007/s40328-016-0192-2.

Bezák, V., Josef, P., Majcin, D., Bučová, J., Šoltis, T., Bilčík, D., and Klanica, R. (2015). Geological interpretation of magnetotelluric sounding in the southern part of seismic profile 2T (Central Slovakia). *Contributions to Geophysics and Geodesy*, 45(1):1–11.

Gyalog, L. and Síkhegyi, F. (2005). Magyarország földtani térképe, M= 1:100 000.[The Geological Map of Hungary, 1: 100 000in Hungarian]. *Magyar Állami Földtani Intézet kiadványa*, Budapest.

Káčer, Š., Antalík, M., Lexa, J., Zvara, I., Fritzman, R., Vlachovič, J., Bystrická, G., Brodianska, M., Podfaj, M., Madarás, J., Nagy, A., Maglay, J., Ivanička, J., Gross, P., Rakús, M., Vozárová, A., Buček, S., Boorová, D., Šimon, L., Mello, J., Polák, M., Bezák, V., Hók, J., Teťák, F., Konečný, V., Kučera, M., Žec, B., Elečko, M., Hraško, Ľ., Kováčik, M., and Pristaš, J. (2005). Digitálna geologická mapa Slovenskej republiky v M 1:50 000 a 1:500 000. *MŽP SR, ŠGÚDŠ*.

Konečný, V., Lexa, J., Balogh, K., and Konečný, P. (1995). Alkali basalt volcanism in Southern Slovakia: volcanic forms and time evolution. *Acta Vulcanologica*, 7:167–172.

Kováč, M., Plašienka, D., Soták, J., Vojtko, R., Oszczypko, N., Less, G., osović, V., Fügenschuh, B., and Králiková, S. (2016). Paleogene palaeogeography and basin evolution of the Western Carpathians, Northern Pannonian domain and adjoining areas. *Global and Planetary Change*, 140:9–27. https://doi.org/10.1016/j.gloplacha.2016.03.007.

Kovács, I. J. and Szabó, C. (2005). Petrology and geochemistry of granulite xenoliths beneath the Nógrád-Gömör volcanic field, Carpathian–Pannonian region (N-Hungary/S-Slovakia). *Mineralogy and Petrology*, 85:269–290. https://doi.org/10.1007/s00710-005-0090-8.

Novák, A., Rubóczki, T., Wesztergom, V., Mircea, R., Szakács, A., Molnár, C., and Kovács, I. J. (2024). Lithospheric scale cross-section through the Transylvanian Basin: A joint geophysical and geological survey. *Geologica Carpathica*, pages 195–211. https://doi.org/10.31577/GeolCarp.2024.11.

Patkó, L., Liptai, N., Aradi, L. E., Klébesz, R., Sendula, E., Bodnar, R. J., Kovács, I. J., Hidas, K., Cesare, B., Novák, A., Trásy, B., and Szabó, C. (2020). Metasomatism–induced wehrlite formation in the upper mantle beneath the Nógrád-Gömör Volcanic Field (Northern Pannonian Basin): evidence from xenoliths. *Geoscience Frontiers*, 11(3):943–964. https://doi.org/10.1016/j.gsf.2019.09.012.

Patkó, L., Novák, A., Klébesz, R., Liptai, N., Lange, T. P., Molnár, G., Csontos, L., Wesztergom, V., Kovács, I. J., and Szabó, C. (2021). Effect of metasomatism on the electrical resistivity of the lithospheric mantle An integrated research using magnetotelluric sounding and xenoliths beneath the

Nógrád–Gömör Volcanic Field. *Global and Planetary Change*, 197:103389. https://doi.org/10.1016/j.gloplacha.2020.103389.

Rubóczki, T., Novák, A., Liptai, N., Porkoláb, K., Molnár, C., Galsa, A., Molnár, G., Wesztergom, V., and Kovács, I. J. (2024). The Pannon LitH2Oscope magnetotelluric array in the Pannonian Basin. *Acta Geodaetica et Geophysica*, page 26.

Szabó, C. and Taylor, L. A. (1994). Mantle petrology and geochemistry beneath the Nógrád–Gömör volcanic field, Carpathian–Pannonian region. *International Geology Review*, 36(4):328–358. https://doi.org/10.1080/00206819409465465.

Vozár, J., Bezák, V., and Marko, F. (2021). Three-dimensional magnetotelluric model along seismic profile 2T: An improved view on crustal structure in central Slovakia (Western Carpathians). *Geologica Carpathica*, 72(2). https://doi.org/10.31577/GeolCarp.72.2.1.

Wéber, Z. (2016). Source parameters for the 2013..2015 earthquake sequence in Nógrád county, Hungary. *Journal of Seismology*, 20:987–999. https://doi.org/10.1007/s10950-016-9576-6.

A Geodynamic Network for the Monitoring of Seismo–Tectonic Activity Along the Mur–Mürz Fault Line (Austria)

Enikő Barbély[1,2*], Judit Benedek[1], Roman Leonhardt[3], Nikolaus Horn[3], Csongor Szabó[1], Tibor Molnár[1], Dániel István Csáki[4], Bruno Meurers[5] and Gábor Papp[1]

[1]HUN-REN Institute of Earth Physics and Space Science, Sopron, Hungary
[2]Department of Geodesy and Surveying, Faculty of Civil Engineering, University of Technology and Economics, Budapest, Hungary
[3]GeoSphere Austria, Vienna, Austria
[4]HUN-REN Institute of Earth Physics and Space Science, Sopron, Hungary
(2021–2022)
[5]University of Vienna, Vienna, Austria

Abstract

The Mur-Mürz fault line is an active boundary between the geological units of the Eastern Alps and the Pannonian basin. Some moderate earthquakes shake this densely inhabited border area between Austria and Hungary every year, consequently special attention is paid for the research of its seismo-tectonic activity. Beyond the seismological monitoring the continuous observation of long periodic crustal deformations may efficiently help the understanding and interpretation of the mechanism of tectonic processes connected to the seismological events. Therefore, in the national networks of seismometers operated in and around the area (Vienna basin), three seismic stations were completed by high resolution tilt meters and two more independent tilt stations were installed on a 51 km by 25 km area in east-west and north-south directions, respectively, on both sides of the fault until 2023. This report shortly introduces the observations sites, their instrumentation and technical infrastructure as well as the processing methodology of the time series of recorded ground tilts. It also refers to the achieved results briefly.

Keywords: high resolution tiltmeter, Mur-Mürz fault line, monitoring network, data corrections.

*Corresponding author: Enikő Barbély (barbely.eniko@epss.hun-ren.hu)
Citation: E. Barbély, J. Benedek, R. Leonhardt, N. Horn, Cs. Szabó, T. Molnár, D. I. Csáki, B. Meurers and G. Papp (2025): A Geodynamic Network for the Monitoring of Seismo–Tectonic Activity Along the Mur–Mürz Fault Line (Austria). *Geophysical Observatory Reports, 2023–2024*, 82–105. https://doi.org/10.55855/gor2024.6

Introduction

Due to the recent tectonics of the Mur-Mürz fault line separating the Eastern Alps and the Pannonian basin near to the state border between Austria and Hungary some earthquakes of small and moderate magnitude may occur from year to year. There were 9 such events ($2.5 \leq M \leq 5$) along the fault between January, 2023 and April, 2024. Since the area which includes the Vienna basin is densely inhabited the monitoring of the seismo-tectonic activities using different kinds of devices and technologies is a justified public need. Although the national seismological networks of Austria, Slovakia and Hungary watch and record continuously the 3D ground speeds at their nearby stations the instrumentation of some were gradually completed by high resolution tiltmeters. This improvement was financed by the Eötvös Loránd Research Network, Hungary in the framework of an application call for infrastructure development (ELKH IF-1/2021)[†]. So nowadays at 3 sites co-located seismometers and tilt meters are operated by GeoSphere Austria and HUN-REN Institute of Earth Physics and Space Science (EPSS) in cooperation. The other two sites run only tiltmeters, but all the sites are installed in underground facilities (abandoned mine vaults, tunnels, cellars) providing high temperature stability (typically below 0.01° C/day) required for the undisturbed observations. The search for the location of one more suitable station is currently under discussion. The sites are situated nearly along a line between the Conrad Observatory (COBS), Austria and the Sopronbánfalva Geodynamical Observatory, Hungary (SOPGO) crossing the fault in south-east and north-west direction. Both observatories have been equipped also by recording gravity meters (COBS: GWR Superconducting Gravimeter, SOPGO LCR G949 spring type gravimeter) applied to measure and record the time variation of the gravity field. SOPGO is equipped also by a 20 m long extensometer. The distance between COBS and SOPGO is about 60 km. The network and its surrounding can be seen in Fig. 1.

Network Stations and Their Instrumentation

Stations

All the stations and the instrumentation installed and operated there are listed in Table I. The depth of the observation sites measured from the ground surface varies between 5 m (SOPPAL) and 30 m (COBS).

- Conrad Obsevatory (COBS), Geosphere, Austria The Conrad Observatory is located 60 km SW of Vienna (Austria) in a carbonate region belonging to the Eastern Alps, close to the top of the Trafelberg Mountain at an elevation of 1050 m. The Trafelberg Mountain itself is part of the Northern Calcareous Alps consisting of Main Dolomite and Wetterstein/Gutenstein

[†]The project budget was 14 million HUF (∼35.000 EUR).

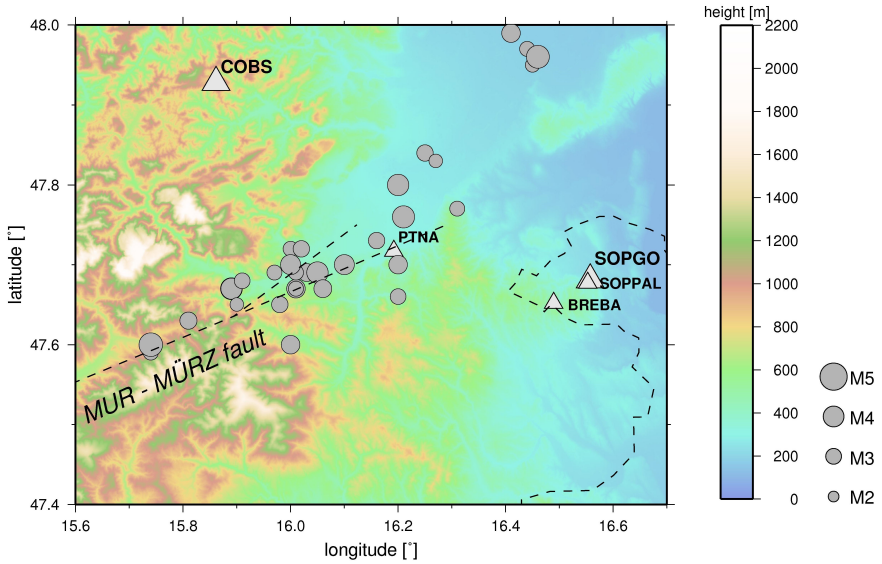

Fig. 1. The locations of the observation sites (triangles) and the epicentres of earthquakes (circles) occurred recently (30.01.2008 01.02.2024) on the research area. The color coded background picture shows the SRTM3 topography of the area (Jarvis et al., 2008). The dashed line shows the state border between Hungary and Austria.

limestone (Blaumoser, 2011; Bryda and Posch-Trözmüller, 2016). The observatory consists of a 144 m long and 3 m wide tunnel drilled in an EW direction (https://cobs.zamg.ac.at/gsa/index.php/en/observatory/virtual-3d-tour-sgo).

The facility has an outstanding infrastructure and provides a very stable environment for geodynamical investigations (e.g. seismological monitoring, observations of earth tides and loading effects). Table II shows the results of statistical and spectral analysis of more than 4 years of temperature data of the tunnel at the pier where the LTS SOP2 and the iWT tiltmeters are installed.

Between August 2014 and February 2020 the Geodetic and Geophysical Institute (GGI, Sopron, Hungary, predecessor of EPSS) operated a 5.5 m long Michelson–Gale-type interferometric water level tiltmeter (iWT), in order to monitor E–W ground tilts. It was designed and built by the Finnish Geodetic Institute (FGI; Ruotsalainen et al., 2016a,b; Ruotsalainen, 2018) and installed on a 6 m long pier in the middle of the tunnel.

In July 2015, a high-resolution Lippmann tilt sensor (LTS SOP2) was installed by GGI close to the iWT on the same pier (Papp et al., 2019). The LTS provides both NS and EW tilt time series. Local thermal insulation, made from 10 cm thick polystyrene plates, was applied for both tilt instruments. The

sampling rate of the SOP2 tiltmeter was 1 Hz until February 2022 and since then the LTS has been recording with 5 Hz. The collocated measurements of the two type of tiltmeters (iWT and LTS SOP2) allow for a comparison of the response of tiltmeters with long (several metres) and short (a few decimetres) base lengths.

The Central Institute for Meteorology and Geodynamics (ZAMG, Austria, predecessor of Geosphere Austria) had operated the superconducting gravimeter (SG) GWR–C025 at COBS over 11 years (2007–2018).

- Sopronbánfalva Geodynamical Observatory (SOPGO), EPSS, Hungary The Observatory, established in 1965 and located close to Sopron, is in the Sopron Mountains. The area belongs to the extensions of the Eastern Alps, which is formed by metamorphic rocks of Palaeozoic age, such as gneisses and various mica schist–granites (Haas, 2001). The observatory is a 60 m long artificial gallery (Mentes, 2010). On the 18$^{\text{th}}$ of January, 2023 the LTS SOP3 tiltmeter was installed in the deepest part of the tunnel system, in a chamber which was originally made to host so called horizontal pendulums. The selection of this final position of the tiltmeter was preceded by a series of test measurements at three other locations which proved to be inadequate because of the noise level and frequent disturbances (sudden steps) observed in the tilt time series. Nowadays the urban surrounding of SOPGO is not really ideal due to the city and the railway traffic. The railway line connecting Wien and Sopron runs approximately 900 m away from the station. It, however, provides very stable thermal conditions (Table II). The application of an insulation hut certainly contributes to this excellent thermal stability (Fig. 2).

An STS2 seismometer (seismological station code: SOP) and a 20 m long extensometer are operated in an 8–10 m distance to SOP2 sensor.

- Cellar of Pauline/Carmelites Cloister Sopronbánfalva (SOPPAL), Eszterháza Cultural-, Research- and Festival Center, Non-profit, Public Benefit Ltd, Hungary The LTS SOP4 sensor is installed in a small side chamber of the southern part of the cellar system on a concrete pillar. Although the cellar system is fully abandoned and permanently closed from the public, the usual local thermal insulation hut is applied. 0.1 °C/year temperature increase was detected. The results of spectral analysis of temperature data are shown in Table II.

- Brennbergbánya Szálasi bunker (BREBA), Fertő–Hanság National Park, Hungary The LTS SOP5 sensor is installed in the southern part of the vault system on a concrete pillar with thermal insulation (Fig. 2). The distance between the opening of the vault and the pillar is only 25 m. The amplitude of the annual thermal variation is 0.2 °C (Table II) due to the passive air ventilation system. This is an order of magnitude larger than that of other stations.

Table I. The stations, their instrumentation and some auxiliary data. Abbreviations: LTS – Lippmann type high resolution tiltmeter, SOP2, ..., SOP7 – sensor names, GWR SG – GWR superconducting gravity meter, LCR G949 – LaCoste and Romberg G type gravity meter, STS – Streckeisen seismometer, iWT – FGI type interferometric water tube (hydrostatic) tiltmeter. For further explanations see the sections from - *Conrad Obsevatory (COBS), Geosphere, Austria* to - *Seismological Station at Georgistollen, Pitten (PTNA), Geosphere, Austria.*

Stations	WGS84 (λ, φ, h)	Instruments and their owner	Operation period	Sampling rate
COBS	15.8613° 47.9282° 1045 m	LTS SOP2 (Hungary)	2015.07–	1 Hz, 5 Hz
		GWR SG-C025 (Austria)	2007–2018.11.17	1 Hz
		LCR G949 (Hungary)	2017.11.23–2021.01.25	1 Hz
		iWT (Hungary)	2014.08.14–2020.02.09	15 Hz
		STS2.5 (Austria)	2002	100 Hz
SOPGO	16.5526° 47.6771° 298 m	LTS SOP3 (Hungary)	2022.01.26–	5 Hz
		LCR G949 (Hungary)	2021.06.16–	1 Hz
		extensometer (Hungary)	1990–	1 min
		STS2 (Hungary)	–1994 2011–	analog 100 Hz
SOPPAL	16.5526° 47.6771° 263 m	LTS SOP4 (Hungary)	2022.04.28–	5 Hz
BREBA	16.4893° 47.6518° 415 m	LTS SOP5 (Hungary)	2023.06.15–	5 Hz
PTNA	16.1920° 47.7171° 370 m	LTS SOP7 (Hungary)	2023.01.13–	5 Hz
		STS2.5 (Austria)	2023.01.13–	100 Hz

- Seismological Station at Georgistollen, Pitten (PTNA), Geosphere, Austria PTNA station is located in a vault of an 18$^{\text{th}}$ century iron mine where GEOSphere operates a seismological station too. The LTS SOP7 sensor is installed in a distance of about 300 m from the entrance of the vault on a concrete pillar, in co-located position with the STS2.5 seismometer. The usual

local thermal insulation hut is applied (Fig. 2). The results of spectral analysis of temperature data are shown in Table II.

Table II. The results of main statistics and spectral analysis of temperature data registered by LTS sensors.
∗: cannot be estimated due to the short data length

Stations	Analyzed time interval	**Mean** temperature [°C]	Coefficient of **linear trend** [°C/year]	Amplitude of **annual** variation [°C]	Amplitude of **diurnal** variation [°C]	Amplitude of **semidiurnal** variation [°C]
COBS	2016.04.19–2020.04.03	8.468	-0.014	$4\ 10^{-3}$	$4.4\ 10^{-5}$	$1\ 10^{-4}$
SOPGO	2023.01.18–2024.11.06	12.368	0.022	$3\ 10^{-3}$	$1.6\ 10^{-4}$	$2\ 10^{-4}$
SOPPAL	2022.04.30–2024.09.17	10.842	0.110	$7\ 10^{-2}$	$2.5\ 10^{-4}$	$2\ 10^{-4}$
BREBA	2023.06.18–2024.08.04	10.738	∗	$2\ 10^{-1}$	$5.8\ 10^{-4}$	$1\ 10^{-4}$
PTNA	2023.03.07–2024.07.30	12.358	∗	$3\ 10^{-3}$	$1.6\ 10^{-4}$	$3\ 10^{-4}$

Fig. 2. A typical insulation hut of the tiltmeters applied at most sites.

Comparison of the Noise Characteristics of the Stations

Selecting a bit longer than 1 month continuous and overlapping time segments from the time series of N–S ground tilt data recorded at all the stations in 2023, their power spectra were determined and plotted for demonstration in Fig. 3. It clearly indicates that COBS station has the lowest noise level above 1 Hz (up to 2.5 Hz) which is basically dominated by anthropogenic noise. Here the peak amplitude varies between 0.01 mas (PTNA) and 0.03 mas (SOPGO) and generally it is higher by almost two orders of magnitude than what characterizes the observed noise level at COBS in the same frequency range.

There are only slight differences between the powers in the range of microseismic noise (0.06 Hz–0.2 Hz) generated by the interactions of atmospheric and hydrological processes in the North Atlantic region (e.g. Papp et al., 2012).

The large differences at lower frequencies, dominantly below 0.01 Hz, are mainly caused by the abrupt changes of the tilt which indicates the dynamics of local deformations of the sites. Whereas steps (sudden tilt changes) are small and rarely contaminate the data observed at COBS, SOPGO and SOPPAL, the time series recorded at the other two sites BREBA and PTNA are disturbed by steps and transient signals frequently. The reason of it could be either local (e.g. type and structure of the surrounding rocks) or regional, connected to the seismo–tectonic activity of the Mur–Mürz fault. PTNA is located just in the fault zone but both stations are operated on areas of abandoned mining activity. Thermal and hydrological impacts (Meurers et al., 2021) can also induce disturbing transient signals lasting for several days or even weeks in the time series.

The two sharp spectral peaks show the diurnal and semidiurnal wave group components of the tidal tilt spectrum.

Instrumentation

- LTS The Lippmann-tiltmeter is a very compact instrument (Fig. 4), equipped with two pendulums which provide tilt angles measured in two perpendicular directions (X/Ch#1 and Y/Ch#2) with nrad resolution (1 nrad = 10^{-9} m/m = 0.2 milliarcsec). Except COBS the orientations of the X and Y pendulums are N–S and E–W, respectively. The sign of tilt is positive in N and E directions. At COBS positive X and Y tilts mean tilt to E and tilt to S, respectively. An integrated meteorological station measuring the air temperature, -humidity, and -pressure is also build in inside the cover box of the instrument. At present the data provided by the tiltmeters are recorded with 5 Hz sampling rate at all stations.

- LCR G949 A LaCoste–Romberg G type gravity meter (LCR G949) purchased in 2000 has been used for more than two decades at the Geodetic and Geophysical Research Institute and its successors for different purposes. The instrument, originally manufactured for field surveys, was improved gradually to a

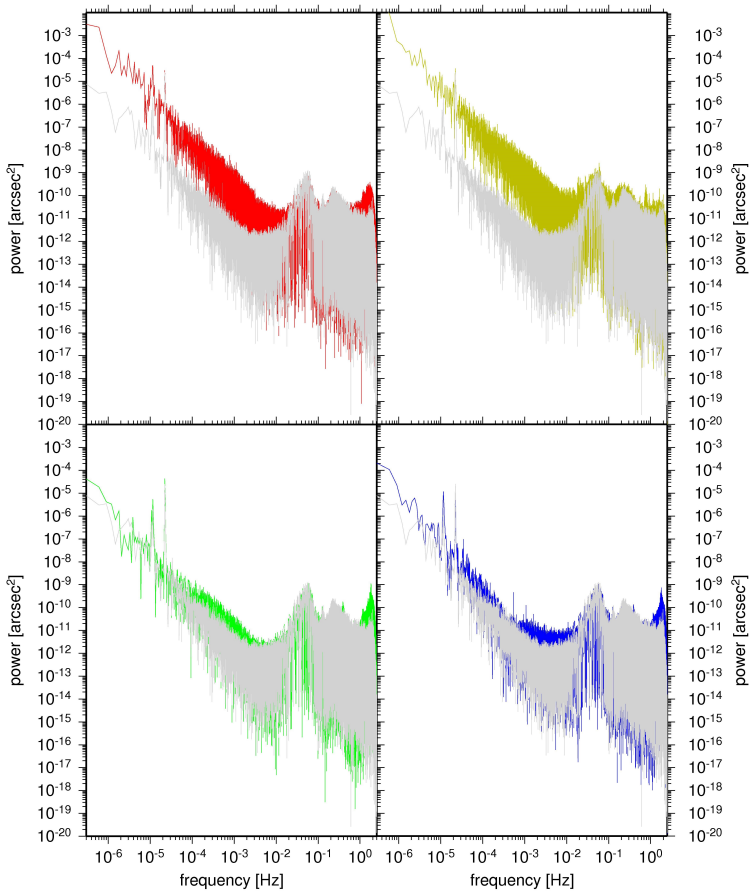

Fig. 3. Comparison of PSDs of N–S ground tilt time series observed at the monitoring stations of the Mur–Mürz fault line. The PSD of data recorded at COBS is the reference (grey), the other curves show PSDs of SOPGO (green), SOPPAL (blue), BREBA (red) and PTNA (yellow) stations.

complete and continuously operable gravity tide recording system in 2010–2014 by the scientific and technical staff of EPSS (Fig. 5a). Most of the hardware and software components necessary for that were designed, developed and made at the Institute. The complex reading system of the instrument controlled by a PC provides several types of data, which are recorded with 1 Hz sampling rate. For further details see the paper by Papp et al. (2018).

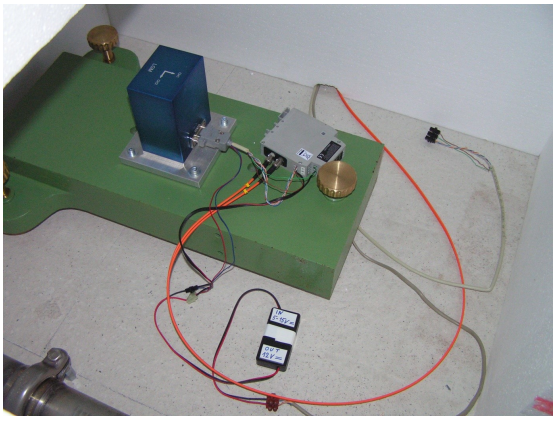

Fig. 4. The LTS SOP2 tiltmeter (blue cube) installed at COBS. Its heavy iron instrument platform (green) was made in the mechanical workshop of EPSS.

The tidal recording system has been operational at SOPGO since June, 2021. Before that it was used at several places in the Pannonian basin between 2012 and 2021 (Papp et al., 2018). Until now the longest time series provided by it was recorded at the Conrad Observatory (Barbély, 2023) between autumn of 2017 and June 2021 where it operated side by side with the GWR SG C025 superconducting gravity meter (Fig. 5b).

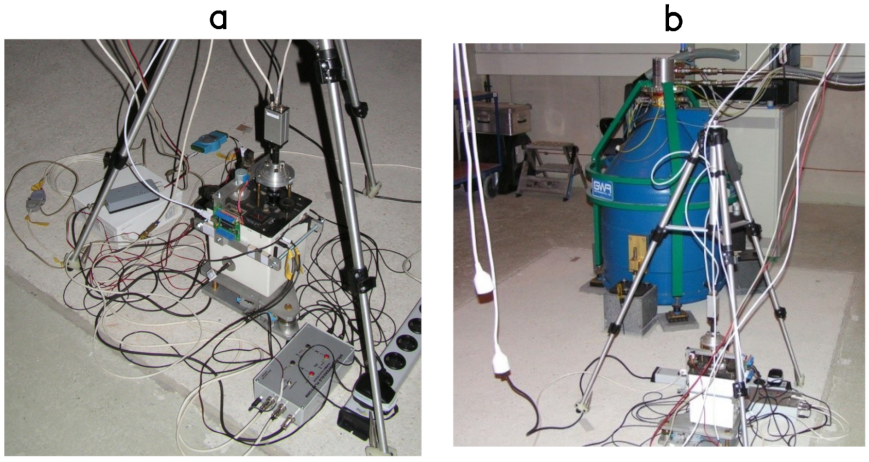

Fig. 5. (a) The complete gravity tide recording system. **(b)** The co-located setup of the GWR SG C025 superconducting- and the LCR G949 gravity meters at COBS.

Data Acquisition and Processing

Tiltmeter Data

At all the five stations (SOPGO, SOPPAL, BREBA, COBS and PTNA) the data is collected continuously on 5 channels with 5 Hz sampling rate. The channels consist of the tilt measurements along the x and y coordinate axes and the meteorological parameters (air temperature, -humidity and -pressure), measured inside the tiltmeter box, are recorded as well (Table III).

Table III. Example of some records of raw tiltmeter data recorded at station SOPPAL.

Timestamp	**X tilt [arcsec]**	**Y tilt [arcsec]**	**Temperature [°C]**	**Humidity [%]**	**Air pressure [mBar]**
20240919000000.00	-3.3406	7.4230	11.101	47.63	991.31
20240919000000.20	-3.3442	7.4232	11.101	47.60	991.31
20240919000000.40	-3.3422	7.4215	11.101	47.61	991.31
20240919000000.60	-3.3387	7.4231	11.101	47.62	991.31
20240919000000.80	-3.3361	7.4218	11.101	47.63	991.31
20240919000001.00	-3.3387	7.4220	11.101	47.64	991.31
20240919000001.20	-3.3403	7.4224	11.101	47.64	991.31
...	...	...	...	...	...

Data collection of tiltmeters is controlled by different Raspberry Pi platforms (RPiZero, RPi4). Remote access to the data collection systems is possible at each station. In case of internet access (COBS, SOPGO, SOPPAL, PTNA) a scheduled FTP process manages the data transfer of the daily data files. The measurements are updated hourly and are forwarded to the public web page (https://kepujsag.ggki.hu) maintained by EPSS Sopron. In case of lack of internet access (BREBA), the low bandwidth of the GMS internet service allows only one data file transfer per day. If an NTP server is unavailable (BREBA), then a GPS module card can be added to the system to provide time synchronization. In case of lack of mains electricity (BREBA), a fully autonomous data logger system characterized with very low current consumption (∼100 mA) has been developed. This system (sensor and data logger) can be powered by an 110 Ah battery providing 1.5 months of continuous operation. By the installation of a charging system connected to a solar panel the operation time could be arbitrarily increased without changing the battery.

For every day a sequential ASCII file is created the name of which is constructed from the station- and sensor names, a character string indicating the

orientation and the directions of positive tilts of the sensors X and Y axes and the datum string followed by the file extension named tlt (e.g. soppal_sop4_+XN_+YE_20240919.tlt). The data acquisition method, coded in FreeBasic language, is fitted to both the internal sampling process of the sensor and its requested served reading method (i.e. software triggering) provided by the firmware of the tiltmeters. So a time stamp of a digital reading managed through RS232 serial interface represents the nominal mean time of two internal sampling segments of 0.1 s length, preceding and following the specific time stamp. It practically means the averaging of 32 samples taken at 160 Hz internal sampling rate. The recorded and compressed daily files are transferred to the HP RX2800 unix server of the EPSS together with some status plots of the running observations made on the fly at regular time intervals and displayed on https://kepujsag.ggki.hu website managed by EPSS. Then the daily files can be downloaded for further processing.

The original size of a daily file containing 432000 samples at 5 Hz sampling is about 26.8 MByte. Its compressed version takes about 3.6 MByte disk space.

Table IV summarizes some statistics of the stability of data recording. The averages of the number of missing samples due to instantaneous failure of data transmission and recording (average length of automatically filled gaps per day, column 7, Table IV) varies between 11 and 238 samples, depending on the stations and their examined time periods. The histograms of the missing data records of each station are presented in Fig. 6, where the dashed vertical lines indicate the average values (column 7, Table IV) in sample unit. The higher number of missing samples (column 6, Table IV) causing gaps longer than what can be automatically filled, is usually resulted in by technical breakdowns (e.g. power failure) of the local recording systems.

LCR G949 Data

The data are arranged in daily files (e.g. 20181125.dat), which contain the temporal change of gravity (Δg), and the image shift, both measured in pixels due to the special electro–optical reading unit developed for the continuous and automated recording (Papp et al., 2018). In addition, the (so called cross level) X and (so called long level) Y tilt measurements, indicating the momentary levelled position of the instrument, are also recorded through an A/D converter in mV unit (Table V).

Meteorological data provided by a Procontrol meteorological sensor (THP-05-LD) is recorded every minute in a separate file (meteo.dat). It contains the temperature in degrees Celsius, the humidity in percentage, and the air pressure in mBar units (Table VI).

The Structure of Data Storage

The systematically named daily files (see e.g., Section *Tiltmeter Data*) are organized and stored in a hierarchical folder system (Fig. 7). It starts at the level

Table IV. Some statistics of the missing data per stations. The maximum number of the recorded samples is 432000 per day at 5 Hz sampling rate. The statistics in columns 5, 6 and 7 refer to the time period under consideration (column 2), excluding the missing full days (their number is listed in column 4).

Station	**examined time period**	**length of examined time period [days]**	**number of missing days**	**missing data [%]**	**average daily missing data records**	**average length of filled gaps [sec/day]**
SOPGO	2021-03-13 – 2024-11-05	1333	15	0.54	2320	2.18
SOPPAL	2022-04-30 – 2024-09-18	872	13	1.03	4453	5.08
BREBA	2023-06-16 – 2024-10-12	484	0	0.37	1607	33.33
COBS	2022-07-29 – 2024-07-01	703	20	0.81	3484	47.54
PTNA	2023-01-14 – 2024-07-29	562	46	1.05	4538	37.76

Table V. Some example data recorded by the LCR G949 gravimeter.

Timestamp	**Delta g** [pixel]	**Image shift** [pixel]	**X tilt** [mV]	**Y tilt** [mV]
20181115000000	-138.5	13.0	-000.61	-000.23
20181115000001	-139.0	13.0	-000.59	-000.23
20181115000002	-139.5	13.0	-000.61	-000.23
20181115000003	-139.0	13.0	-000.61	-000.25
20181115000004	-138.5	13.0	-000.63	-000.25
20181115000005	-139.0	13.0	-000.61	-000.25
20181115000006	-140.0	13.0	-000.59	-000.25
...	...	...	...	...

of data type (e.g., LTS_data). The next sub-level is identified by the sensor name (e.g., sensor_sop2). Below that level there are sub-folders indicating the format of the daily files (e.g., TSF). Then the sub-folders, identified by station

Table VI. Meteorological data.

Timestamp	**Temperature** [°C]	**Humidity** [%]	**Air pressure** [mBar]
2018.11.25. 0:00	018,5	46	0583,2
2018.11.25. 0:01	018,5	46	0583,2
2018.11.25. 0:02	018,5	46	0583,1
2018.11.25. 0:03	018,4	46	0583,2
2018.11.25. 0:04	018,4	46	0583,1
2018.11.25. 0:05	018,5	46	0583,1
2018.11.25. 0:06	018,4	46	0583,1
...	...	...	...

names, where the sensor has ever been installed and operated, follow. In the station name folder, the sub-folders are identified by different sampling rates (5Hz, 1sec, 1min, 1h). This indicates that the time series stored on this level contain not only the original recorded samples, but also filtered and decimated data. Finally, in the last sub-folder level the measurement years are defined.

In addition, a possibility of quick statistical characterization of the daily tsf files (complete, incomplete, missing) for a given year is also provided by running an interactive graphical file listing utility developed for this purpose under HP Unix (Fig. 8). The required statistics are saved in a log file too.

Software Used for Data Processing

For the on-site visualization, compression and transfer of the recorded data a scheduled process is used parallel to the data acquisition software at each sites. It hourly starts:

1. the drawing of the status plots creating the corresponding BMP files directly from codes written in FreeBasic,

2. to convert the BMP files to PNG format to reduce size of about 600 Kbytes to about 5 Kbytes,

3. the compression (gzip utility) of the daily files before the data transfer starts,

4. the FTP process of the compressed daily- and status plot files.

For further visualisation, data processing and manipulation Tsoft is used. It is an open-source software package developed for the analysis of time series (e.g.,

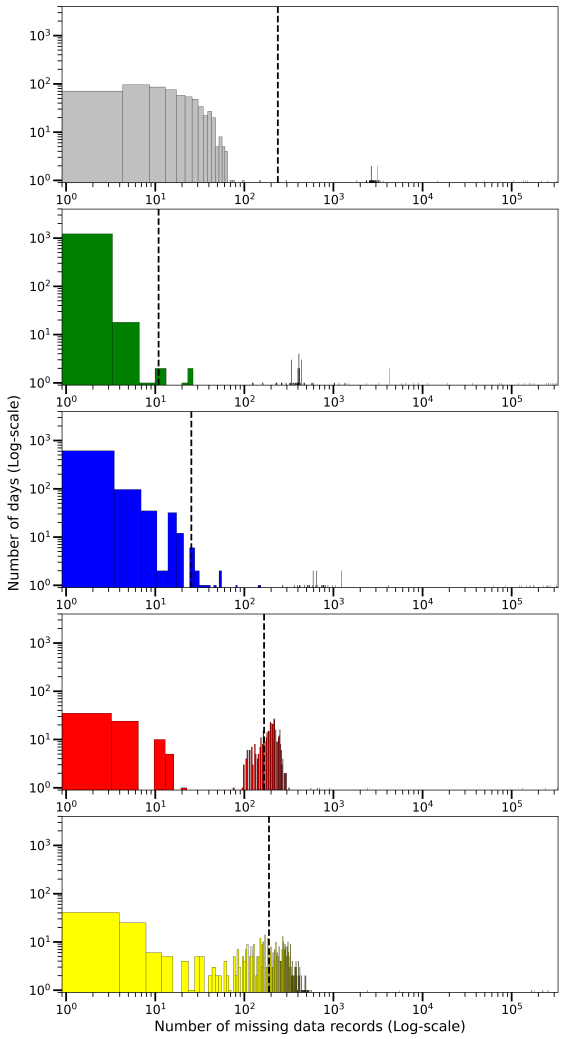

Fig. 6. Distributions of the number of missing data records per stations. The grey, green, blue, red and yellow colors from top to bottom indicate station COBS, SOPGO, SOPPAL, BREBA and PTNA, respectively. The dashed vertical lines represent the average value of missing records due to the failure of data transmission and recording (column 7, Table IV).

Earth tides) by the Royal Observatory of Belgium (Van Camp and Vauterin, 2005).

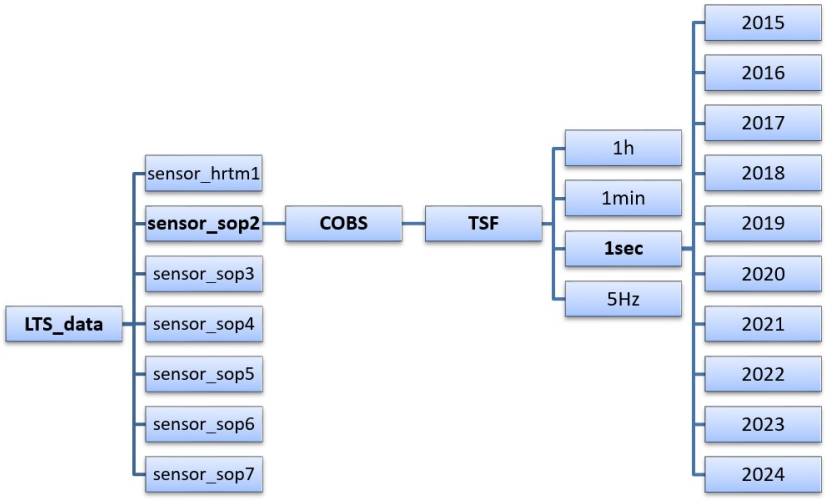

Fig. 7. Hierarchical folder structure to store daily TSF files measured by SOP2 sensor at the Conrad Observatory on QNAP disk unit mounted to rx2800 HP Unix server.

The input file format required by Tsoft is, however, different of that of the raw recorded data so a conversion utility applying a daily file based batch processing scheme is necessary. It was also developed at EPSS and its function is multiple. Beyond the format conversion it checks the consistency of data regarding formal record structure and the continuity of the time series. Short, few second long gaps can be filled on the fly by repeating the last valid recorded value of the respective channel. It calculates some statistics (data maximum and minimum, number of records, number of missing samples, etc...) and if the data structure is corrupted e.g., due to truncated records caused by accidental breakdown of the communication between the sensor and the data logger, it warns the user and records the situation in a log file. Using the log information the user can eliminate the irregular structure manually and can run the conversion program again in an iterative manner. The latest version of it can also be used to detect high noise sections in the time series being converted which makes the automatic determination of the first arrival of a transient tilt signal connected e.g., to seismological events (Benedek et al., 2024) possible.

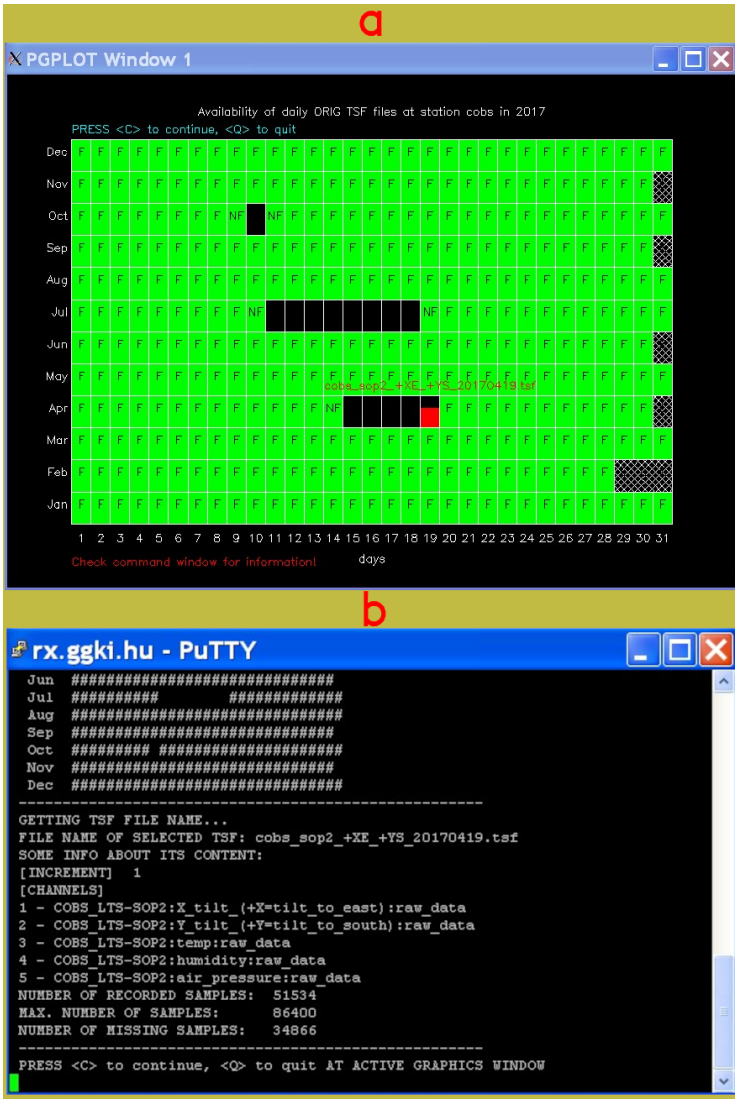

Fig. 8. **(a)** A calendar like presentation of the availability of the daily TSF files recorded by the SOP2 sensor at COBS in 2017. F: full, NF: not full. The height of the red column on the 19$^{\text{th}}$ of April is proportional to the number of available data. **(b)** Some details about the selected TSF file (cobs_sop2_+XE_+YS_20170419.tsf) and the data stored in it.

The time series defined in the file format of the software (TSF) are arranged into channels. In addition to efficient multi-channel visualization, both whole

channels and single data can be manipulated, corrected, or deleted as it is required. Although Tsoft is perfectly suitable for quick visual checking and calculations, it can process only segmented data in case of longer time series. However, as the amount of data increases, the use of the software becomes more and more difficult, slower, or after a certain amount of data, simply impossible. To overcome this problem an EPSS program was developed under HP Unix to visualize very long time series in X11 environment, where the RAM is user manageable up to its physical limit. This way two data vectors (time stamps and the data to be visualized) of 450 million samples in double precision can be handled easily. A one year long data set sampled at 5 Hz contains almost 157 millions of samples in a channel.

Table VII shows the structure of a TSF file containing data recorded by the LCR G949 gravity meter at Conrad Observatory. The header of the file basically defines the sampling rate, the format of the time stamp, the channels, their measurement units, and the number of the records. So, in the example given in Table VII there are seven channels with their names and measurement units. The data section of a TSF file contains the timestamps (year, month, day, hour, minute, second and alternatively millisecond columns) followed by the corresponding channel data. The meteorological data is only recorded at every full minute in this example. Where the data is missing and it cannot be filled automatically because of its length, the gap is indicated by the number 9999.9. This is the default value for NaNs (=not a number) in TSOFT but the user can arbitrarily define it in the TSF header section.

During the years of tidal analysis and data processing in EPSS, Sopron, many programs have been written to manage large data sets (data preprocessing, manipulation, filtering and spectral analysis), tending to automate some of the corrections and to make the data visualization interactive. These include, for example, the compilation and conversion of data files, and the batch processing tool of the continuous time domain convolution of daily TSF files applying various types of filters. According to processing needs the data is filtered and decimated and then stored in different time resolutions, for example in 5 Hz, 1 second, 1 minute and 1 hour time resolution (Fig. 7). These data are available in separate daily files so to obtain a continuous time series they must be interlaced for further analysis.

There are different types of corrections that need to be done during processing of data recorded by both the LCR G949 gravimeter and the Lippmann tiltmeters. These include the step and spike corrections and the diminishing of the unfavourable effects of earthquake signals and background microseism (Papp et al., 2012).

Step- and Spike Corrections

A step can be defined as a sudden shift (i.e. jump) between the values measured at two consecutive observation data and the data series continues with

Table VII. The structure of daily TSF files containing data recorded by both the LCR G949 gravimeter and a Procontrol meteorological station.

```
[TSF-file] v01.0


[UNDETVAL]  9999.9

[TIMEFORMAT] DATETIME

[INCREMENT]  1

[CHANNELS]
CO_g949: -delta_g
CO_g949: image_shift
CO_g949: X_tilt
CO_g949: Y_tilt
CO_g949: temp
CO_g949: humidity
CO_g949: air_pressure

[UNITS]
pixel
pixel
mV
mV
deg_C
percent
mbar

[COMMENT]

[COUNTINFO]  86400

[DATA]
2018 11 25 00 00 00  129.40   16.10   -0.76   -0.36   18.5   46.0  583.2
2018 11 25 00 00 01  127.90   16.10   -0.72   -0.38 9999.9 9999.9 9999.9
2018 11 25 00 00 02  128.90   16.10   -0.74   -0.36 9999.9 9999.9 9999.9
...
```

either bigger or smaller point values meanwhile the difference, represented by the jump, remains constant for a sufficiently long time interval. In other words: before and after a step/jump the mean values of the data segments are significantly different (see e.g., Students t-test). Such features frequently occur in ground tilt time series indicating that the tilt of the rocks underlying the instrument may be changed by sudden deformations caused by e.g., thermally or tectonically induced stress variations. One, however, can find artificial jumps also in gravity time series as well (Fig. 9), due to e.g., range compensating the effect of instrumental drift. It is possible to remove it manually and with a built in step correction tool in Tsoft. There is also an EPSS program that is used for step detection and its semi-automatic correction (Fig. 10).

Spikes (single outliers) are generally identified as sharp data peaks caused by abrupt positive or negative change decaying very quickly in the dataset. Unlike steps the data segment after the spike continues on the same average signal level as beforehand, only the spike (i.e. outlier data point) needs to be corrected. The removal of such a feature is also possible by Tsoft manually or with the autodetect spike function, which can be very efficient with an experimentally well-defined parameter set.

The importance of the step- and spike correction is obvious if spectral methods are applied in the processing of data. The whole spectrum of the processed

signal is influenced by these anomalies, consequently the estimation of the characteristics of specific spectral components can be highly biased if proper corrections of the anomalies are not applied.

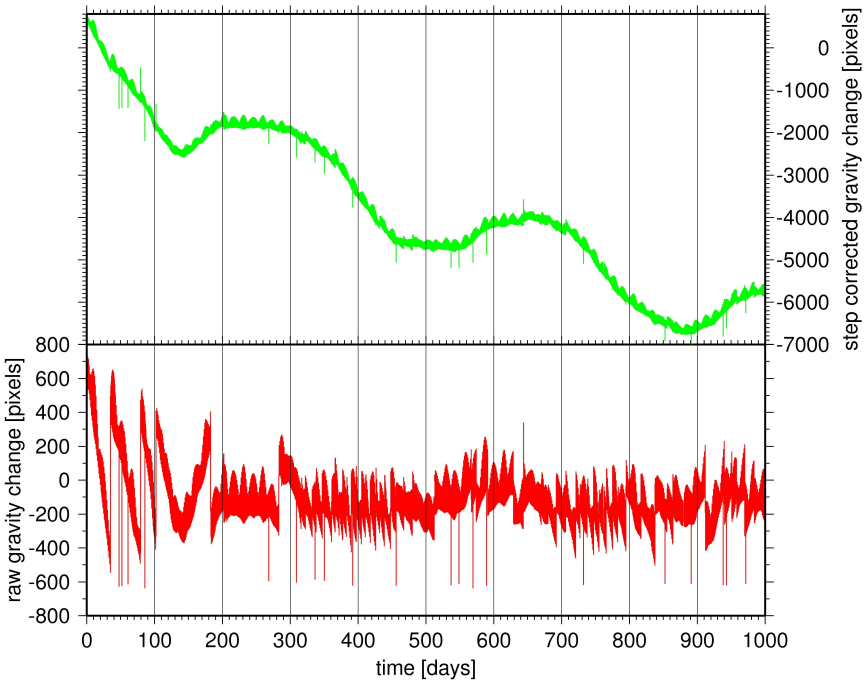

Fig. 9. A thousand days long time series of gravity variations recorded at COBS between 2017–2020 before (bottom panel) and after (top panel) step corrections. The waving shapes on the diagrams are the indications of the harmonic tidal signal.

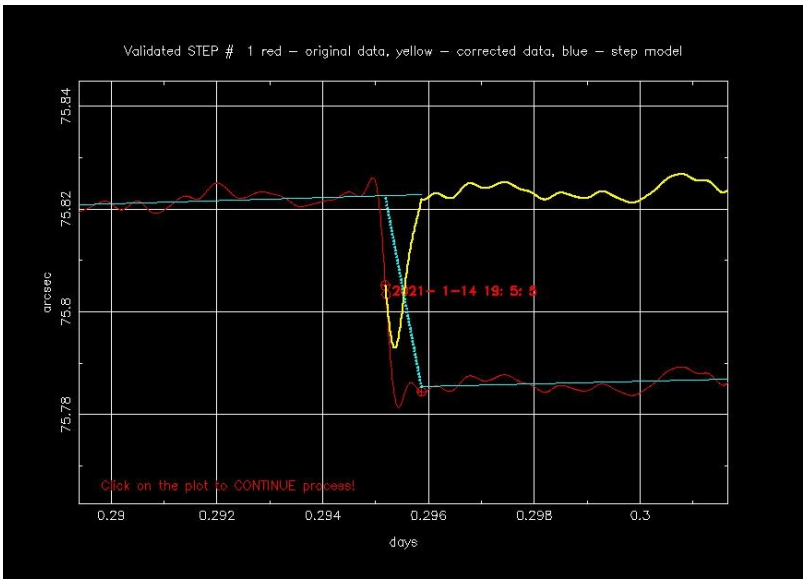

Fig. 10. An example of how the program developed at EPSS detects, models and corrects a step in a tilt time series interactively.

Gap Correction

Data gaps are continuous segments of missing data in the time series with varying length. The EPSS conversion program mentioned above (Section *Software Used for Data Processing*) can already handle the short, few second long gaps, however, in case of longer gaps another approach is necessary. The main goal of gap correction is to eliminate discontinuities in the data series by taking into consideration the trends of data segments located directly before and after the missing data. Gaps, however can also be created artificially if, for example, a data segment distorted by a transient signal of instrumental origin needs to be replaced for some reason. The method used to correct a gap or time segment of biased data lasting for a few hours at most, was developed by the Geodesy Research Group.

First the time series has to be low-pass filtered e.g., with the Chebyshev filter G1S1M (Fig. 11) (Hábel and Meurers, 2014), then the starting and ending point of the segment to be replaced or filled have to be identified (see interval A in Fig. 12). In the next step, the time derivative function of the filtered data is calculated numerically. Then, the derivatives have to be interpolated on interval A (Fig. 12) by e.g., linear or bicubic interpolation depending on its length. Finally, the derivative function has to be numerically integrated in

order to get back the approximate signal on interval A. In all other sections of the time series the original signal is preserved, naturally.

This method can efficiently be used to correct an unfavourable effect of earthquake signals recorded by the LCR G949 gravimeter (Fig. 12). In general, such a situation occurs when high-magnitude earthquakes are observed. This may cause a gap-like effect in the first, max. 30 minutes long segment of the earthquake signal (see interval B) because the arriving long periodic surface waves of large amplitudes may stick the index beam (which is a mechanical part of the sensor) to one of the two beam limiters (Instruction Manual, 1991). After the beam gets released a relaxation signal (see interval C) which may last for hours distorts the time series. This data segment can also be corrected by the method described above (Fig. 12). The correction is done manually with Tsoft.

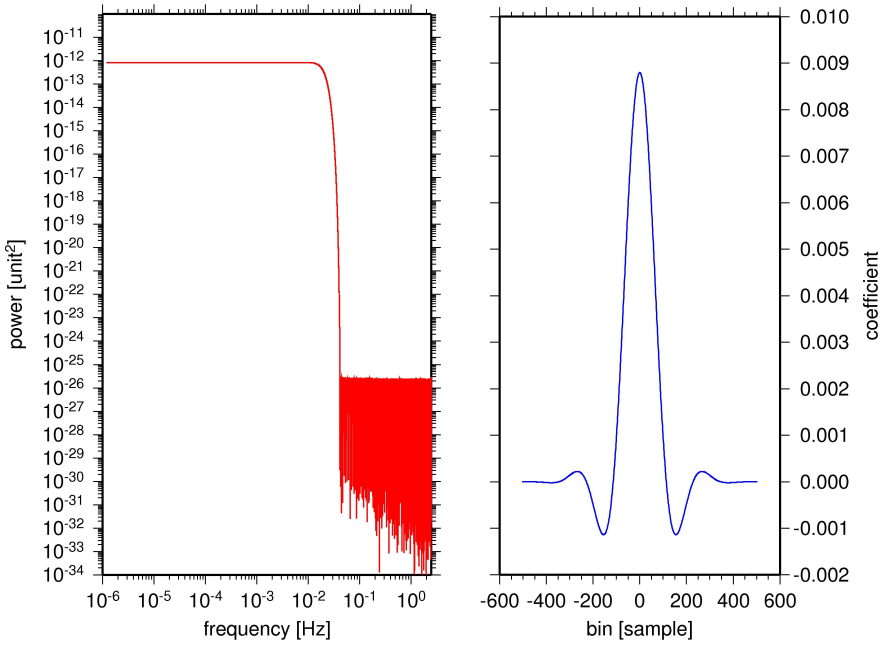

Fig. 11. The frequency (left panel) and time (right panel) representations of the low-pass GGP filter (g1s1md) used to eliminate high frequency noise from the tilt observations recorded at 5 Hz sampling rate.

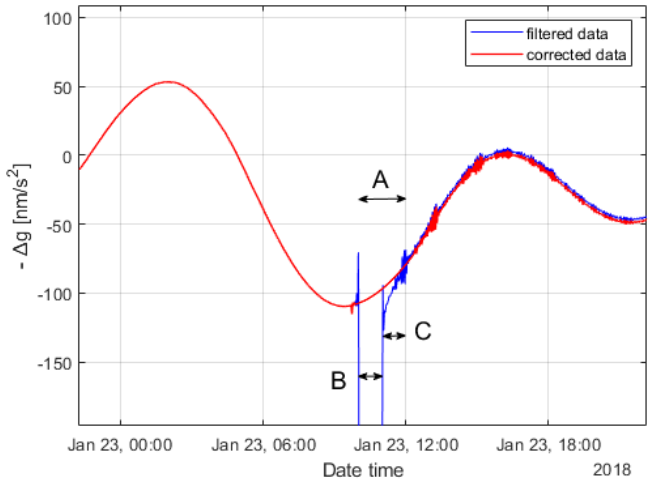

Fig. 12. Gap due to sticking of the index beam to one side of the measuring range caused by a large magnitude earthquake and its correction in the gravimeter measurements. Interval A: Filled/interpolated gap, Interval B: Data gap due to temporal index beam sticking. Interval C: Relaxation period after the index beam freely moves again.

Conclusions and Results

The network described in this paper provides simultaneous ground tilt and auxiliary meteorological data from its five stations since 15$^{\text{th}}$ of June, 2023. Based on the recorded data a successful attempt to locate epicentres for local earthquakes linked to the tectonic activity of the MurMürz fault line was made. The best inversion method developed for the processing of the tilt time series gives epicentre coordinates sufficiently close to the epicentres (4.5 km on average) determined from the observations of the nearby seismological stations. The first results are under publication (Benedek et al., 2024).

Acknowledgements

This study was supported partly by the National Research, Development and Innovation Office, Hungary, and partly by the Eötvös Loránd Research Network of Hungary (now called Hungarian Research Network) under the grants K141969 and IF-1/2021, respectively.

References

Barbély, E. (2023). *The comparison study and tidal analysis of collocated time series recorded by the GWR SG025 superconducting gravimeter (Conrad Observatory) and the LCR G949 tide gravimeter*. MSc thesis.

Benedek, J., Barbély, E., Horn, N., Meurers, B., Leonhardt, R., & Papp, G. (2025). Assessment of the network operation of high resolution Lippmann tiltmeters installed for the monitoring of the Mur-Mürz fault line (Austria). (Submitted to *Journal of Geodesy*).

Blaumoser, N. (2011). Hydrological and geological investigations at Trafelberg mountain. *Cobs Journal*, **2**, 12–12.

Bryda, G., & Posch-Trözmüller, G. (2016). Geological investigation of the drill core from borehole TB2A: First results. *Cobs Journal*, **4**, 9–9.

Haas, J. (2001). *Geology of Hungary*. ELTE Eötvös Kiadó, Budapest, Hungary.

Hábel, B., & Meurers, B. (2014). A new tidal analysis of superconducting gravity observations in Western and Central Europe. *Contrib. Geophys. Geod.*, **44**(1), 1–24. https://doi.org/10.2478/congeo-2014-0001

Instruction Manual (1991). *Model G and D Gravity Meters*. Austin, Texas, USA.

Jarvis, A., Reuter, H. I., Nelson, A., & Guevara, E. (2008). Hole-filled seamless SRTM data V4. International Centre for Tropical Agriculture (CIAT). Available from http://srtm.csi.cgiar.org.

Meurers, B., Papp, G., Ruotsalainen, H., Benedek, J., & Leonhardt, R. (2021). Hydrological signals in tilt and gravity residuals at Conrad Observatory (Austria). *Hydrol. Earth Syst. Sci.*, **25**(1), 217–236. https://doi.org/10.5194/hess-25-217-2021

Mentes, G. (2010). Quartz tube extensometer for observation of Earth tides and local tectonic deformations at the Sopronbánfalva Geodynamic Observatory, Hungary. *Rev. Sci. Instrum.*, **81**, 074501, 1–6. https://doi.org/10.1063/1.3470100

Papp, G., Szűcs, E., & Battha, L. (2012). Preliminary analysis of the connection between ocean dynamics and the noise of gravity tide observed at the Sopronbánfalva Geodynamical Observatory, Hungary. *J. Geodyn.*, **61**, 47–56. https://doi.org/10.1016/j.jog.2012.07.004

Papp, G., Benedek, J., Varga, P., Kis, M., Koppán, A., Meurers, B., Leonhardt, R., & Baracza, M.K. (2018). Feasibility study applied to mapping tidal effects in the Pannonian basin An effort to check location dependencies at μGal level. *Geod. Geodyn.*, **9**(3), 237–245. https://doi.org/10.1016/j.geog.2017.10.003

Papp, G., Benedek, J., Ruotsalainen, H., Meurers, B., & Leonhardt, R. (2019). A decade of international cooperation dedicated to geodynamical research. *Cobs Journal*, **6**, 23–23.

Ruotsalainen, H., Bán, D., Papp, G., Leonhardt, R., & Benedek, J. (2016a). Interferometric water level tilt meter at the Conrad Observatory. *Cobs Journal*, **4**, 11–11.

Ruotsalainen, H., Papp, G., Leonhardt, R., Bán, D., Szűcs, E., & Benedek, J. (2016b). Comparison of broadband time series recorded by FGI type interferometric water level- and Lippmann's pendulum type tilt meters recording parallel at Conrad Observatory, Austria. *Geophysical Research Abstracts*, 18, EGU2016-6932. In: EGU General Assembly 2016, 1722 April 2016, Vienna, Austria.

Ruotsalainen, H. (2018). Interferometric water level tilt meter development in Finland and comparison with combined Earth tide and ocean loading models. *Pure Appl. Geophys.*, **175**, 1659–1667. https://doi.org/10.1007/s00024-017-1562-6

Van Camp, M., & Vauterin, P. (2005). Tsoft: graphical and interactive software for the analysis of time series and Earth tides. *Comput. Geosci.*, **31**, 631–640. https://doi.org/10.1016/j.cageo.2004.11.015

Assessing Time Synchronization in Global ELF Station Networks Based on ELF Transients

Kolos Németh[1*] and Tamás Bozóki[1]

[1]HUN-REN Institute of Earth Physics and Space Science, Sopron, Hungary

Abstract

This study focuses on the time synchronization between 15 Extremely Low Frequency (ELF, 3 Hz–3 kHz) stations operated by 6 scientific institutions, which is critical for accurate detection and localization of ELF transients and their corresponding source lightning stroke. After identifying the transients by applying an amplitude threshold on the filtered time series, time synchronization was assessed by comparing the time differences between transients detected at paired stations. Most stations demonstrated proper synchronization, but significant timing discrepancies were found at the Eskdalemuir (ESK) station, requiring timestamp corrections to ensure reliable future use of the data.

Keywords: ELF station network, ELF transients, time synchronization.

Motivation

The motivation for this research stems from the critical importance of accurate time synchronization between ELF stations in detecting and localizing extremely powerful lightning discharges producing globally observable signals known as ELF transients or Q-bursts (Ogawa et al., 1966; Guha et al., 2017). Since ELF stations detect the electromagnetic signal emitted by lightning, they offer a powerful means to study global lightning activity (Sátori et al., 2009; Price et al., 2004). However, discrepancies in timing between stations can undermine the accuracy of such observations, hindering our ability to effectively localize and monitor lightning activity. This study aims to examine the time synchronization between ELF stations operated by different scientific institutions, drawing attention to potential problems.

Data and Methods

For the present study, measurements from 15 ELF stations operated by 6 scientific institutions were used. The most important information about these stations are listed in Table I, while their locations are shown in Figure 1.

*Corresponding author: Kolos Németh (nemeth.kolos@epss.hun-ren.hu)

Citation: K. Németh and T. Bozóki (2025): Assessing Time Synchronization in Global ELF Station Networks Based on ELF Transients. *Geophysical Observatory Reports, 2023–2024*, 106–111. https://doi.org/10.55855/gor2024.7

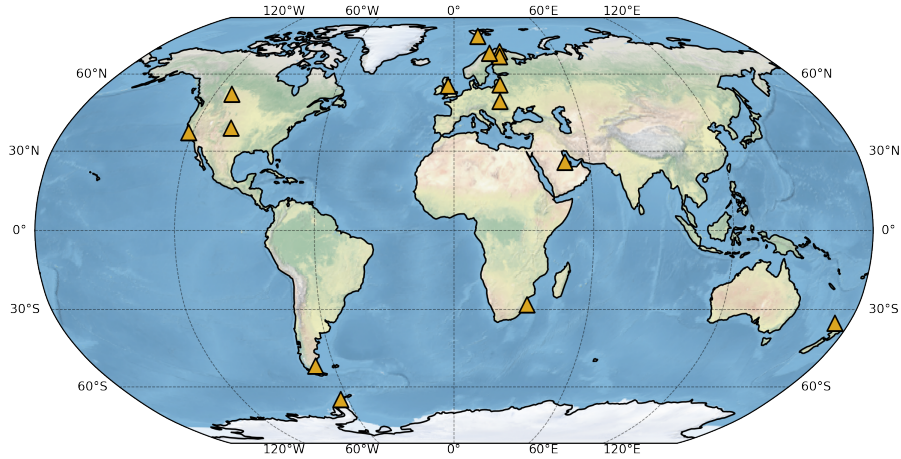

Fig. 1. Map showing the locations of the 15 ELF stations used in the study (marked by orange triangles).

Each station is equipped with a pair of induction coil magnetometers, one aligned with the geographic north and the other perpendicular to it. The Alberta (ALB), Baisogala (BAI), Boulder Creek (BOU), Hluhluwe (HLU), Hofuf (HOF), and Northland (NOR) stations are operated by the Heartmath Institute (https://www.heartmath.org/gci/). Vernadsky station (VRN) is located in Antarctica and is operated by the Institute of Radio Astronomy of the National Academy of Sciences of Ukraine. The Eskdalemuir (ESK) station is operated by the British Geological Survey, while the Hornsund (HRN) station in Svalbard is maintained by the Institute of Geophysics of the Polish Academy of Sciences. The Hugo (HUG), Hylaty (HYL), and Patagonia (PAT) stations are part of the World ELF Radiolocation Array (WERA), operated by the Krakow ELF group (http://www.oa.uj.edu.pl/elf/). The Kevo (KEV), Kilpisjärvi (KIL), and Sodankylä (SOD) stations are part of the Finnish pulsation magnetometer chain, operated by the Sodankylä Geophysical Observatory (https://sgo.fi/). More detailed information on the stations are available in Bozóki et al. (2023).

To effectively work with the data from different stations, standardized, one-hour time series were generated from the raw data files of various formats. In this step, the measured data were processed by applying a Finite Impulse Response (FIR) bandpass filter, which also corrected for the amplitude response of the recording systems. Based on the available information on the bandwidth and amplitude response of the measurement systems, the bandwidths of the FIR filters were chosen as follows: 2–45 Hz for the ALB, BAI, BOU, ESK, HLU, HOF, HRN, HUG, HYL, NOR, PAT, and VRN stations, and 2–31 Hz for the KEV, KIL, and SOD stations.

Table I. ELF Stations Used in the Study.

Station	Code	Country	Latitude (°)	Longitude (°)	Sampling (Hz)
Alberta	ALB	Canada	51,89	-111,47	130
Baisogala	BAI	Lithuania	55,63	23,70	130
Boulder Creek	BOU	USA	37,19	-122,12	130
Eskdalemuir	ESK	UK	55,29	-3,17	100
Hluhluwe	HLU	South Africa	-28,05	32,32	130
Hofuf	HOF	Saudi Arabia	25,94	48,95	130
Hornsund	HRN	Svalbard	77,0	15,6	100
Hugo	HUG	USA	38,89	-103,40	887
Hylaty	HYL	Poland	49,19	22,55	887
Kevo	KEV	Finnland	69,75	27,02	250
Kilpisjarvi	KIL	Finnland	69,05	20,79	250
Northland	NOR	New Zealand	-35,11	173,49	130
Patagonia	PAT	Argentina	-51,59	-69,32	887
Sodankyla	SOD	Finnland	67,43	26,39	250
Vernadsky	VRN	Antarctica	-65,25	-64,25	320

By using the standardized data files as input, the identification of transients was performed for each station. The input required for this process includes the total magnetic field, an amplitude threshold for detecting the transients and a merging threshold. The main steps of this process include determining a vector of time intervals during which the magnetic field exceeds the threshold, merging nearby time intervals, finding the maximum within the merged time intervals, and displaying the number of detected ELF transients. The output of this process is a list containing all the transients detected in the data file with the corresponding timestamps, as well as the transient's peak amplitude in pT, eccentricity and ELF azimuth in degrees. After generating the transient lists for each station, the time synchronization was assessed by pairing the transients detected at different stations. Two stations were always selected, one of which was designated as the reference station, against which the time synchronicity of transients appearing at the other station was examined. For each transient detected at the reference station, the closest event in time at the other station was identified, the time difference between these events was calculated, and these time differences were plotted.

Results

The proper synchronization of station timing is crucial, especially for applications like determining the location of source lightning strokes. The timing is typically well-synchronized among stations operated by the same group (as

they generally use the same measurement system), but discrepancies may arise between different station systems. Figure 2 illustrates the timing verification between the HRN station operated by the Geophysical Institute of the Polish Academy of Sciences and the BAI station operated by the Heartmath Institute. The figure shows the time differences between the transients detected closest in time at the two stations between 13 January 2019 and 31 January 2019. Ideally, this difference should be very close to 0 second, or more precisely, within a few tens of milliseconds, depending on the distance between the two stations. The few events outside this range were likely recorded only by one station, so there is no corresponding event at the other station. Based on Figure 2, the HRN and BAI stations are properly synchronized. Figure 3 shows the pairing of the HRN station and the ESK station operated by the British Geological Survey. It can be observed that in this case, the typical time differences are not within the window of a few tens of milliseconds but are around 50 seconds. Additionally, there is a stepwise increase in the typical time differences over the days. Based on this, it can be concluded that the timing of the ESK station shows a gradually increasing shift of around 50 seconds, at least during the examined period. In this form, the measurements from this station are not suitable for localization purposes, and the timestamps require precise correction. We now know that the ESK system was not intended for this type of study, and that it is probably very old compared to other stations.

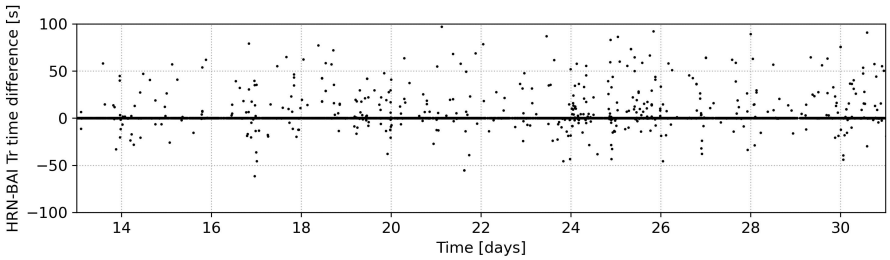

Fig. 2. The time differences between the transients detected closest in time at the HRN and BAI stations between 13 January 2019 and 31 January 2019. The horizontal axis shows the days, and the vertical axis shows the time difference in seconds.

We examined the time differences for all possible combinations of station pairs. Aside from the ESK station, issues only appeared in the plots of the pairs involving the South African HLU station. This is most likely due to the station's location, as there is significant lightning activity close to the station in the studied period. This is supported by the fact that this problem is only

observed when HLU is the reference station. The timing of the other 13 station was found to be adequate based on our investigation.

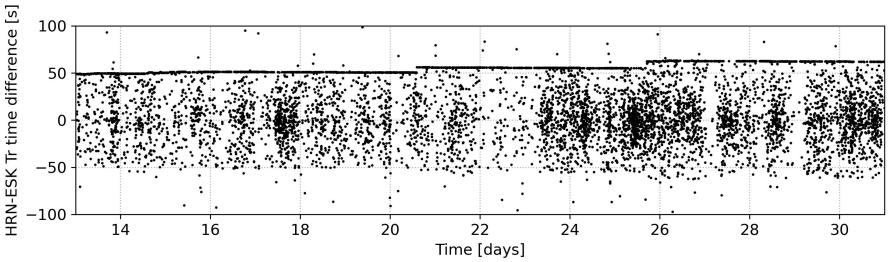

Fig. 3. The time differences between the transients detected closest in time at the HRN and ESK stations between 13 January 2019 and 31 January 2019. The horizontal axis shows the days, and the vertical axis shows the time difference in seconds.

Conclusions

This research confirmed that the majority of the examined ELF stations have proper time synchronization, which is critical for accurately localizing the source lightning stroke of ELF transients. However, significant timing discrepancies were found at the Eskdalemuir (ESK) station, requiring corrections to ensure reliable use of the data. Identifying such synchronization issues is essential for the effective observation and analysis of global lightning activity.

Acknowledgements

The authors wish to express their gratitude to the owners of the ELF stations for maintaining the measurements and for sharing the data used in this study. Tamás Bozóki acknowledges the contribution of József Bór in the development of the program used to identify and characterize ELF transients in two component magnetic measurements. This work was supported by the National Research, Development, and Innovation Office, HungaryNKFIH, project numbers K138824 and PD146019. The contribution of T.B. was also supported by the János Bolyai Research Scholarship of the Hungarian Academy of Sciences (BO/00352/24).

References

Ogawa, T., Tanaka, Y., Miura, T., & Yasuhara, M. (1966). Observations of natural ELF and VLF electromagnetic noises by using ball antennas. *J. Geomagn. Geoelec.*, **18**(4), 443–454. https://doi.org/10.5636/jgg.18.443

Guha, A., Williams, E., Boldi, R., Sátori, G., Nagy, T., Bór, J., et al. (2017). Aliasing of the Schumann resonance background signal by sprite-associated Q-bursts. *J. Atmos. Sol. Terr. Phys.*, **165–166**, 25–37. https://doi.org/10.1016/j.jastp.2017.11.003

Price, C., & Melnikov, A. (2004). Diurnal, seasonal, and inter-annual variations in the Schumann resonances. *J. Atmos. Sol. Terr. Phys.*, **66**(13–14), 1179–1187. https://doi.org/10.1016/j.jastp.2004.05.004

Sátori, G., Williams, E., & Lemperger, I. (2009). Variability of global lightning activity on the ENSO time scale. *Atmos. Res.*, **91**(2–4), 500–507. https://doi.org/10.1016/j.atmosres.2008.06.014

Bozóki, T., Sátori, G., Williams, E., Guha, A., Liu, Y., Steinbach, P., et al. (2023). Day-to-day quantification of changes in global lightning activity based on Schumann resonances. *J. Geophys. Res.: Atmos.*, **128**(11), e2023JD038557. https://doi.org/10.1029/2023JD038557